



HAL
open science

Reflectance of Jezero crater floor: 2. Mineralogical interpretation

Lucia Mandon, Cathy Quantin-Nataf, Clément Royer, Pierre Beck, Thierry Fouchet, Jeffrey Johnson, Erwin Dehouck, S. Le Mouélic, François Poulet, Franck Montmessin, et al.

► **To cite this version:**

Lucia Mandon, Cathy Quantin-Nataf, Clément Royer, Pierre Beck, Thierry Fouchet, et al.. Reflectance of Jezero crater floor: 2. Mineralogical interpretation. *Journal of Geophysical Research. Planets*, 2023, 128 (7), pp.e2022JE007450. 10.1029/2022JE007450 . insu-03885989

HAL Id: insu-03885989

<https://insu.hal.science/insu-03885989>

Submitted on 26 Jan 2024

HAL is a multi-disciplinary open access archive for the deposit and dissemination of scientific research documents, whether they are published or not. The documents may come from teaching and research institutions in France or abroad, or from public or private research centers.

L'archive ouverte pluridisciplinaire **HAL**, est destinée au dépôt et à la diffusion de documents scientifiques de niveau recherche, publiés ou non, émanant des établissements d'enseignement et de recherche français ou étrangers, des laboratoires publics ou privés.

Reflectance of Jezero crater floor: 2. Mineralogical interpretation

L. Mandon¹, C. Quantin-Nataf², C. Royer¹, P. Beck³, T. Fouchet¹, J. R. Johnson⁴, E. Dehouck², S. Le Mouélic⁵, F. Poulet⁶, F. Montmessin⁷, C. Pilorget⁶, O. Gasnault⁸, O. Forni⁸, L. E. Mayhew⁹, O. Beyssac¹⁰, T. Bertrand¹, E. Clavé¹¹, P. Pinet⁸, A. J. Brown¹², C. Legett¹³, J. Tarnas¹⁴, E. A. Cloutis¹⁵, G. Poggiali^{1,16}, T. Fornaro¹⁶, S. Maurice⁸, R. C. Wiens^{13,17}, The SuperCam team¹⁸

¹LESIA, Observatoire de Paris, Université PSL, CNRS, Sorbonne Université, Université de Paris, Meudon, France

²Université de Lyon, UCBL, ENSL, CNRS, LGL-TPE, Lyon, France

³Université Grenoble-Alpes, CNRS, IPAG, UMR 5274, Grenoble, France

⁴Johns Hopkins University Applied Physics Laboratory, Laurel, Maryland, USA

⁵Laboratoire Planétologie et Géosciences, CNRS UMR 6112, Nantes Université, Université Angers, 44322 Nantes, France

⁶Institut d'Astrophysique Spatiale, CNRS/Paris-Saclay University, France

⁷LATMOS, CNRS, Univ. Saint-Quentin-en-Yvelines, Sorbonne Univ., Guyancourt, France

⁸IRAP, CNRS, Université de Toulouse, UPS-OMP, Toulouse, France

⁹Department of Geological Sciences, UCB 399, University of Colorado-Boulder, Boulder, Colorado 80309, USA

¹⁰Institut de Minéralogie, de Physique des Matériaux et de Cosmochimie (IMPMC), Université

Pierre-et-Marie-Curie (UPMC), Paris, France

¹¹Centre Lasers Intenses et Applications, CNRS, CEA, Université de Bordeaux, 33000 Bordeaux, France

¹²Plancius Research, MD, USA

¹³Los Alamos National Laboratory, Los Alamos, NM, USA

¹⁴NASA, JPL, Caltech, USA

¹⁵University of Winnipeg, Canada

¹⁶INAF-Astrophysical Observatory of Arcetri, largo E. Fermi n.5, 50125 Firenze, Italy

¹⁷Earth, Atmospheric, and Planetary Sciences, Purdue University, West Lafayette, Indiana, USA

¹⁸A list of authors and their affiliations appears at the end of the paper

Key Points:

- Mineralogy of rocks, regolith and dust of the crater floor of Jezero, Mars was inferred from SuperCam reflectance data
- Assemblages suggest limited aqueous alteration of igneous rocks, followed by evaporation-induced deposition of sulfates
- Samples collected on the crater floor for return to Earth are representative of the geological diversity and witness past-aqueous processes

Abstract The Perseverance rover landed in the ancient lakebed of Jezero crater, Mars on February 2021. Here we assess the mineralogy of the rocks, regolith, and dust measured during the first year of the mission on the crater floor, using the visible and near-infrared spectrometer of SuperCam onboard the Perseverance rover. Most of the minerals detected from orbit are present in the bedrock, with olivine-bearing rocks at the bottom of the stratigraphy and high-Ca pyroxene-bearing rocks at the top. This is distinct from the overall low-Ca pyroxene-bearing composition of the watershed of Jezero, and points towards an igneous origin. Alteration mineral phases were detected in most of the rocks analyzed in low proportions, suggesting that aqueous alteration of the crater floor has been spatially

Corresponding author: Lucia Mandon, lucia.mandon@obspm.fr

This article has been accepted for publication and undergone full peer review but has not been through the copyediting, typesetting, pagination and proofreading process, which may lead to differences between this version and the [Version of Record](#). Please cite this article as [doi: 10.1029/2022JE007450](https://doi.org/10.1029/2022JE007450).

This article is protected by copyright. All rights reserved.

widespread, but limited in intensity and/or time. The diverse aqueous mineralogy suggests that the aqueous alteration history of the crater floor consists of at least two stages, to form phyllosilicates and oxyhydroxides, and later sulfates. We interpret their formation in a lake or under deeper serpentinization conditions, and in an evaporative environment, respectively. Spectral similarities of dust with some rock coatings suggest widespread past processes of dust induration under liquid water activity late in the history of Jezero. Analysis of the regolith revealed some local inputs from the surrounding rocks. Relevant to the Mars Sample Return mission, the spectral features exhibited by the rocks sampled on the crater floor are representative of the diversity of spectra measured on the geological units investigated by the rover.

Plain Language Summary

We present the results of the analysis of rocks and regolith measured during the first year after landing of the Perseverance rover on Mars. The analytical technique used is reflectance spectroscopy (the measurement of the light reflected by surfaces), which primarily provides information on mineralogy. The mineralogical composition of the magmatic rocks located near the landing site indicates that they have experienced several distinct episodes of interaction with water in the past, of relatively low intensity. Soil analysis reveals a composition similar to what has been observed at other sites on Mars, with a contribution from the disintegration of local rocks. The samples collected by Perseverance at the crater floor and that will be brought back to Earth are representative of the diversity of the different geological units explored by the rover.

1 Introduction

The Noachian (>3.7 Ga in the Hartmann & Neukum, 2001 chronology) and early Hesperian (3–3.7 Ga) terrains of Mars are marked by the activity of water, as evidenced by the presence of deltaic deposits, valley networks and hydrated minerals (Masursky, 1973; Fassett & Head, 2005; Poulet et al., 2005; Carter et al., 2013; Mangold et al., 2021). However, little is known about the duration and spatial extent of the liquid water activity on Mars. The science goals of the Mars 2020 mission (NASA) include characterizing past environments on Mars capable of supporting microbial life, searching for biosignatures, and collecting core rock and soil samples for return to Earth by the forthcoming Mars Sample Return (MSR, NASA/ESA) mission (Muirhead et al., 2020; Farley et al., 2020).

On the 18th of February 2021, the Mars 2020 rover Perseverance landed at the "Octavia E. Butler" site, on the floor of the 45-km diameter Jezero crater, which hosted a lake during Hesperian and/or Noachian eras (Fassett & Head, 2005; Mangold et al., 2021). During the first year of the mission, Perseverance investigated rocks and regolith of the crater floor with the aim of understanding the origin and history of its geological units. Before landing, it was uncertain whether the units of the crater floor were emplaced through magmatic/volcanic processes (such as lava flows or pyroclastic deposits) or as sediments related to the lake activity, and how they compared with the terrains of similar inferred mineralogy outside of Jezero.

The payload of Perseverance includes the SuperCam instrument, which combines several remote-sensing techniques to investigate the elemental and mineralogical composition of rocks and soils: high-resolution color imaging (RMI), laser-induced breakdown spectroscopy (LIBS), Raman spectroscopy, visible and near-infrared (VISIR) reflectance spectroscopy, and acoustic sensing (Wiens et al., 2021; Maurice et al., 2021). In particular, while near-infrared spectroscopy has been widely used to detect and map miner-

als from orbit (e.g., Ehlmann et al., 2009; Carter et al., 2013), its application as an in situ technique is a novelty. SuperCam passive reflectance spectra cover the 0.39–0.85 μ m (VIS) and 1.3–2.6 μ m (NIR) ranges, which allow the identification of a wide variety of minerals, especially hydrated ones, and hence can help to constrain past environmental conditions at Jezero crater (Fouchet et al., 2022).

In this contribution, we assess the mineralogy of the crater floor of Jezero using in situ SuperCam VISIR spectra acquired during the Crater Floor Campaign (until sol 379). Our analysis includes data collected on rocks (including cached samples) and soils at Jezero, and spanning a \sim 1 km region around the landing site. We present observations of the Martian dust as well, measured for the first time in the near-infrared in situ. Our results have implications for the origin and alteration history of the rocks of the crater floor, and open new possibilities for contextualizing orbital studies.

A companion paper describes the state of the calibration of the NIR data, as well as its impact on the detection of the minerals presented in this study (Royer et al., this issue/Royer et al., 2022).

2 Jezero crater: geologic background

2.1 The crater floor and its watershed as seen from orbit

While several terrains explored by previous rover missions are of Hesperian age (e.g., Irwin et al., 2005), the particularity of Jezero crater is its Noachian age (Mandon et al., 2020) and hence the possibility to expose in-place Noachian rocks, providing insights into the earliest Martian environments. Its fluvial activity (continuous or intermittent) is likely to have started during the Noachian and persisted at least until the Early Hesperian (Mangold et al., 2020). The crater is connected to a large valley network, whose 15,000–30,000 km² catchment drained the Nili Fossae region, on the margin of the Isidis impact basin (Fassett & Head, 2005; Goudge et al., 2015). The main valley connected to Jezero crater, Neretva Vallis, dissects the Western rim and is associated with preserved deltaic deposits (Fassett & Head, 2005; Fig. 1), which are likely to expose blocks of the Noachian crust for future exploration and sampling by the Perseverance rover (Mangold et al., 2021).

As seen from orbit, the area drained by this valley network shows abundant morphological and mineralogical diversity, and all of the various lithologies present in this region could have potentially been transported and deposited into Jezero in the delta region or as finer distal sediments in the lake. The most ancient rocks of the region, pre-Isidis impact (3.96 ± 0.1 Ga; Werner, 2008), can be observed as large massive or stratified basement outcrops or megabreccia blocks, with a spectral signature of low-Ca pyroxene or Fe/Mg-rich clays (Mustard et al., 2009; Scheller & Ehlmann, 2020). These lithologies are embedded in a low-albedo, smooth and ridged phyllosilicate-bearing basement that is regionally capped by a \sim 10 m thick Noachian-age unit found with olivine, carbonate and phyllosilicate mineral detections from orbit, hereafter referred to as the regional olivine-bearing unit (Hoefen et al., 2003; Mangold et al., 2007; Mustard et al., 2007; Ehlmann et al., 2008, 2009; Brown et al., 2010; Kremer et al., 2019; Mandon et al., 2020; Brown et al., 2020).

The interior of Jezero also shows morphological and mineralogical diversity, with spectral signatures similar to regional observations outside the crater (Goudge et al., 2015). In particular, the unit mapped by Stack et al. (2020) as the Crater floor fractured unit (Cf-f) and the Marginal fractured unit (Horgan et al., 2020) are fractured, light-toned, and have strong signatures of olivine and carbonate respectively, all of these features being commonly observed in the regional olivine-bearing unit (Hoefen et al., 2003; Ehlmann et al., 2008; Mustard et al., 2009; Ody et al., 2013; Goudge et al., 2015; Fig. 1). Stack et al. (2020) mapped the Cf-f unit as two distinct bedrock units: the Cf-f-2 occurs at higher

145 elevation than the adjacent Cf-f-1 unit and exhibits a rougher texture with meter-scale
146 bumps and ridges.

147 The Cf-f occupies the lowest position in the stratigraphy exposed at the crater floor.
148 Kremer et al. (2019) and Mandon et al. (2020) showed that the regional olivine-bearing
149 unit overlies the rim of Jezero crater, hence positioning both the regional olivine-bearing
150 unit and the olivine-bearing Cf-f on the same stratigraphic level. However, from orbital
151 studies, the relationship between the regional and Cf-f olivine-bearing units is ambigu-
152 ous, and it is unclear if the olivine deposits inside and outside the crater share a com-
153 mon origin. From orbital studies, the following scenarios have been proposed to explain
154 the nature of the regional olivine-bearing unit: lava flows (Tornabene et al., 2008), im-
155 pact product of Isidis (Mustard et al., 2007; Palumbo & Head, 2018), pyroclastic deposits
156 (Bramble et al., 2017; Kremer et al., 2019; Rogers et al., 2018; Mandon et al., 2020), and
157 sedimentary deposits (Rogers et al., 2018). As noted by Stack et al. (2020), a volcanic,
158 aeolian, or fluvio-lacustrine sediment origin appears plausible for the Cf-f unit, based on
159 orbital data.

Surficial units

- Ab-s Aeolian bedforms, large
- Ab-sm Aeolian bedforms, small
- Minor Cover
- Moderate Cover
- T Talus
- Us Undifferentiated smooth

Geologic units

- Cf-f-1 Crater floor fractured 1
- Cf-f-2 Crater floor fractured 2
- Cf-fr Crater floor fractured rough
- Cr-bl Crater rim blocky
- Cr-br Crater rim breccia
- Cr-l Crater rim layered
- Cr-r Crater rim rough
- D-bl Delta blocky
- D-lr Delta layered rough
- D-tkl Delta thickly layered
- D-tnl Delta thinly layered
- D-tcl Delta trunc. curvilinear layered
- M-f Margin fractured
- NV-l Neretva Vallis layered
- NP-f Nili Planum fractured

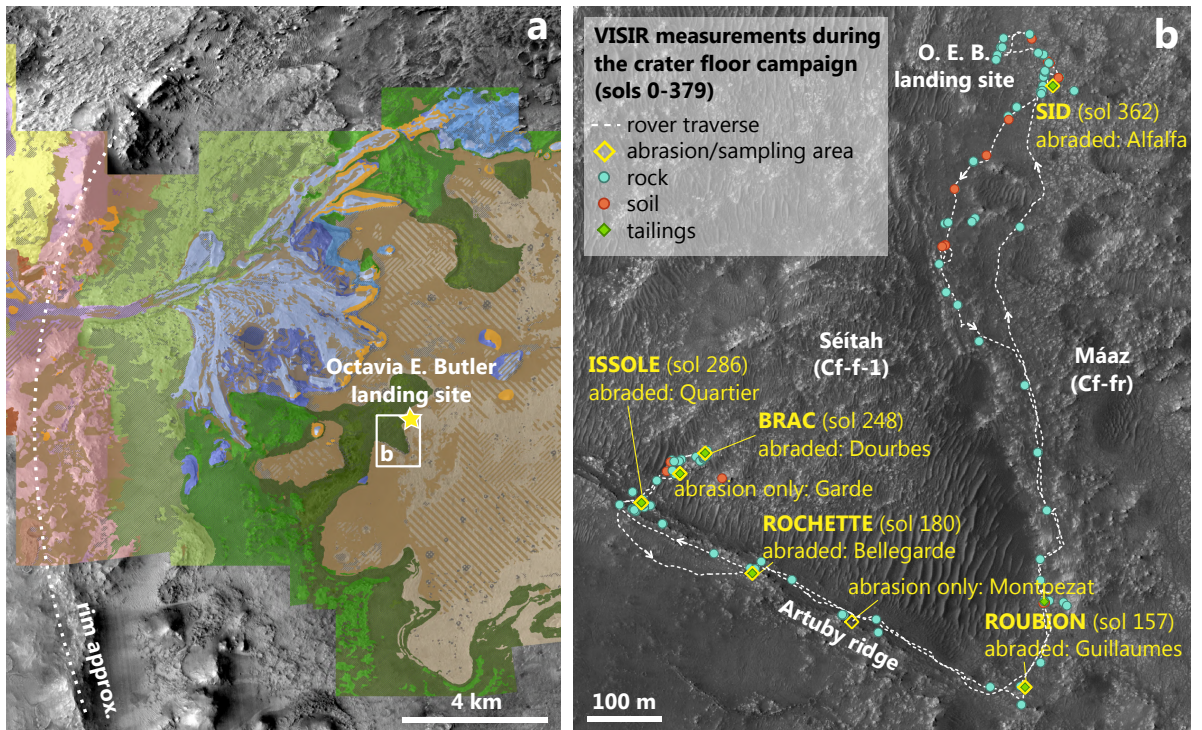


Figure 1: (a) Photogeological map of Western Jezero (modified from Stack et al., 2020). (b) Rover traverse and reflectance measurement locations overlain on a HiRISE mosaic (McEwen et al., 2007; Ferguson et al., 2020), SuperCam long-distance (>~60 m) observations excluded. Each color dot corresponds to a VISIR raster acquisition (usually consisting of one to ten individual spectra spaced on a target), while diamonds correspond to VISIR raster on abrasion or sampling targets. Sol annotations next to an abrasion/sampling site refer to sol number arrival of the rover at the corresponding workspace.

160 The Marginal fractured unit that outcrops on the Western part of the crater also
161 shares morphological and spectral similarities with the regional olivine and carbonate-
162 bearing unit. Horgan et al. (2020) proposed a distinct authigenic and lacustrine precipi-
163 tation origin based on the strong carbonate signature and elevation distribution of the

164 unit along the crater margin. The Perseverance rover has not yet investigated these ex-
 165 posures.

166 Stratigraphically above the Cf-f lies a unit referred to as the Crater floor fractured
 167 rough (Cf-fr) unit by Stack et al. (2020; Fig. 1). This unit has a lower albedo than the
 168 Cf-f rocks, a rougher, boulder-producing, crater-retaining morphology and is associated
 169 with a spectral signature of pyroxenes and olivine, which led Schon et al. (2012) and Goudge
 170 et al. (2015) to propose a lava flow origin for this unit. Because rocks with a similar mor-
 171 phology were observed from orbit and then interpreted as sediments with data from the
 172 Mars Science Laboratory (MSL) mission (Edgett, 2018), Stack et al. (2020) noted that
 173 a fluvio-lacustrine origin is also conceivable for the Cf-fr unit. The Cf-fr has been dated
 174 at 2.6 ± 0.6 Ga (Shahrzad et al., 2019), hence late in the crater history and after delta
 175 deposition. However, Quantin-Nataf et al., this issue/Quantin-Nataf et al. (2021) sug-
 176 gested that burying and resurfacing processes are responsible for this apparent young
 177 age. In their scenario, the Cf-fr would have been emplaced earlier (>3 Ga), before the
 178 deltaic exposures observed in the western part of the crater. This hypothesis, also sup-
 179 ported by Holm-Alwmark et al. (2021), has significant implications for sample return and
 180 calibration of the Martian chronology.

181 Overall, both the Cf-fr and the Cf-f-1 (explored by Perseverance during the first
 182 year of the mission) exhibit orbital spectral signatures of igneous minerals, with limited
 183 hydration, as opposed to the delta and the marginal fractured unit, or the geological units
 184 outside of Jezero crater, which exhibit stronger hydration features (Goudge et al., 2015).

185 2.2 Perseverance’s activities in the crater floor

186 The Perseverance rover landed at the Octavia E. Butler site, on top of the Cf-fr
 187 and close to the Cf-fr/Cf-f contact (Fig. 1). During the first sols of the mission, the rover
 188 investigated rocks and soils of the Cf-fr, that was informally renamed the Mááz forma-
 189 tion (“Mars” in the Navajo language, in keeping with the naming scheme for the *Canyon*
 190 *de Chelly* quadrangle in which the rover landed). On sol 170, the rover reached an area
 191 with layered rocks named the Artuby ridge, and corresponding to the transition from
 192 the Cf-fr to the olivine-bearing Cf-f-1. On sol 202, the rover made its first entry into the
 193 Cf-f-1, in a highly dune-covered area called Séítah (“amidst the sands” in Navajo, Fig.
 194 1), and made its way back to the Octavia E. Butler area on sol 360 with the intent on
 195 driving to the delta front. Along the traverse, eight samples were successfully acquired,
 196 two pairs in the Mááz formation, and two pairs in the Séítah formation (Simon et al.,
 197 this issue/Simon et al., 2022).

198 The first ~ 300 sols of investigation showed that the crater floor consists of igneous
 199 terrains and not lake sediments (Farley et al., 2022; Wiens et al., 2022; Liu et al., 2022).
 200 They exhibit a density stratification, with decrease of the SiO_2 content and increase of
 201 FeO and MgO from the Mááz to the Séítah rocks (Wiens et al., 2022). In particular, mm-
 202 sized olivine crystals out of equilibrium with the melt composition and showing a poikilitic
 203 texture in Séítah suggest a cumulate origin (Wiens et al., 2022; Liu et al., 2022; Beyssac
 204 et al. this issue/Beyssac et al., 2021).

205 2.2.1 The Mááz formation (Cf-fr)

206 The Mááz formation is composed of dark-toned and massive rocks showing layer-
 207 ing and internal stratification on its stratigraphically lowest portions (Horgan et al., this
 208 issue) and scarce vesicular texture, as well as flat, low-standing and highly dust-covered
 209 rocks referred to as “pavers” (Fig. 2a). These two types of rocks appear to be a differ-
 210 ent morphological expression of the same lithology, with the dark-toned rocks being likely
 211 more resistant to erosion than the pavers, as they share overall similar bulk-rock com-
 212 positions (Wiens et al., 2022; Udry et al., this issue/Udry et al., 2022). Abraded rocks

213 of the Mááz formation exhibits a texture showing angular coarse grains ($>300 \mu\text{m}$; Wiens
 214 et al., 2022) with no apparent matrix, and of variable tint (Fig. 2b).

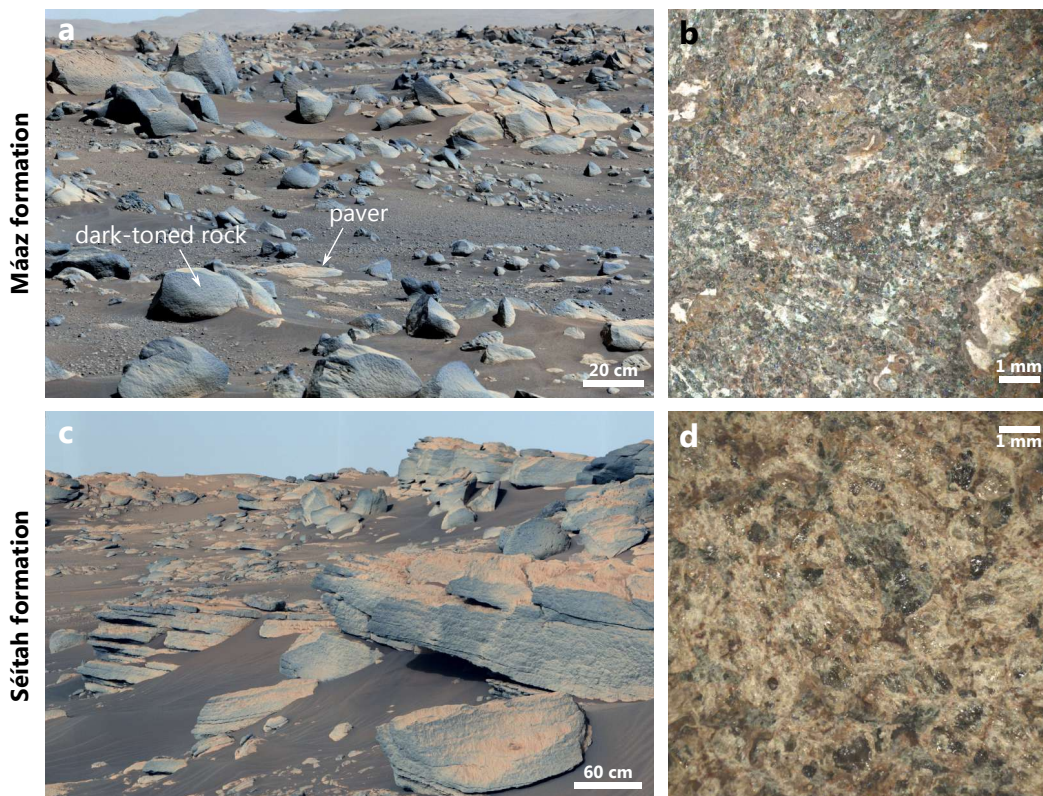


Figure 2: (a) Mastcam-Z mosaic panorama with the maximum zoom at 110 mm focal length taken on sol 78 in the Mááz formation. (b) ACI and WATSON merged images of the *Bellegarde* abraded patch (Mááz formation) taken on sol 186. (c) Mastcam-Z mosaic panorama with the maximum zoom at 110 mm focal length taken on sol 211 in the Séítah formation. (d) ACI and WATSON merged images of the *Garde* abraded patch (Séítah formation) taken on sol 207. See supplementary materials for image IDs.

215 Elemental compositions point towards a basaltic composition for the Mááz formation,
 216 with dominant pyroxene, feldspar and minor Fe-oxides and apatites (Wiens et al.,
 217 2022; Udry et al., this issue/Udry et al., 2022; Razzell Hollis et al., 2022). Secondary
 218 products were observed as bright salt deposits in the interstices of the Mááz formation rocks
 219 abraded patches *Guillaumes* and *Bellegarde*, likely consisting of Ca and Mg-sulfates,
 220 as well as anhydrous Na-perchlorates (Wiens et al., 2022; Meslin et al., this issue/Meslin
 221 et al., 2022; Razzell Hollis et al., 2022). Rare occurrences of Fe/Mg-carbonates have also
 222 been found in these rocks (Clavé et al., this issue/Clavé et al., 2022). An increase of the
 223 normative pyroxene proportion was observed at the lowest parts of the stratigraphy, in
 224 the Artuby ridge (Wiens et al., 2022).

225 2.2.2 The Séítah formation (Cf-f-1)

226 As Perseverance drove along the Artuby ridge and the expected Mááz/Séítah contact,
 227 many layered rocks were observed, whereas they were rare within the Mááz formation
 228 itself. Séítah's outcrops exhibit thin (up to cm-scaled) non-planar beds with a nodu-
 229 lar appearance, usually capped by more massive beds of variable thickness (Fig. 2c). A
 230 change of composition was recorded through the Mááz/Séítah contact, with increased

Mg content (up to $\sim 30\%$ in Séítah; Wiens et al., 2022), detection of olivine in the lowest stratigraphic parts of Artuby and Séítah’s rocks, and detection of carbonates (Wiens et al., 2022; Beyssac et al., this issue/Beyssac et al., 2021; Clavé et al., this issue/Clavé et al., 2022). Abraded rocks in Séítah are coarse grained, and their texture and mineralogy are consistent with olivine-rich cumulates (Liu et al., 2022; Beyssac et al., this issue/Beyssac et al., 2021; Fig. 2d). Overall, Séítah’s mineralogy is dominated by olivine and pyroxene, with scarce plagioclase, Fe-Ti oxides, Cr-rich Fe-Ti ulvospinel and some secondary alteration mineral phases like carbonates (Liu et al., 2022; Beyssac et al., this issue/Beyssac et al., 2021; Clavé et al., this issue/Clavé et al., 2022).

A few in-place outcrops near the top of the stratigraphy of Séítah differ in texture and composition from the surrounding layered, olivine-bearing rocks found in continuity. These outcrops consist of rocks of granular ”pitted” texture, and lack olivine, with elemental compositions similar to the Mááz formation rocks (Wiens et al., 2022; Udry et al., this issue/Udry et al., 2022). They correspond to the rocks of the *Content* member described in Farley et al. (2022) and Wiens et al. (2022). Albeit these rocks being classified as part of the Séítah stratigraphy in these previous studies, here we separate these pitted rocks from the non-pitted rocks of the Séítah formation due to their contrasting composition.

Both in the Mááz and Séítah formations, coatings were commonly observed on the surface of rocks. These coatings usually have a smooth texture and occur as discontinuous patches of variable thickness, with a purple tint on most enhanced color images (Garczynski et al., this issue/Garczynski et al., 2022). They show enrichment in Mg, S and H compared to the rocks underneath (Wiens et al., 2022).

The techniques of LIBS (SuperCam instrument) and X-ray fluorescence (the Planetary Instrument for X-Ray Lithochemistry, or PIXL instrument) allowed the quantification of rock chemistry based on major elements and the detection of compositions compatible with the stoichiometry of minerals listed above. The use of VISIR spectroscopy complements these approaches by being particularly sensitive to the presence of hydrated and hydroxylated mineral phases, carbonates, sulfates and iron-bearing phases ranging from iron oxides to olivines and pyroxenes (e.g., Bishop, 2020). It can assist in resolving some of the ambiguities of mineralogy that can arise when only the major elements are used, and also detect minerals with low-Z elements (i.e., H and C) that can be challenging to identify with X-ray fluorescence or LIBS. Additionally, PIXL analyses are performed via contact with the targets, which limits the number of scans (mostly performed on abraded patches during the first campaign; Razzell Hollis et al., 2022). While the LIBS operates remotely, its capabilities are limited above ~ 6.5 m distance from a target, where derived compositions are less reliable (Wiens et al., 2021; Maurice et al., 2021). The VISIR technique on the contrary is not limited by the distance and can measure spectra at long distances (theoretically, at infinity, as long as the atmospheric opacity can be adequately compensated), with a spot analyzed larger than those of the LIBS. Indeed, the field of view of the VISIR spectrometer is on the order of 1.4–2.3 mm for a mast-to-target distance of 2 m, while the surface ablated by the LIBS is on the order of <0.5 mm. As the technique does not use a laser like the LIBS or Raman techniques, it can be operated regularly with relative limited power, as long as the target is sunlit. The main minerals detected during the first year of the mission with the VISIR technique have been reviewed in Wiens et al. (2022); the goal of our study is to present them extensively as well as their significance for our understanding of the formation and evolution of rocks at Jezero crater.

3 Dataset and processing

3.1 VISIR reflectance spectroscopy

Reflectance spectroscopy, i.e., the measurement of the visible and near-infrared light ($\sim 0.4\text{--}4 \mu\text{m}$) reflected and scattered by the first microns of a surface, is a non-destructive

283 technique that has been widely used in planetary science. In particular, investigation of
 284 the reflectance in the 1–2.6 μ m range has allowed the detection and mapping of a breadth
 285 of minerals on the surface of Mars, including mafic minerals (olivine and pyroxene), iron
 286 oxides, feldspar (detectable in NIR if Fe-bearing), a variety of hydrous minerals (includ-
 287 ing phyllosilicates, sulfates, hydrated silica, zeolites, epidote, prehnite) and carbonates
 288 (e.g., Hoefen et al., 2003; Gendrin et al., 2005; Mustard et al., 2005; Poulet et al., 2005;
 289 Ehlmann et al., 2008, 2009; Brown et al., 2010; Roach et al., 2010; Carter & Poulet, 2013;
 290 Carter et al., 2013).

291 The combined techniques of visible and near-infrared provide high sensitivity to
 292 the presence of Fe-bearing minerals, due to electronic transitions absorption bands re-
 293 lated to transition elements. In the visible wavelengths, crystalline ferric oxides exhibit
 294 absorptions near 0.53–0.54 μ m and a ferric oxide absorption edge near 0.60 μ m that
 295 is particularly evident on Mars owing to the ubiquitous presence of oxidized dust. This
 296 results in reddened spectra in the visible range, with reflectance maxima typically near
 297 0.75 μ m, sometimes followed by downturns toward the near-infrared. Some ferric ox-
 298 ide minerals and hydrated iron-bearing sulfates have prominent absorptions in this μ m
 299 region. Reflectance downturns towards the near-infrared are also attributable to ferrous
 300 iron absorption bands in olivine and pyroxene, which are often also associated with shorter-
 301 wavelength peak reflectance maxima (<0.7 μ m) (e.g., Bell et al., 2008; Johnson et al.,
 302 2015). In the near-infrared, electronic absorptions centered around 1 μ m occur for most
 303 Fe-rich minerals and around 1 μ m and 2 μ m in the specific case of pyroxene (Cloutis
 304 & Gaffey, 1991; Burns, 1993; Klima et al., 2007; Clnet et al., 2011). Though the 1 μ m
 305 band center is outside of SuperCam’ spectral ranges, these bands are large enough that
 306 the high-wavelength wing produces a strong red slope at the shortest NIR wavelengths
 307 probed by SuperCam, and the low-wavelength wing can be observed partially by the longest
 308 SuperCam VIS wavelengths. Mastcam-Z multispectral observations (0.44–1.02 μ m) pro-
 309 vide additional information in this region (e.g., Rice et al., this issue; Johnson et al., 2022;
 310 Horgan et al., this issue).

311 The near-infrared is highly sensitive to the presence of alteration minerals, as the
 312 combinations and overtones of bending and stretching of groups such as H₂O, metal-OH,
 313 CO₃²⁻ and SO₄²⁻ in minerals cause various narrow absorptions in the near-infrared. In
 314 particular, H₂O-bearing minerals spectra exhibit absorption bands centered around \sim 1.4
 315 and \sim 1.9 μ m. The 1.4 μ m region can also exhibit an absorption feature due to OH.
 316 Shallow absorptions centered in the 2.1–2.5 μ m range allow the discrimination of ad-
 317 ditional molecular bonds: around 2.2 μ m with the presence of Al–OH, Si–OH and Si–
 318 O–Si, 2.28 μ m for Fe³⁺–OH, 2.35 μ m for Fe²⁺–OH, and 2.1 and 2.32 μ m for Mg–OH.
 319 The CO₃²⁻ group is identified with the co-detection of absorptions centered at \sim 2.3 and
 320 2.5 μ m, while SO₄²⁻ usually induces absorptions around \sim 1.7 and 2.4 μ m. Variability
 321 in band position can be observed with compositional change (and to a lesser extent, grain
 322 size variation), and mineralogical identification is usually performed by comparing the
 323 number and position of absorptions of a measured spectrum to those of reference spec-
 324 tra obtained in laboratories.

325 3.2 The VISIR spectrometer of SuperCam

326 SuperCam is divided into two main units: a body unit (BU), which includes three
 327 spectrometers used to measure the UV and visible light and that are primarily used by
 328 the LIBS technique, and a mast unit (MU) which hosts the infrared spectrometer (IRS).
 329 One of the three BU spectrometers is used to produce the VIS spectra shown here: the
 330 transmission spectrometer, which covers the visible 0.535–0.855 μ m range in 6000 chan-
 331 nels and with a varying FWHM spectral resolution of 0.3–0.4 nm (Wiens et al., 2021).
 332 This spectrometer uses three regions: Green (0.535–0.620 μ m), Orange (0.620–0.712 μ
 333 m), and Red (0.712–0.853 μ m). Data provided by the blue-violet (VIO) spectrometer
 334 provides information for the short wavelength (0.379–0.464 μ m) region but correspond-

ing reflectance spectra have a relatively low signal-to-noise ratio. The near-infrared range is covered by the Infrared Spectrometer (IRS), an acousto-optic tunable filter (AOTF) spectrometer located in the MU and which operates by scanning the light between 1.3 and 2.6 μm , along 256 channels (spectels) and with a spectral resolution of 32 cm^{-1} (around 5 nm at 1.3 μm , 11 nm at 1.95 μm and 20 nm at 2.6 μm ; Fouchet et al., 2022). Every SuperCam activity on a target consists of a "raster", i.e., a set of "points" (usually from one to ten) that each is associated with a LIBS, Raman, VISIR spectrum and/or RMI image. Whenever a LIBS activity was performed along with reflectance spectroscopy for a rock target, the VISIR spectra are acquired after the LIBS bursts, in order to take advantage of partial dust removal performed by the LIBS plasma (Maurice et al., 2016). For soils, the VISIR data are acquired prior to the LIBS to avoid effects of shadowing in the resulting LIBS pit. The analytical footprint of VISIR is much larger than the LIBS ablation spot on the target surface. Therefore, any structural damage due to the prior LIBS analyses on the sample is considered negligible in the VISIR data. This was demonstrated by Fau et al. (2019) for the SuperCam Raman data that has a similar analytical footprint to VIS spectroscopy and slightly smaller than for the NIR spectroscopy (Maurice et al., 2021).

The light that enters the spectrometers is collected by a Cassegrain telescope in the MU, with a field of view of 0.7 mrad for the visible spectrometer and 1.15 mrad for the IRS (Maurice et al., 2021). This corresponds to a ~ 1.4 and ~ 2.3 mm footprint respectively for a mast-to-target distance of 2 m. At this scale, several individual mineral phases can be present in the field of view of the instruments, and the measured VISIR spectra are often combinations of different spectral components. The footprint center of the IRS is offset by 0.3 mrad with regard to the other spectroscopy techniques of SuperCam that operate using the optical fiber that collects light to the BU (VIS reflectance, LIBS and Raman; Maurice et al., 2021).

3.3 Calibration overview

3.3.1 Calibration of the visible spectrometer

For VIS data used here, 50 spectra were averaged for each point. Raw VIS data were converted to radiance via an instrument transfer function derived from lab measurements with an integrating sphere (Wiens et al., 2021; Maurice et al., 2021). Relative reflectance spectra were generated by dividing the calibrated target radiance spectrum by a radiance spectrum of the onboard AluWhite SuperCam Calibration Target (SCCT), whose reflectance properties are well known (Cousin et al., 2022). An AluWhite spectrum taken on sol 20 was used as this reference up to sol 129, when the number of rows summed for the Red portion of the transmission spectrometer was updated for all subsequent spectra. Afterwards, only the first spectrum from the sol 184 set was used for calibration of post-sol 129 data, resulting in improved spectra (Legett et al., 2022). Residual issues in the VIS spectra include the narrow Cr^{3+} AluWhite emission feature at $\sim 0.694\text{ }\mu\text{m}$ (removed by interpolating the plotted spectra in this contribution), and decreased sensitivity near detector boundaries for Green/Orange ($\sim 0.62\text{ }\mu\text{m}$) and Orange/Red ($\sim 0.712\text{ }\mu\text{m}$), which can cause offsets and artifacts. Finally, relative reflectance spectra were geometrically scaled to the relevant illumination conditions by multiplying by the Mars-to-Sun distance and Solar incidence cosine ratios.

3.3.2 Calibration of the IRS

The calibration of the IRS is detailed in a companion paper (Royer et al., this issue/Royer et al., 2022) and includes dark smoothing and subtraction, reflectance conversion (also accounting for the radiometric and geometric correction), atmospheric correction and optical throughput as a function of temperature. The processing also includes removal of "glitches" (anomalously low values induced by drops of the radio frequency signal sup-

plying the transducer of the instrument) and "spikes" (anomalous values generated by the readout electronics) of the radiance data. The atmospheric correction is performed by dividing the reflectance data by $t_{CO_2}^k$, where t_{CO_2} is an atmospheric transmission model and k a constant adjusted to minimize the CO_2 main absorption feature around $2 \mu m$. The spectral calibration was performed before the flight during the instrument production. The wavelength variation varies as a function of the AOTF temperature but was estimated to be very minor (5–15 nm within a $50^\circ C$ range).

The calibrated and corrected data are affected by residual instrumental effects mainly related to the temperature of the IRBoard (the electronic component driving the IRS and located in the electronic box of the MU) and the optical box (OBOX, where the IRS is located). Though largely corrected by using AluWhite spectra at different IRBoard temperatures (Royer et al., this issue/Royer et al., 2022), this dependency can still affect some spectra by inducing low-frequency reflectance variations near $\sim 1.7 \mu m$, $\sim 2.3 \mu m$ and above $\sim 2.55 \mu m$. However, these residuals have been estimated by Royer et al. (this issue)/Royer et al. (2022) to be minor and acceptable for mineralogical identification.

3.4 Data analysis

A VISIR observation (referred to as a raster) usually consists of one to ten single-point spectra. As stated previously, the field of view of the spectrometer is a few mm-wide and as it is commonly the case in planetary spectroscopy and for other techniques as well, the measured spectra are the results of the complex mixture of the spectral signatures of each different mineral phases present in the field of view. Hence, the probability that a single type of mineral was observed in a single point is low, and the measured spectra are most likely to be combinations of different components. Additionally, the spectral predominance of some minerals can be an issue for identification. Indeed, spectral mixing of mineral signatures are non-linear with proportion, and spectral measurements on laboratory mixtures have demonstrated that a few percent of particular mineral phases can in some cases have a strong impact on the spectral information in the near-infrared (e.g., Bishop et al., 2013; Mandon, 2020; Mandon et al., 2022).

We carried out a spectral analysis to (1) identify spectral endmembers that could be indicative of mineralogical endmembers and (2) estimate the distribution of the various identified minerals along the traverse and specific outcrops. Here, we present several data types. The majority of the spectra shown in this contribution are single-point or mean target spectra. These spectra are usually the result of the complex mixing of different mineral phases: in order to highlight the contribution of isolated minerals, we performed spectral ratios for specific observations, and applied Independent Component Analysis (ICA) to some subsets of the data. These methods are described in the two following sections.

3.4.1 Spectral ratios

The use of spectral ratios is commonly performed on orbital imaging spectrometers data to highlight the spectral signatures of particular minerals occurring as mixture in the pixels (e.g., Ehlmann et al., 2009; VivianoBeck et al., 2014; Carter et al. 2015; Horgan et al., 2020). To this aim, a spectrum of a region of interest is divided by the spectrum of a nearby, spectrally neutral region (i.e., exhibiting no specific absorption bands). Another possibility for orbital data is the use of the detector column median spectrum as a denominator when there are column-dependent artifacts (e.g., Mandon et al., 2021), typically for instruments operating in pushbroom mode, such as the Compact Reconnaissance Imaging Spectrometer for Mars instrument (CRISM; Murchie et al., 2007). The ratioing method allows to highlight spectral features while minimizing the contribution of the atmosphere and aerosols (dust, clouds).

435 Normalization of SuperCam VISIR data was performed for a few observations (stated
 436 in the figures when applied) by ratioing the spectrum of a point by the median of the
 437 raster. The median is usually not spectrally neutral, but the normalization allows to high-
 438 light faint absorptions that are specific to mineral phases with varying proportions rel-
 439 ative to others in the raster.

440 *3.4.2 Independent Component Analysis (ICA)*

441 The second method is Independent Component Analysis (ICA). In this approach,
 442 a number of multivariate signals (a suite of measured IRS spectra), are separated into
 443 different sources, in order to try to isolate endmember mineral spectra. Here, the sources
 444 are non-dependent and non-Gaussian, while the mixed signals are both. The ICA aims
 445 at identifying the least Gaussian and more independent components from the measured
 446 spectra; in other words, the spectral signals that describe best the variability observed
 447 in a set of reflectance spectra.

448 In this work, the Joint Approximate Diagonalization of Eigenmatrices (JADE; Cardoso
 449 & Souloumiac, 1993) ICA algorithm was implemented on several parts of the IRS spec-
 450 tral database of SuperCam, with a fixed number of components n . Indeed, an assump-
 451 tion was made on the number of independent components that contribute to the spec-
 452 tra. As ICA components are not reflectance spectra per se, some may be difficult to in-
 453 terpret. We found that for SuperCam IRS data, n equal to two or three provides the in-
 454 dividual components that are the more easily interpretable in terms of the minerals present
 455 (i.e., with loadings that compare the best to spectra of natural samples measured in lab-
 456 oratories). A unique feature of the JADE algorithm is the use of kurtosis as a non-Gaussian
 457 criterion, which measures the dispersion of the probability weights relative to the cen-
 458 ter of distribution.

459 While ICA decomposition aims at providing physically/chemically-significant com-
 460 ponents, some caveats are associated with this method. First, there is no determination
 461 of sign or amplitude of the sources. Additionally, the method is inadequate to identify
 462 individual eigen spectra in homogenous targets (e.g., borehole tailings, whose spectra show
 463 less intra-raster variability). The results are also model-dependent; nevertheless, the JADE
 464 algorithm results shown in this contribution were compared to the results obtained with
 465 the Fast-ICA algorithm (Hyvriinen & Oja, 2000), which returned similar individual com-
 466 ponents.

467 *3.4.3 Absorption bands retrieval and main spectral parameters*

468 *Determining absorption band parameters*

469 For all the point spectra, we measured the position of the absorption centers by
 470 performing the following steps, described in Mandon et al. (2021) with an example shown
 471 in supplementary Fig. S1: first, the single-point spectra were lightly denoised using wavelet
 472 denoising (using a soft BayesShrink algorithm), then a spectral continuum was fitted us-
 473 ing the upper part of a convex hull of the NIR-only spectrum. This step was repeated
 474 until all band shoulders were satisfactorily included in the continuum. Then, the con-
 475 tinuum was divided from the data, allowing determination of the center and depth (one
 476 minus the minima of the continuum-removed spectrum) of the various absorption bands.

477 *Other spectral parameters*

478 To evaluate the broad spectral diversity of all observations, we measured the spec-
 479 tral slopes in the 1.3–1.8 μ m and 2.1–2.5 μ m ranges, and the band centers at 1.3 μ m
 480 and 2.1 μ m assuming a linear continuum shouldered at 1.8 or 2.5 μ m (Table 1). To-
 481 gether, these parameters allow a first-order evaluation of the contribution of different min-
 482 eral families. Here, olivine exhibits a strong and positive 1.3–1.8 μ m slope with a 2.1–
 483 2.5 μ m slope close to zero. As the band centers and shoulders of the ~ 1 μ m and ~ 2
 484 μ m bands of pyroxene shift with Ca/Fe/Mg relative proportion in the crystals, the val-

Table 1: List of the main spectral parameters used in this study. Note that the NIR parameters are computed on the denoised spectra (see section 3.4.3). The last section of the table lists the spectral range considered to classify some of the absorptions identified once the continuum was removed from NIR data. CRS: continuum-removed spectrum, R_λ : reflectance at a given wavelength λ , ¹: see Johnson et al. (2015).

Parameter	Value	Sensitivity	Appears in figure(s)
0.545 μ m band depth ¹	$1-R/R_c$ where R is the value of the reflectance spectrum at 0.545 μ m and R_c the value at 0.545 μ m of the continuum anchored at 0.43 and 0.60 μ m	Crystalline ferric materials	5
0.67/0.44 μ m ratio ¹	$R_{0.67\mu m}/R_{0.44\mu m}$	"Red" surfaces	5
0.75–0.84 μ m slope ¹	Slope between 0.75 and 0.84 μ m	Mafic minerals and other Fe-bearing mineral phases	5
0.60–0.84 μ m slope ¹	Slope between 0.60 and 0.84 μ m	Dusty surfaces	5
1.3–1.8 μ m slope	$1-R_{1.34\mu m}/R_{1.80\mu m}$	- Strongly positive for olivine, high-Ca pyroxene and other ferrous mineral phases, moderately positive for ferric minerals - Negative for low-Ca pyroxene	9, 10
2.1–2.5 μ m slope	$1-R_{2.15\mu m}/R_{2.5\mu m}$	- Negative for water-bearing mineral phases - Positive for pyroxene	10
2.13 μ m band depth	$1-R/R_c$ where R is the value of the reflectance spectrum at 2.13 μ m and R_c the value at 2.13 μ m of the continuum anchored at 1.93 and 2.18 μ m	Kieserite	7
Band identified in the CRS	Band position range	Sensitivity	Appears in figure(s)
1.9 μ m band	1.90–2.0 μ m	H ₂ O, OH	7, 9
2.28 μ m band	2.26–2.295 μ m	Fe ³⁺ –OH	7, 9
2.3 μ m band	2.26–2.35 μ m	Fe–OH, Mg–OH, carbonate	7, 9

485 ues of these parameters are expected to vary with both pyroxene abundance and com-
486 position. Low-Ca pyroxenes have a negative 1.3–1.8 μm slope and a positive 2.1–2.5 μm
487 m slope, while these slopes are both positive in the case of high-Ca pyroxenes. Hydrated
488 minerals have a negative 2.1–2.5 μm slope owing to water-related absorption. Spectra
489 of Fe-bearing minerals exhibit a positive 1.3–1.8 μm slope as well, though its intensity
490 is weaker in the case of Fe^{3+} compared to Fe^{2+} , the latter inducing a stronger absorp-
491 tion near 1 μm . For non-Fe-bearing hydrated minerals, this slope is usually close to zero.

492 For the SuperCam VIS spectra, simple ratios and spectral slope parameters were
493 used in the same manner as was done with MSL ChemCam passive spectra to distin-
494 guish different types of soil and rock materials (e.g., Johnson et al., 2015). For exam-
495 ple, overall "redness" (0.67/0.44 μm ratio) or the magnitude of the near-infrared drop
496 off (0.75–0.84 μm slope) helped resolve variations in ferric vs. ferrous components. Com-
497 parisons of spectral slopes and ratios between 0.60 μm and 0.84 μm provided some sen-
498 sitivity to dust coatings. Band depths at 0.545 μm provided a means to track the in-
499 fluence of crystalline ferric materials, and were computed using shoulders at 0.60 μm
500 and 0.43 μm (Clark & Roush, 1984). When calculating these spectral parameters, the
501 average relative reflectance value for a given wavelength was computed using all chan-
502 nels within ± 5 nm of that wavelength.

503 3.5 Context images

504 In this contribution, context and location of VISIR measurements are given from
505 the various color imaging instruments of the rover: the SuperCam Remote Micro-Imaging
506 (RMI; Wiens et al., 2021; Gasnault et al., 2021), the Mast Camera Zoom (Mastcam-Z;
507 Bell et al., 2021), the Wide Angle Topographic Sensor for Operations and eNgeering
508 (WATSON; Bhartia et al., 2021) and the Hazard Avoidance Cameras (Hazcams; Maki
509 et al., 2020). The RMI produces Bayer-filter images in a 18.8 mrad footprint (less than
510 4 cm for a mast-to-target distance of 2 m), at a resolution of 10 $\mu\text{rad/pixel}$ and with
511 a narrow depth of field (Wiens et al., 2021; Maurice et al., 2021). The Mastcam-Z in-
512 strument is a set of two zoomable cameras (with a focal length ranging from 26 to 110
513 mm) that produce broadband Red/Green/Blue color stereo-images as well as multispec-
514 tral reflectance spectra in the 0.4–1 μm range (Bell et al., 2021). WATSON is a cam-
515 era built on the heritage of the MSL MAHLI (Mars Hand Lens Imager) camera and mounted
516 on the rover robotic arm, allowing proximity imaging of targets in the close environment
517 of the rover (Bhartia et al., 2021). The associated images have a resolution ranging from
518 ~ 13 $\mu\text{m/pixel}$ to infinity depending on standoff distance to the target. WATSON is cou-
519 pled with the Autofocus Context Imager (ACI), which acquires ~ 10 $\mu\text{m/pixel}$ greyscale
520 images. Finally, additional context was provided by the Hazcams color images at 0.46
521 mrad/pixel (Maki et al., 2020). In this contribution, RMI, WATSON and ACI images
522 are used to show target texture, while Mastcam-Z and Hazcams color images are shown
523 for wider context (e.g., whole rock imaging).

524 The list of image IDs shown here is described in the supplementary text S1.

525 4 Results

526 As of sol 379, nearly 2000 interpretable VISIR spectra (i.e., without saturation or
527 major shadowing in the field of view) were acquired on targets in the nearby rover en-
528 vironment, including ~ 1400 spectra on ~ 150 unabraded rock targets, ~ 300 spectra on
529 ~ 20 soil targets, ~ 150 spectra on seven abraded patches of rocks and ~ 120 spectra on
530 13 tailings of coring or abrasion (Fig. 1). The list of the VISIR observations used in this
531 contribution along with the sol of execution of the activity can be found in the supple-
532 mentary table S1.

533 Most of the spectra measured on rocks of the crater floor exhibit an absorption near
 534 $1.9 \mu\text{m}$, indicating the presence of water (Fig. 3). More precisely, 94% of individual spectra
 535 on rock targets of the crater floor show a $>1\%$ band depth absorption (relative to
 536 the continuum) near $1.9 \mu\text{m}$, and the median $1.9 \mu\text{m}$ band depth is 7% (relative to the
 537 continuum). Additional shallower bands in the $2.1\text{--}2.4 \mu\text{m}$ range indicate the presence
 538 of secondary minerals (Fig. 3). The Mááz and Séítah formation rocks exhibit distinct
 539 spectral signatures, indicative of different primary and secondary mineral assemblages,
 540 as detailed in the following sections. The summary of all the mineral phases identified
 541 based on VISIR spectroscopy is shown in table 2.

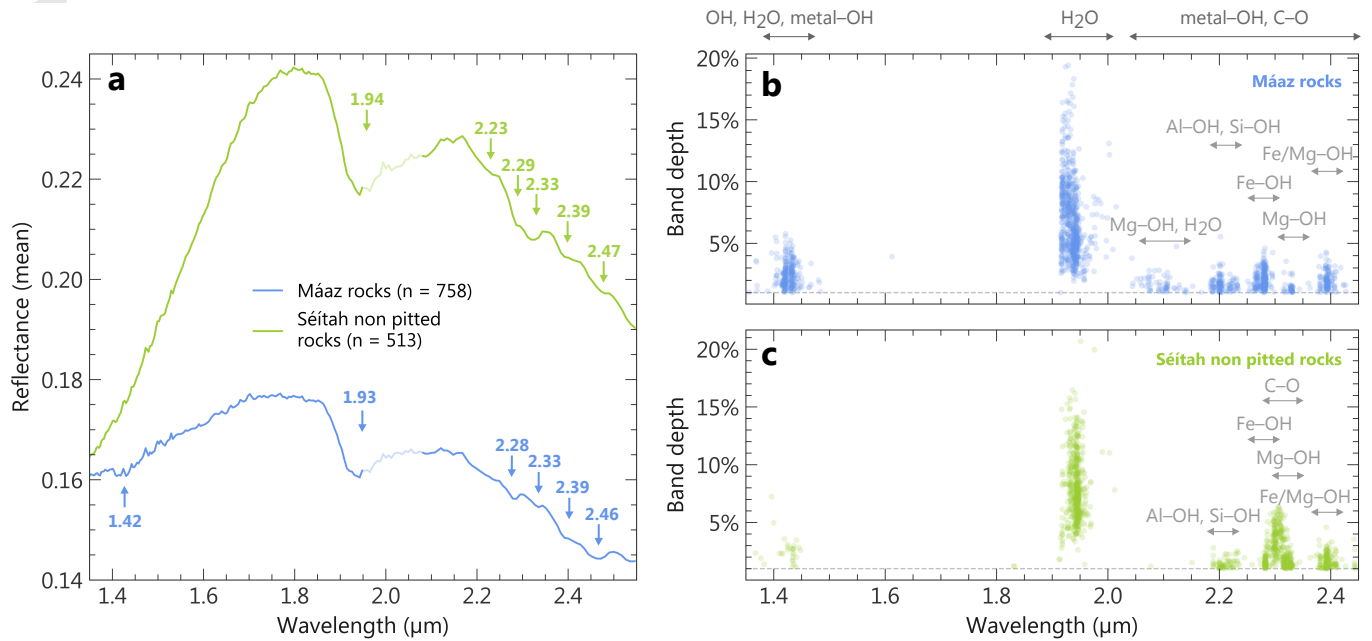


Figure 3: Near-infrared spectral signature of the rocks of the crater floor (until sol 379). (a) Mean spectra of rocks of the Mááz and Séítah formations. Parts of the spectra near $2 \mu\text{m}$ shown with lower opacity correspond to the main atmospheric CO_2 absorption domain, where correction residuals might affect the spectra. (b, c) Position and depth of the absorption bands extracted on the Mááz (b) and Séítah (c) rock spectra after continuum removal (with a threshold of 1% absorption, in agreement with a SNR of 100, met in the majority of the observations; Royer et al., this issue/Royer et al., 2022). The spectral ranges of molecular absorptions of interest are indicated with light grey arrows. Because of the thermal sensitivity of the IRS past $\sim 2.5 \mu\text{m}$, no band centered after $2.45 \mu\text{m}$ is shown as their position might be affected by this caveat. All the absorptions detected near $1.4 \mu\text{m}$ and in the $2.1\text{--}2.5 \mu\text{m}$ range are associated with an absorption near $1.9 \mu\text{m}$.

542 4.1 Dust and coatings

543 4.1.1 Dusty rocks

544 The Martian dust is a ubiquitous cover of all surfaces, and is known to affect the
 545 reflectance spectra measured on rocks – mostly by inducing a red spectral slope in the
 546 visible and flattening the spectra in the near-infrared (e.g., Le Moulic et al., 2006). How-
 547 ever, before SuperCam operations on Mars, no in situ measurement had been performed
 548 in the $1.3\text{--}2.6 \mu\text{m}$ near-infrared range. On sol 141, an experiment was conducted on the
 549 target *Salles* by acquiring VISIR spectra before and after LIBS measurements in order
 550 to assess the influence of the LIBS dust removal on the VISIR spectra. Subtle differences

551 in the VISIR spectra were noted, including a blueing of the reflectance in the VIS range
 552 as dust is usually redder compared to rocks (see supplementary Fig. S2), similar to the
 553 results obtained by MSL ChemCam instruments on dusty rock target but in that case
 554 limited to the visible range (Johnson et al., 2015). However, investigation of the RMI
 555 images shows that dust removal was minor on this target, limiting the possible interpre-
 556 tation.

557 We present in Fig. 4a the VISIR single-point spectra of the dustiest surfaces measured
 558 during the crater floor campaign. One of the dustiest surfaces (based on RMI images)
 559 was observed on the *Naltsos* target, a paver with a strong 0.545 μ m band depth
 560 related to crystalline and/or nanophase ferric oxides (Fig. 4b). Fig. 5d presents a com-
 561 parison of 0.60–0.84 μ m spectral slopes vs. 0.60/0.84 μ m ratio, which was shown by
 562 Johnson et al. (2015) to be a useful proxy for ferric dust coatings on spectrally neutral,
 563 low-albedo albedo substrates. Here, *Naltsos* plots as one of the dustiest endmembers of
 564 the Mááz targets (compared to the least dusty targets such as *Manior*).

565 Based on visual investigation of color and texture of rocks in RMI images, 13 points
 566 with thick dust coating covering the whole SuperCam VISIR field of view were identi-
 567 fied. The average spectrum from these observations is presented in Fig. 4a. In the in-
 568 frared, these dusty surfaces exhibit a relatively flat spectrum, with a faint absorption re-
 569 lated to hydration at 1.93 μ m (\sim 3–5% of absorption relative to the continuum) as well
 570 as a subtle downturn after \sim 2.3 μ m, attributable to a number of poorly crystalline water-
 571 bearing mineral phases (Fig. 4). While the 1.9 μ m absorption might be caused by hy-
 572 drated material of the rock underneath the dust cover, analysis of corresponding Mastcam-
 573 Z and RMI images shows optically-thick coating of dust in most of the field of view, likely
 574 to mask any spectral signature originating from the rock (Fig. 4b). Additionally, nearly
 575 all SuperCam dusty targets (mainly pavers) exhibit a 1.9 μ m region absorption band.

576 **4.1.2 Recently deposited dust**

577 After the rover’s landing, airborne dust started to accumulate on the rover deck
 578 and on each SuperCam calibration target (SCCT), providing the opportunity to inves-
 579 tigate the properties of the recently deposited dust. Several of the SuperCam reflectance
 580 calibration targets are enclosed in a magnetic ring, intended to deflect the magnetic frac-
 581 tion of airborne dust from the center to the edge of the SCCT (Manrique et al., 2020).
 582 On sols 72 and 111, two VISIR observations were performed on the AluWhite SCCT to
 583 check the horizontal and vertical alignment of the infrared spectrometer, measuring both
 584 the center of the SCCT and its magnetic dust-covered edges (Fig. 4c). Similar to dust-
 585 coated rocks, the spectra of the AluWhite SCCT recently covered by the magnetic frac-
 586 tion of the airfall dust exhibited a strong red slope in the visible. However, unlike the
 587 typical dust-coated rocks or soils, the VIS spectra exhibit only a weak 0.545 μ m band
 588 and a positive 0.75–0.84 μ m spectral slope. Merusi et al. (this issue) provide additional
 589 multispectral observations of the magnetic dust using Mastcam-Z data (0.44–1.02 μ m).
 590 In the IRS data, no clear absorption was observed in the near-infrared range (Fig. 4e).

591 **4.1.3 Coatings**

592 The purple-tinted material found as coatings on the rocks of the crater floor (Gar-
 593 czynski et al., this issue; Garczynski et al., 2022) has been investigated by SuperCam.
 594 Only one example is shown here, on the target *Villette*, but Garczynski et al. (this issue)/Garczynski
 595 et al. (2022) showed that the rock coatings of the crater floor share similar reflectance
 596 spectra in the VISIR. Interestingly, these purple-tinted coatings share similar features
 597 with the dust-covered surfaces. While they are darker than dusty rocks over the whole
 598 VISIR range, their spectra likewise show a red slope in the \sim 0.6–0.8 μ m range, among
 599 the strongest 0.545 μ m band depths, as well as relatively flat shapes in the NIR, along
 600 with faint 1.93 μ m absorption and downturn longward of \sim 2.3 μ m (Fig. 4a and c). These

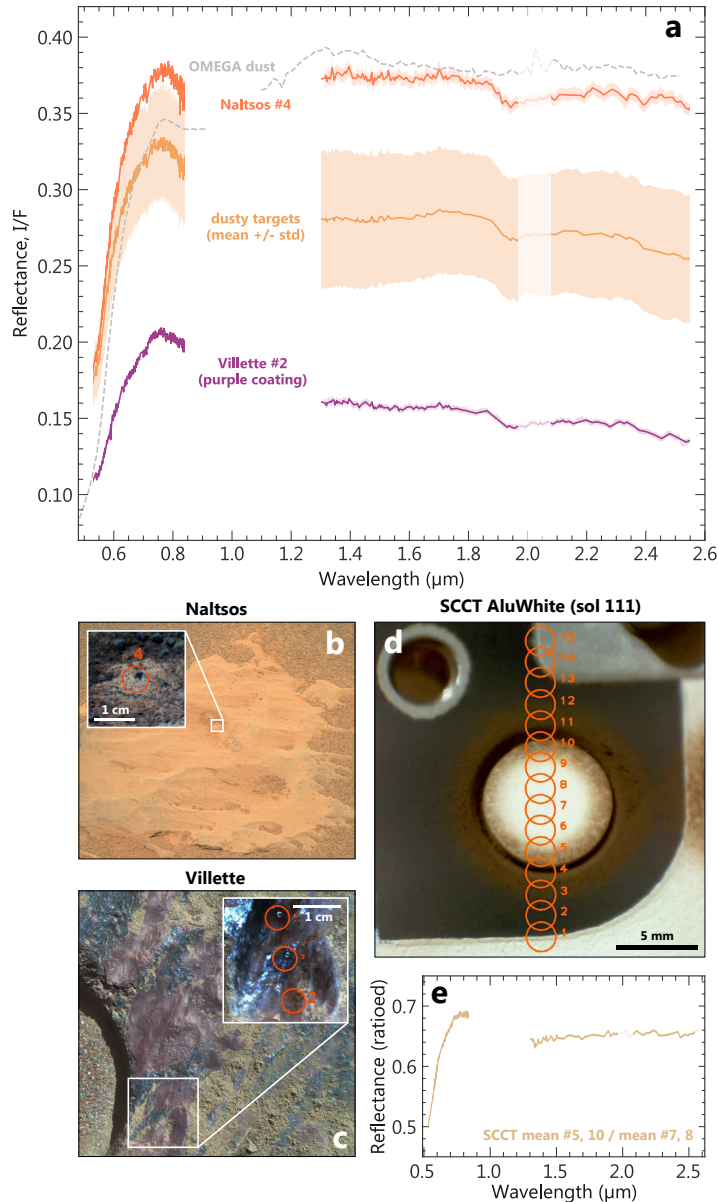


Figure 4: VISIR signature of dust-covered targets and coatings. (a) Mean spectrum of 13 points where significant dust coatings have been observed based on RMI images (list in supplementary text S3), spectrum of location #4 on the highly dusty paver *Naltsos* with corresponding Mastcam-Z image and RMI close-up in (b), and spectrum measured on location #2 of the target *Villette* coated by purplish material, with corresponding WATSON image and RMI close-up in (c). For comparison, an OMEGA orbital measurement of a dusty terrain north of Syrtis Major (Le Moulic et al., 2006) is shown. (d) RMI image and IRS pointing of a vertical observation showing dust accumulation associated with magnetized region around the SCCT AluWhite reflectance standard. Red circles indicate the location of the field of view of the IRS accounting for 68% of signal. (e) Ratioed spectrum of the SCCT edges covered in dust over the measurements centered in the middle of the SCCT shown in (d), highlighting the spectral signature of the magnetic dust deposited on the edges of the SCCT. Segments of the spectra shown with lower opacity line near $2 \mu\text{m}$ correspond to the main atmospheric CO_2 absorption domain, where residuals might affect the spectra. See supplementary text S1 for image IDs.

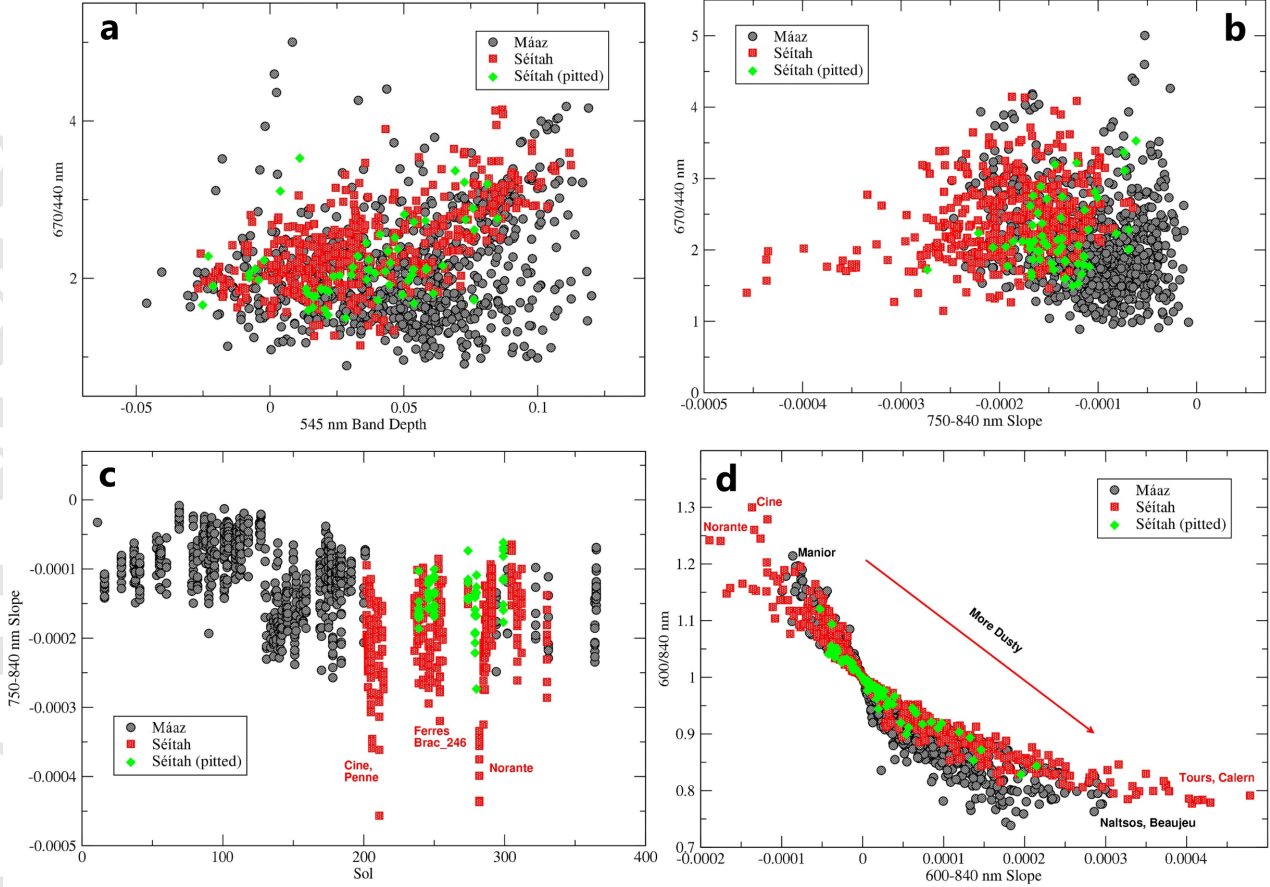


Figure 5: Visible wavelength spectral parameters for the Mááz, Séítah non-pitted and Séítah pitted rock types. (a) $0.67/0.44 \mu\text{m}$ ratio (“redness”) as a function of the $0.545 \mu\text{m}$ band depth (crystalline ferric materials). (b) $0.67/0.44 \mu\text{m}$ ratio as a function of the $0.75\text{--}0.84 \mu\text{m}$ spectral slope (Mafic minerals and other Fe-bearing phases). (c) Variations in the $0.75\text{--}0.84 \mu\text{m}$ spectral slope as a function of sol number, demonstrating the onset of strong negative slopes related to the presence of olivine as the rover entered the Séítah region on sol 201. (d) $0.60/0.84 \mu\text{m}$ ratio as a function of the $0.60\text{--}0.84 \mu\text{m}$ spectral slope (dusty surfaces), which can serve as a proxy for dust coatings on spectrally neutral, low-albedo substrates (Johnson et al., 2015).

spectral similarities suggest similar composition and a link between the modern Martian dust and the purple coating observed at Jezero crater, as discussed further in this contribution and by Garczynski et al. (this issue)/Garczynski et al. (2022). We note that these coatings are not present on all rock targets (Garczynski et al., this issue/Garczynski et al., 2022) and cannot explain the pervasive presence of an H_2O band in VISIR data of rocks.

4.2 Rocks of the Mááz formation

In the Mááz formation, the single-point spectra of the dark-toned rocks (i.e., the least-dusty rocks) most often exhibit a concave shape in the infrared range, with a pronounced $1.9 \mu\text{m}$ water absorption centered between ~ 1.92 and $1.95 \mu\text{m}$. The strongest water bands were observed in point spectra of the *Bidziil* and *Tsosts'id ts'áadah* targets, with 19% and 18% of absorption relative to the continuum respectively.

VIS spectra of the Mááz formation targets tend toward greater 0.545 μ m band depths and weaker 0.75–0.84 μ m spectral slopes than those from the Séítah targets, although there is substantial overlap (Fig. 5a and b). This results from the combined effects of overall greater contributions from ferric surfaces (dust, coatings) and no olivine in the Mááz targets.

4.2.1 Phyllosilicates

Dark-toned rocks usually exhibit an absorption at 2.28 μ m attributed to the Fe³⁺–OH bond (40% of the individual point spectra, with a threshold of 1% absorption minimum; Fig. 7). This band is often paired with additional absorptions at 1.42 μ m (OH, H₂O) and 2.39 μ m (Fe/Mg–OH), and is stronger when the water band is positioned at the lowest of the band range, at \sim 1.92 μ m (Fig. 6 and 7). These observations indicate the presence of a Fe³⁺-phyllosilicate such as nontronite or hisingerite, best expressed in the spectra of the *Bidziil* target (Fig. 6b), a vertical facet of a rock (and hence a relatively dust-free target). While nontronite and hisingerite can form in different settings, these two species have similar spectral features and are hardly distinguishable in the VISIR spectral range (Milliken & Bish, 2014). Pure nontronite or hisingerite should have a 1.9 μ m absorption band centered at shorter wavelength (\sim 1.91 μ m) and with a narrower shape, indicating that this band is likely induced by the mixture of different hydrated minerals. An additional faint absorption was observed at 2.32–2.33 μ m (Fig. 3), suggesting that a slight amount of some Mg–OH mineral(s) (such as Mg-phyllosilicates and/or brucite) or carbonate might be occurring in mixture with the Fe-phyllosilicates or that an Fe/Mg–OH phyllosilicate is present.

4.2.2 Oxyhydroxides

Overall, the 2.28 μ m band indicative of Fe-phyllosilicates is relatively shallow, exceeding 3% of absorption relative to the continuum in only 5% of the single-point spectra on the dark-toned rocks. Additionally, no clear correlation between the 1.9 and 2.28 μ m band depths was observed (Fig. 7c). These observations along with the large range of 1.9 μ m H₂O band positions point towards the presence of at least another hydrated mineral phase in the Mááz formation. Indeed, in some spectra, the 1.42, 2.28 and 2.39 μ m bands are weak or non-existent, and are associated with a strong and wider water band centered at \sim 1.94 μ m (Fig. 6b). These features are consistent with a mixing with an Fe-oxyhydroxide, such as ferrihydrite. The best example was found on sol 90 in a dark-toned filled-vesicle of the *Tsosts'id ts'áadah* target mentioned above (Fig. 6). This is in agreement with the LIBS co-analysis, which revealed \sim 80% FeOT in this target, consistent with the presence of Fe-oxyhydroxides (Wiens et al., 2022; Clavé et al., this issue/Clavé et al., 2022). In the spectra of *Tsosts'id ts'áadah*, an additional absorption near 2.46 μ m suggests that akaganeite (an Fe/Cl-oxyhydroxide) might be present as well. The laboratory spectra of other minerals such as some serpentines, brucite, carbonates, illite or muscovite can exhibit a 2.46 μ m absorption, but show additional bands in the 2.2–2.3 μ m range that are not observed here (see Carter et al., 2015 for a review).

4.2.3 Sulfates

Additionally, some spectra exhibit a significant absorption related to water (1.9 μ m band depth of \sim 10%), with a downturn longward of \sim 2.3 μ m. This was especially observed in the spectra of abraded rocks (e.g., the *Bellegarde* and *Guillaumes* targets; Fig. 6). In *Bellegarde*, spectra ratioed by the raster median have absorptions and overall spectral shape similar to those of polyhydrated sulfates (such as starkeyite, hexahydrite, schwertmannite; Fig. 6d). Though this spectral shape can also be explained by the presence of zeolite or other poorly crystalline minerals containing water, co-analysis with LIBS shows a stronger sulfate component in this target (Meslin et al., 2022). Single-

point and ratioed spectra in *Bellegarde* also exhibit a 1.93–2.13 μm "box-shaped" absorption shouldered at ~ 1.8 and $2.2 \mu\text{m}$ with an absorption maximum near $2.13 \mu\text{m}$ (Fig. 6b and d): this is usually observed in the spectra of monohydrated Mg/Fe-sulfates of the kieserite–szomolnokite solid solution (e.g., Fig. 6c). The spectra of these species also exhibit a faint absorption near $2.4 \mu\text{m}$, which is observed in the non-ratioed spectrum of *Bellegarde* shown in Fig. 6, but not in the ratioed one. The $2.13 \mu\text{m}$ feature has also been reported for one hydrated perchlorate spectrum by Hanley et al. (2009), but the strength of this band is minor in the published literature (Bishop et al., 2014). Using LIBS and Raman data, (Meslin et al., this issue/Meslin et al., 2022) reported the presence of Mg-sulfates in Máaz abraded patches, but no Fe-sulfate, making the Mg-kieserite species more likely to explain the $2.13 \mu\text{m}$ band observed in the VISIR spectra. Overall, this $2.13 \mu\text{m}$ feature is not commonly observed in Máaz rocks spectra (see section 5.2.1).

4.2.4 Other mineral phases

In some Máaz rocks, a faint absorption at $\sim 2.2 \mu\text{m}$ was observed (e.g., the *Guillaumes* target; Fig. 6b). This band can be caused by the presence of an Al-phyllsilicate, hydrated silica or gypsum.

While most of the rock targets show some degrees of hydration, some smooth and pitted rocks such as the target *Hedgehog* are exceptions, with weak to non-existent $1.9 \mu\text{m}$ absorptions, blue slopes and subtle wide absorptions around $\sim 1 \mu\text{m}$ (Fig. 6). These relatively featureless spectra might indicate a low mafic minerals content, or result from small grain size. Some extremely high-Ca, low-Fe pyroxenes also exhibit similar spectral features with subdued absorption at $2 \mu\text{m}$ (Horgan et al., 2014; Fig. 6). From LIBS data, these targets exhibit similar elemental compositions compared to the surrounding rocks, suggesting no strongly variable composition (Udry et al., this issue/Udry et al., 2022).

4.2.5 Independent Component Analysis

In the ICA model considering $n = 3$ components mixed in the abraded rocks of the Máaz formation, *Guillaumes* and *Bellegarde*, one of the resulting components exhibits a red slope in the 1.3 – $1.7 \mu\text{m}$ range as well as a broad and large absorption centered at $2.3 \mu\text{m}$, consistent with high-Ca pyroxene (Fig. 6), also detected by the LIBS and PIXL instrument (Wiens et al., 2022; Razzell Hollis et al., 2022). In the $n = 2$ model run on these same targets, one of the resulting components shows a sharp downturn past $2.3 \mu\text{m}$ as well as absorptions at 1.43 , $1.93 \mu\text{m}$, and a very weak feature at $2.13 \mu\text{m}$ (Fig. 6e), consistent with Mg-sulfates. The other component exhibits a large absorption at $1.94 \mu\text{m}$ (similar to those of the *Tsosts'id ts'áadah* spectrum), as well as shallow absorptions at 1.42 , 2.28 and $2.39 \mu\text{m}$ (similar to those of the *Bidziil* spectrum). This component likely corresponds to a Fe-phyllsilicate and Fe-oxyhydroxide mixture. ICA analysis was also performed on all rock targets of the Máaz formation, considering $n = 3$ components. One of the corresponding component is similar to the possible Fe-oxyhydroxide and Fe-phyllsilicate mixture (Fig. 6e).

4.3 Rocks of the Séítah formation: non-pitted rocks

4.3.1 Olivine

The VISIR single-point spectra of Séítah non-pitted rocks are significantly different from those measured in the Máaz formation, with a distinctly stronger absorption between ~ 0.7 and $\sim 1.8 \mu\text{m}$ typical of olivine (with possible minor contributions from other Fe-rich minerals; Fig. 3, 8 and 9a). While exhibiting a strong absorption related to olivine, these spectra also show a negative 2.1 – $2.5 \mu\text{m}$ slope (Fig. 10) as well as an

710 absorption band of water near $1.9 \mu\text{m}$ (Fig. 8), showing that hydrated products are widespread
 711 in the unit, similar to the Mááz formation rocks. The depth of this absorption is on the
 712 same order as for the Mááz rocks (Fig. 3, 7a and 9b), with the strongest water band depth
 713 being observed at 16% and 14% absorption relative to the continuum (for the targets
 714 *Issole* and *Penne* respectively). The greater olivine contributions in many of the Séítah
 715 targets (section 4.3) are expressed by the stronger negative $0.75\text{--}0.84 \mu\text{m}$ spectral slopes
 716 exemplified in Fig. 5c (targets *Cine*, *Penne*), where the major spectral change occurred
 717 around sol 200 when Perseverance entered the Séítah region.

718 4.3.2 Phyllosilicates and carbonates

719 In most of the less dusty non-pitted rocks in Séítah, an absorption at $\sim 2.3 \mu\text{m}$,
 720 whose shape and center exhibits significant variations, is observed. In some of these single-
 721 point spectra, a doublet of sharp bands showing minima centered at 2.28 and $2.32\text{--}2.33$
 722 μm respectively (Fig. 3c and *Dourbes* tailings in Fig. 8), consistent with a mixture of
 723 Fe-phyllosilicates (such as nontronite or hisingerite) and some carbonate and/or Mg-OH
 724 mineral(s) respectively. The latter could be a Mg-phyllosilicate (such as a smectite, a
 725 serpentine or talc) or a magnesium hydroxide (such as brucite). Additional very shal-
 726 low bands at ~ 2.4 and $2.47 \mu\text{m}$ were observed (respectively 1.2% and 0.7% of absorp-
 727 tion relative to the continuum in the tailings of the *Dourbes* target; Fig. 8). If real, they
 728 could suggest that talc may be a good candidate for the potential Mg-OH mineral (Fig.
 729 8a, Brown et al., this issue/Brown et al., 2022), however, the two bands are near detec-
 730 tion limit. In some other spectra, the $2.3 \mu\text{m}$ band does not exhibit any doublet and
 731 instead shows a single, wider, and usually stronger absorption centered at $2.32 \mu\text{m}$ (Fig.
 732 8 and 9). While a $2.32 \mu\text{m}$ absorption was also observed in Mááz rocks spectra, it is gen-
 733 erally stronger in those of Séítah rocks (Fig. 9c).

734 No correlation between the 1.9 and $2.3 \mu\text{m}$ band depths was observed (Fig. 7d),
 735 suggesting that the $1.9 \mu\text{m}$ band is explained by minerals with no Fe/Mg-OH bands (such
 736 as ferrihydrite), that the hydration of the metal-OH bearing phase itself is variable, which
 737 would not be unexpected for clay minerals (interlayers more or less collapsed), or that
 738 at least one non-hydrated mineral phase contributes to the absorption near $2.3 \mu\text{m}$. In
 739 the *Garde* abraded patch, a shallow band at $2.53 \mu\text{m}$ is observed, together with an absorp-
 740 tion at $2.32 \mu\text{m}$ (Fig. 8e). This absorption near $2.5 \mu\text{m}$ can be due to the presence
 741 of carbonates, although some spectra of clay minerals (e.g., serpentine) can also exhibit
 742 this feature. On the target *Garde*, Clavé et al., this issue/Clavé et al. (2022) reported one
 743 of the strongest signatures of carbonates of all the LIBS and Raman spectra measured
 744 on the crater floor. Hence, we favor the hypothesis that the absorption near $2.5 \mu\text{m}$ ob-
 745 served in this specific target is related to carbonates. Notably, this band is weaker than
 746 the $2.3 \mu\text{m}$ band, whereas the opposite would be expected if it were solely due to car-
 747 bonate. As such, it likely represents a mixture of carbonates with Fe/Mg-phyllosilicates
 748 (which also contribute to the $2.3 \mu\text{m}$ absorption). Once the continuum is removed, the
 749 2.3 and $2.5 \mu\text{m}$ bands observed in the *Garde* target are centered at 2.31 and $2.53 \mu\text{m}$
 750 respectively. This is in agreement with bands associated with Fe/Mg-carbonates, and
 751 consistent with the composition inferred from LIBS data (Clavé et al., this issue/Clavé
 752 et al., 2022) and from orbit at the regional scale (Ehlmann et al., 2008).

753 Given the implication of observing an absorption near $2.5 \mu\text{m}$, its significance was
 754 investigated in more detail in the companion paper by Royer et al. (this issue)/Royer
 755 et al. (2022): in the *Garde* spectra, the absorption at $2.53 \mu\text{m}$ is observed at band SNR
 756 > 3 in 5 single-point spectra out of 27 (SNR = 1 being the band detection threshold,
 757 as the signal is equal to the estimated noise). In particular, the *Garde* sol 209 #8 spec-
 758 trum exhibits an absorption at $2.53 \mu\text{m}$ at a band SNR of 7, which indicates that it is
 759 likely not induced by instrumental effects.

760 By comparison with the spectra of mixtures of carbonate and olivine, the carbon-
 761 ate proportion in the field of view of the IRS is likely minor. Indeed, as shown in Fig.
 762 8d and e, the relative band depths at 2.5 μ m (carbonate) and 1.3 μ m (olivine) in the
 763 *Garde* spectrum are weaker than in the 95 wt.% olivine and 5 wt.% carbonate mixture
 764 spectrum measured by Mandon et al. (2022). Analysis of the SuperCam calibration tar-
 765 gets has shown overall weaker contrast and band depth on the IRS spectra measured on
 766 Mars compared to laboratory measurements (Royer et al., this issue/Royer et al., 2022),
 767 and grain size and complex mixture can greatly affect the depth of the absorption bands
 768 (e.g., Crowley, 1986; Zaini, Van der Meer, & Van der Werff, 2012), so great care should
 769 be taken when comparing to laboratory measurements of mixtures. Still, observations
 770 of a band near 2.5 μ m are very scarce in the spectral dataset of the crater floor and ob-
 771 served at maximum 3–4% band depth which is very weak. This is in agreement with the
 772 low proportion of carbonates in the Séítah rocks inferred by Clavé et al. (this issue)/Clavé
 773 et al. (2022).

774 On the orbital data, the southern part of Séítah exhibits relatively weak carbon-
 775 ate signature, which is in agreement with the scarce observations of the absorption near
 776 2.5 μ m (Horgan et al., 2020; supplementary Fig. S3b). After the first campaign of Mars
 777 2020 and before reaching the base of the deltaic deposits, Perseverance reached the West-
 778 ern region of Séítah, which from orbit show stronger carbonate signatures. Consistently,
 779 VISIR reflectance spectra of the rocks at this location exhibit distinct bands at 2.53 μ
 780 m, similar to the *Garde* observation (supplementary Fig. S3a).

781 4.3.3 *Oxyhydroxides*

782 In *Issole*, a non-pitted rock, a strong (16% of absorption relative to the continuum)
 783 and large hydration band at \sim 1.9 μ m was observed, as well as subdued bands in the
 784 metal–OH absorption region, in addition to the olivine absorption typical of Séítah rocks
 785 (Fig. 8c). Apart from the olivine absorption, these spectral features are similar to those
 786 observed in the spectrum of *Tsosts'id ts'áadah*, interpreted as Fe-oxyhydroxide-bearing.
 787 As such, this type of minerals might be common to the Séítah and Mááz formations. Still,
 788 these spectral features are overall rarely observed in the Séítah rocks spectra.

789 4.3.4 *Other mineral phases*

790 In the abraded patch *Quartier*, some light-toned areas were observed, similarly to
 791 the *Bellegarde* and *Guillaumes* patches in the Mááz formation. One of these light-toned
 792 features was largely included in the field of view of some SuperCam VISIR measurements
 793 (Fig.8j); ratioing the corresponding spectrum by the raster median highlighted spectral
 794 features similar to those in the *Bellegarde* target that were interpreted to be due to the
 795 possible presence of sulfate and/or poorly crystalline water-bearing materials (Fig. 8b).

796 Finally, an absorption shoulder was observed in Séítah rocks at 2.22–2.23 μ m (Fig.
 797 3). This can be induced by both Al–OH mineral phase(s) or hydrated silica. In LIBS
 798 data, several points high in silica have been observed and are unlikely to correspond to
 799 quartz in a mafic rock consisting of \sim 40% olivine (Wiens et al., 2022), and might be re-
 800 lated to potential secondary hydrated silica (e.g., opal or chalcedony) causing the ab-
 801 sorption at 2.2 μ m. Given the weak absorption associated with this band, both Al–OH
 802 phases and hydrated silica remain a possibility to explain its occurrence in Séítah rocks.

803 4.3.5 *Independent Component Analysis*

804 Similarly to the Mááz rocks, one of the ICA components of abraded rocks NIR spec-
 805 tra in Séítah shows a red slope in the 1.3–1.6 μ m range as well as a broad and large ab-
 806 sorption centered at 2.3 μ m, consistent with high-Ca pyroxene (Fig. 8). Another com-
 807 ponent exhibits similar spectral features as olivine with carbonate and/or Fe/Mg-phyllosilicates.

808 The ICA models run on Séítah rocks have not yet been able to distinguish olivine from
 809 secondary minerals products, and while an unaltered pyroxene component could be re-
 810 trieved, no pristine olivine component was observed. This might suggest that the pro-
 811 portion of the alteration products varies as the olivine proportion does, and that they
 812 are preferentially spatially associated with olivine compared to pyroxene, at the scale of
 813 the IRS field of view (e.g., in cracks or on the rims of the olivine crystals). This is con-
 814 sistent with olivine usually altering more rapidly than pyroxene.

815 4.4 Rocks of the Séítah formation: pitted rocks

816 In total, seven different pitted rocks (the rocks near the top of the stratigraphy of
 817 Séítah) have been measured in the VISIR by SuperCam. Unlike the other rocks in Séítah,
 818 their single-point spectra do not exhibit the wide absorption between ~ 0.7 and $\sim 1.8 \mu$
 819 m typical of olivine, but rather exhibit similar spectral shape as the Mááz rocks in the
 820 overall VISIR range (Fig. 8b). In particular, the spectral slopes in the $1.3\text{--}1.8 \mu$ m, 2.1--
 821 2.5μ m and $0.75\text{--}0.84 \mu$ m ranges, are on the same order than the spectra measured in
 822 Mááz rocks (Fig. 5 and 10). The lack of absorption indicative of olivine is in agreement
 823 with the Mg-poor and olivine-lacking composition inferred from LIBS data on these pit-
 824 ted rocks (Wiens et al., 2022).

825 4.5 Soils

826 During the crater floor campaign, different types of regolith were observed on the
 827 crater floor (Vaughan et al., this issue/Vaughan et al., 2021; Cousin et al., this issue/Cousin
 828 et al., 2022). In particular, we distinguish fine soils, which are associated with μ m-scale
 829 particles coated with dust (Hausrath et al., this issue/Hausrath et al., 2022), and coarse
 830 soils, which consist of an assemblage of fine and coarser mm-sized materials. On the crater
 831 floor, the latter is usually found on eolian bedforms and much of the coarser fraction con-
 832 sists of dark-toned mm-sized granules (Fig. 11). In the VISIR data, both types of soils
 833 have distinct spectral signatures in the near-infrared. The spectra of fine soils, such as
 834 the *Cheshkeh* target, exhibit two large absorptions in the $\sim 0.7\text{--}1.7 \mu$ m and $\sim 1.7\text{--}2.4$
 835 μ m ranges, consistent with pyroxene, possibly mixed with olivine (Fig. 11 and supple-
 836 mentary Fig. S4). The second absorption is broadly centered around $2.0\text{--}2.1 \mu$ m, cor-
 837 responding to pyroxene of intermediate composition – either resulting from the mixing
 838 of pyroxenes of different Ca-composition or from a unique type of pyroxene with inter-
 839 mediate Ca content. The spectra measured on the coarse-grained soils, such as the *Has-*
 840 *taa* sand ripple target, show a deeper absorption between ~ 0.7 and 1.7μ m and do not
 841 exhibit the $2.0\text{--}2.1 \mu$ m broad band observed in the soils spectra (Fig. 11). This is con-
 842 sistent with a significant enrichment in olivine compared to the fine soils (though grain
 843 size and and Fo content influence the olivine signature as well), in agreement with the
 844 higher content of Mg and stoichiometry consistent with almost pure olivine inferred from
 845 LIBS data on these dark-toned grains (Cousin et al., this issue/Cousin et al., 2022). This
 846 variability in composition is easily observed in Fig. 10, where the coarse soils plot along
 847 the olivine trend in the spectral slopes parameter space, and the finer soils plot between
 848 the olivine and pyroxene trends.

849 Fine and coarse soils share overall similar spectral shapes whether observed on the
 850 Mááz or Séítah formations (supplementary Fig. S4). Slight differences were observed:
 851 in fine soils spectra, the $2.1\text{--}2.5 \mu$ m slope is of 4% on average for both formation, while
 852 the $1.3\text{--}1.8 \mu$ m slope is of 16% and 22% on average on the Mááz and Séítah formation
 853 respectively. The latter suggests slightly more mafic minerals in the fine soils of the Séítah
 854 formation. In line with this, coarse soils exhibit a $1.3\text{--}1.8 \mu$ m slope of 25% and 32% on
 855 average on the Mááz and Séítah formation respectively. The $2.1\text{--}2.5 \mu$ m slope is sim-
 856 ilar for both types of coarse soils, with 0.5% and 1% on average on Mááz and Séítah.

857 The spectra measured by the IRS on the soils commonly exhibit a shallow absorp-
858 tion related to hydration at $\sim 1.9 \mu\text{m}$. This band was observed at similar strength for
859 both types of soils, at 4 and 3% absorption relative to the continuum for the fine and
860 coarse soils respectively (Fig. 7a). These values are significantly lower than for obser-
861 vations of rocks, which, for dark-toned (i.e., less dusty targets) is of 8% relative to the
862 continuum. In the spectra of coarse soils, additional absorptions at 2.28 and $2.32 \mu\text{m}$,
863 or $2.30 \mu\text{m}$ were observed, attributed to a combination of Fe-OH and Mg-OH phases
864 (Fig. 11 and supplementary Fig. S4). The large absorption in the $\sim 0.7\text{--}1.7 \mu\text{m}$ range
865 induced by olivine and these two shallow bands around $2.3 \mu\text{m}$ observed in coarse soils
866 in both two units of the crater floor are spectral characteristics shared with the spectra
867 measured on the non-pitted rocks of the Séítah formation, implying a common compo-
868 sition between the dark-toned granules in the soils and the Séítah rocks.

869 ICA analysis of the regolith spectra confirms the results above and highlights the
870 three following components for soils (in no preferential order): a first component con-
871 sistent with intermediate-Ca pyroxene or a mixture of various pyroxene types of distinct
872 composition (broad absorption centered at $\sim 2 \mu\text{m}$); a second component consistent with
873 olivine mixed with carbonates and/or Fe/Mg-phyllsilicates (large absorption in the 1.3--
874 $1.8 \mu\text{m}$ range and shallow absorptions centered in the $2.28\text{--}2.32 \mu\text{m}$ range), which is
875 similar to Séítah rocks; and a third component corresponding to some hydration of un-
876 certain nature showing a single absorption at $1.94 \mu\text{m}$ (Fig. 11).

877 While the coarser soils share spectral similarities with the Séítah rocks (a wide 0.7--
878 $1.8 \mu\text{m}$ absorption, shallower ~ 1.9 and $2.3 \mu\text{m}$ absorptions), their $2.1\text{--}2.5 \mu\text{m}$ slope
879 is weaker (Fig. 10). This might be explained by the presence of finer, pyroxene-rich soils
880 in the field of view of the IRS or by a weaker water content in the coarse soils compared
881 to Séítah rocks, consistent with their weaker $1.9 \mu\text{m}$ band.

882 4.6 Cached samples

883 We report in Fig. 12 the spectral signatures associated with the different targets
884 related to the sampled rocks: (1) natural and (2) abraded surfaces of the sampled rocks
885 and (3) tailings resulting from their coring or abrasion. The corresponding spectra are
886 compared to the mean spectra of each of the geologic unit the samples are related to,
887 as a means to estimate their representativeness. During the crater floor campaign, eight
888 rock cores were collected and sealed, comprising two paired samples at each of the fol-
889 lowing outcrops: *Rochette* and *Sid* in the flat-lower and massive-upper Mááz formation
890 respectively, and *Brac* and *Issole* in the Séítah formation (Fig. 1, see the supplementary
891 text S2 for the list of target names). No sample was acquired from the pitted rocks of
892 the Séítah unit.

893 After a coring activity, no measurement was performed by the science payload on
894 the collected sample. SuperCam analyses were performed on the boreholes of the drills,
895 but these targets were usually not sunlit, which complicates the interpretation of reflectance
896 spectra. The abraded surfaces of the rock sampled on the crater floor are the freshest
897 surfaces measured by SuperCam and the more likely to represent the lithologies of the
898 sealed cores. These abraded targets have usually stronger absorptions than the natural
899 rocks (Fig. 12), which is expected given their low to absent dust cover and/or weath-
900 ered coatings.

901 The abraded *Rochette* and *Sid* outcrops have mean VISIR spectra similar to the
902 mean signature of the Mááz rocks: they share a comparable overall spectral shape in the
903 $0.5\text{--}2.5 \mu\text{m}$ range, including similar $0.545 \mu\text{m}$ band depths and $0.75\text{--}0.84 \mu\text{m}$ spectral
904 slopes. In the near-infrared they exhibit similar absorptions at 1.43 , 1.93 , 2.28 , 2.39 and
905 $2.46 \mu\text{m}$ (Fig. 12a and b). This indicates that the samples collected at *Rochette* and *Sid*
906 are overall representative of the Mááz formation in terms of the alteration minerals as-
907 semblage present in the rocks. These two Mááz abraded rocks are similar in terms of the

spectral intensity of the 1.9 μ m water absorption (8% average, relative to the continuum) as well as the 2.28 μ m Fe-phyllsilicate band (1.5% average).

The abraded *Brac* and *Issole* outcrops are representative of the S  itah formation, and exhibit similar spectra compared to the rocks measured in this unit: negative 0.545 μ m band depths, but strong absorption between 0.7 and 1.8 μ m consistent with the presence of olivine, possibly mixed with other ferrous components. They also exhibit associated bands at 1.94, 2.3, 2.39 and 2.46 μ m related to the secondary mineral phases discussed previously for S  itah rocks. Both abraded rocks have similar 1.3–1.8 μ m olivine/ferrous mineral band depth (45% average relative to the continuum at 1.3 μ m), Fe/Mg-phyllsilicate and/or carbonate 2.3 μ m band (5% average). The 1.9 μ m water band is slightly stronger at *Issole* compared to *Brac* (11 and 8% average respectively).

Interestingly, at *Rochette* and *Sid*, the abraded rock and tailings spectra exhibit significantly different spectral signatures in the infrared. While strong H₂O and metal–OH bands were observed in the abraded spectra, similarly to other M  az rocks, their tailings exhibit flatter spectra, along with subdued absorption bands (Fig. 12). Potential interpretations of this phenomenon are provided in the discussion section.

5 Discussion

5.1 Igneous nature of the crater floor

The VISIR spectra measured during the first year of the mission are in agreement with parallel studies proposing that the crater floor consists of igneous rocks, with altered basaltic rocks on top of the stratigraphy and olivine-rich rocks at the bottom (Farley et al., 2022; Wiens et al., 2022; Liu; et al., 2022; Beyssac et al., this issue/Beyssac et al., 2021; Udry et al., this issue/Udry et al., 2022).

5.1.1 The M  az formation

In the M  az formation (east of the S  itah region, Artuby excluded), Wiens et al. (2022) reported basaltic compositions with mineral abundances (derived from LIBS CIPW norms and alteration phases excluded) of \sim 45% feldspar and \sim 43% pyroxene (mostly as Fe-rich augite and pigeonite; Udry et al., this issue/Udry et al., 2022). Oxides might also be present in the M  az rocks. Fe-poor feldspars do not exhibit strong distinct absorption bands in the spectral range covered by SuperCam, making pyroxene the main primary mineral detectable in VISIR in the M  az formation. Depending on grain size, hydrated minerals can have low detection thresholds in reflectance spectroscopy compared to mafic minerals (e.g., Thollot, 2013; Mandon et al., 2022), likely explaining the dominance of their signature in the M  az rocks spectra. Still, our ICA analysis suggested the presence of high-Ca pyroxene in some targets, in agreement with the LIBS compositions (Udry et al., this issue/Udry et al., 2022). No evidence of low-Ca pyroxene was observed based on the analysis of the VISIR spectra.

In orbital data over Jezero’s delta and watershed, the signatures of low-Ca pyroxene, as well as olivine and carbonate are significant (Horgan et al., 2020). The fact that the corresponding signatures were not observed in the M  az formation rocks strengthens the hypothesis favored by Farley et al. (2022), Wiens et al. (2022) and Udry et al. (this issue)/Udry et al. (2022) that this unit is not composed of igneous materials transported from the watershed, but instead emplaced in situ through igneous processes (such as lava flows or pyroclastic deposits).

952

5.1.2 The Séítah formation

953

954

955

956

Similarly to Máaz, the mineralogical assemblage observed in VISIR in the Séítah rocks does not include the low-Ca pyroxene signature observed on the watershed and on the delta, possibly favoring again the in situ magmatic/volcanic emplacement over the sedimentary hypothesis, consistent with Liu et al. (2022).

957

958

959

960

961

962

963

964

965

966

967

968

969

970

971

972

973

974

Consistent with Wiens et al. (2022), no olivine was detected with the VISIR technique in the Séítah pitted rocks or in the Máaz formation, but it was detected in all the spectra of the Séítah non-pitted rocks. Farley et al. (2022) and Wiens et al. (2022) proposed various scenarios to explain this change of mineralogy between Máaz and Séítah, accounting for the cumulate texture of olivine-bearing rocks described by Liu et al. (2022). In the first scenario, the terrains observed by Perseverance on the crater floor were formed after the differentiation of a single melt by gravity settling of olivine crystals (Brown et al., this issue/Brown et al., 2022). Alternatively, the Máaz formation (and possibly Artuby) could have formed from consecutive lava flows, after emplacement and erosion of the cumulate filling the crater floor. In these hypotheses, the origin of the cumulate formation is unclear, and could result from the differentiation of an intrusive or thick extrusive igneous flow, or from an impact melt. Layers observed from orbital data in the regional Nili Fossae olivine-bearing unit drape the eroded rim of Jezero North to the delta, discarding an intrusive origin or a formation related to the older giant impact of Isidis (Mandon et al., 2020). Hence, if the Séítah formation exposes rocks of the regional olivine-bearing unit, an effusive scenario would be favored. Until further exploration outside of Jezero crater, the clarification of the relationship between the rocks exposed at Jezero and the regional olivine-bearing unit, as well as its exact origin, remain to be determined.

975

5.2 Alteration of the crater floor

976

5.2.1 Nature of the hydration

977

978

979

980

981

982

983

984

985

986

987

988

989

990

991

From orbital data, the crater floor of Jezero appears poorly hydrated, with primary mafic minerals dominating the CRISM spectra measured on Máaz and Séítah (e.g., Goudge et al., 2015; Horgan et al., 2020). Surprisingly, most of the SuperCam reflectance spectra of the rocks of the crater floor exhibit an absorption near $1.9 \mu\text{m}$, related to water. Fig. 7 and 9 show that the depth of the $1.9 \mu\text{m}$ band has comparable strength in the spectra of Séítah and Máaz rocks (slightly more intense in Máaz), pointing to roughly similar hydration level in both formations. Pavers exhibit shallower hydration bands than massive dark-toned rocks, likely owing to their substantial dust cover which was often not completely removed within the VISIR fields of view by LIBS bursts prior to acquisition, and/or more adherent coatings. Abraded rocks of the upper part Máaz stratigraphy (*Alfalfa* target within the *Sid* sample site) and lower Máaz stratigraphy (*Guillaumes* and *Bellegarde* targets within the *Roubion* and *Rochette* sample sites, respectively) exhibit comparable average $1.9 \mu\text{m}$ absorption depths: 8% for the *Alfalfa* and *Bellegarde* targets and 11% for the *Guillaumes* target. This suggests overall similar hydrated mineral phases content throughout the Máaz stratigraphic column.

992

993

994

995

996

997

998

999

1000

Several hydrated minerals that might cause the $1.9 \mu\text{m}$ absorption have been identified using VISIR data: Fe-oxyhydroxides, phyllosilicates, sulfates and if hydrated, carbonates (see section 4). In reflectance spectroscopy, the strength of the absorption bands cannot be readily used to derive absolute mineral proportions, as complex effects of texture, grain size and porosity also affect the spectra. Here, while the hydration band at $1.9 \mu\text{m}$ was observed at a strength up to $\sim 20\%$ relative to the continuum, the absorption bands in the $2.1\text{--}2.5 \mu\text{m}$ range are faint (max. $\sim 5\%$), pointing to possibly low proportions of phyllosilicates, sulfates and/or carbonates in the fields of view of the instrument.

1001 From the VISIR spectra only, it is challenging to infer whether the Fe/Mg-carbonates
 1002 detected at Séítah are hydrated as they are likely observed as mixtures with phyllosil-
 1003 icates, which exhibit strong water bands. Fe-carbonates are nominally anhydrous, whereas
 1004 Mg-carbonates are more complex, with several hydrated forms found in nature, such as
 1005 hydromagnesite or nesquehonite (whose stability in the Martian environment remains
 1006 uncertain; Calvin et al., 1994; Harner & Gilmore, 2015). However, other than carbon-
 1007 ates, similar minerals were observed between the Máaz and Séítah rocks without signif-
 1008 icant variation of the water band depth, suggesting a non-significant hydration of car-
 1009 bonates. This is consistent with LIBS data, in which carbonate detections are not as-
 1010 sociated with intense H emission lines compared to other targets (Clavé et al., this issue/Clav
 1011 et al., 2022).

1012 In Máaz, the 2.2 μ m absorption possibly attributed to gypsum, Al-phyllosilicates
 1013 or hydrated silica was observed at low intensity, close to the noise level (at $\sim 1.5\%$ rel-
 1014 ative to the continuum), suggesting a minor influence of the corresponding hydrated min-
 1015 eral phase. Faint 2.32 μ m absorptions are also observed and attributed to a Mg-OH phase,
 1016 that could be a Mg-phyllosilicate and/or a Mg-hydroxide. In Máaz, the 2.32 μ m absorp-
 1017 tion is faint and also close to the noise level (Fig. 3), suggesting a weak contribution of
 1018 potential Mg-phyllosilicate to the hydration. In Séítah, this band was observed at stronger
 1019 intensity and was attributed to either carbonates, Mg-hydroxide, serpentine, Mg-smectite,
 1020 and/or talc. Talc, serpentine and Mg-hydroxide spectra do not exhibit an absorption at
 1021 1.9 μ m (or subdued in the case of serpentine) due to their lack of structural water and
 1022 are not expected to bear on structural hydration in Séítah.

1023 Mg-sulfates are one candidate to explain the drop in reflectance past 2.3 μ m ob-
 1024 served here as well as an absorption at $\sim 2.13 \mu$ m. As the intensity of the 2.3 μ m drop
 1025 can be affected by thermal effects residuals after the calibration (Royer et al., this issue;
 1026 Royer et al., 2022), we measured the depth of the 2.13 μ m band (shouldered at 1.93 and
 1027 2.18 μ m), as a means to track the signature of Mg-sulfate in the Máaz formation (Ta-
 1028 ble 1). Fig. 7b shows that this absorption is rarely observed and is associated with rel-
 1029 atively low 1.9 μ m band depths, with the exception of the abraded patch *Bellegarde*,
 1030 suggesting a relatively low influence of Mg-sulfates in the VISIR spectra of rocks.

1031 No correlation between the band center and the depth of the 1.9 μ m absorption
 1032 was observed (Fig. 7b). However, the endmember spectrum of location #4 on *Bidziil* dis-
 1033 plays one of the strongest 1.9 μ m band depths and is interpreted as consistent with Fe-
 1034 phyllosilicate. Because the 1.9 μ m absorption in nontronite and hisingerite spectra is
 1035 centered at low wavelength (~ 1.91 - 1.92μ m) compared to other hydrated mineral phases
 1036 detected here ($> 1.93 \mu$ m), an Fe-phyllosilicate cannot alone explain the widespread hy-
 1037 dration on the crater floor. The rocks of the Máaz formation have NIR spectral shapes
 1038 consistent with hydrated Fe-bearing minerals (Fig. 6 and 10), and it is likely that the
 1039 main bearer of hydration consists of a mixture of Fe-phyllosilicate and Fe-oxyhydroxides
 1040 (as also evidenced by ICA results). As shown above, the spectral signature of other can-
 1041 didate hydrated minerals (including sulfates, and possibly Al-phyllosilicates, hydrated
 1042 silica, perchlorate and zeolites) appear less dominant on the spectral dataset of Jezero's
 1043 crater floor and hence probably have a minor influence on the hydration band observed
 1044 at 1.9 μ m.

1045 *Hydration of rock tailings and soils*

1046 The wide diversity of targets measured by SuperCam revealed some variability in
 1047 water band depth among different target types. In particular, the spectra of the tailings
 1048 resulting from drill or abrasion activities often exhibited a subdued 1.9 μ m water band
 1049 compared to spectra acquired on their corresponding natural rock surface (e.g., on the
 1050 *Rochette* outcrop in Fig. 12). Heating during drilling and abrasion is not sufficient to
 1051 dehydrate the detected minerals. Hence, this could be due to a reduced proportion of
 1052 hydrated phases with depth from an outer, more weathered surface to a more pristine
 1053 interior. The reflectance spectra measured on rocks usually have weaker bands compared

1054 to their crushed equivalent, as particles are welded together (Hapke, 1993). Here, the
1055 tailings are very fine powders (aggregates of a few microns), favoring reduced optical paths,
1056 hence possibly reducing spectral contrast and absorption strengths. Overall, one can ex-
1057 plain the different spectral shape of the rock tailings by a change of optical regime, and
1058 not necessarily by a less altered interior. We note that the spectra of *Rochette* and *Brac*'s
1059 tailings have a lower reflectance and spectral contrast compared to those of *Sid* and *Is-*
1060 *sole*. Because the spectra are not corrected for photometric effects, it is possible that the
1061 higher phase angles associated with the *Sid* and *Issole* observations (41–89°) compared
1062 to the *Rochette* and *Brac* observations (26–48°) might also be responsible for the differ-
1063 ence (in that case, *Sid* and *Issole*'s tailings would be more backscattering than *Rochette*
1064 and *Brac*'s tailings).

1065 We noted that the reflectance spectra measured by SuperCam on soils of Jezero
1066 crater usually have weaker water absorption bands compared to the spectra of the crater
1067 floor rocks (Fig. 7a). This is consistent with the low hydration levels inferred from NIR
1068 orbital spectra and the extensive soil coverage on the Cf-fr. However, in LIBS data, soil
1069 targets are associated with stronger H emission lines (Cousin et al., this issue/Cousin
1070 et al., 2022), in apparent discrepancy with our results. The H signal in LIBS spectra is
1071 highly affected by matrix effects (e.g., Schrder et al., 2015), which could (at least par-
1072 tially) induce artificially stronger H signal in soils compared to rocks. Because the wa-
1073 ter absorption strength in the reflectance spectra is also influenced by factors not related
1074 to hydration (typically, the grain size or roughness of the sample) and considering the
1075 matrix effects affecting hydrogen in LIBS data, it is challenging to determine precisely
1076 how the hydration of the regolith compare to the Jezero crater floor rocks.

1077 **5.2.2 Alteration history**

1078 One of the implications of our study regarding the history of Jezero is that water-
1079 rock interactions affected the crater floor broadly, with hydrated minerals present to some
1080 degree in most of the rocks analyzed. The interpreted mineralogical assemblages repre-
1081 sent a diversity of possible secondary mineral phases, with both Fe³⁺ and Mg-phylosilicates,
1082 Fe-oxyhydroxides, carbonates and sulfates. Al-phylosilicates do not appear to be abun-
1083 dant (in agreement with orbital observations). These types of minerals appear to be com-
1084 mon to the Máaz and Séítah units, implying a similar, possibly contemporaneous, altera-
1085 tion. The exception is the presence of carbonates, which seems to be restricted to the
1086 Séítah formation. Clavé et al (this issue)/Clav et al. (2022) reported LIBS compositions
1087 consistent with their presence in Máaz rocks as well, but the corresponding carbonates
1088 occurrences appear to be scarce and at a lower proportion than in Séítah rocks – which
1089 from the intensity of the 2.5 μ m absorption is probably very low.

1090 In Séítah, a significant amount of olivine of the protolith has been preserved, show-
1091 ing that aqueous alteration was likely limited in time, water/rock ratio and/or intensity
1092 (controlled by e.g., temperature, pH), as olivine alters rapidly at geological timescales
1093 when interacting with liquid water (Stopar et al., 2006). In Máaz, no olivine has been
1094 detected in the LIBS dataset, but we cannot exclude that it was fully dissolved and left
1095 voids in rocks (possibly allowing pore-space for deposition of sulfates). In both units, the
1096 presence of poorly crystalline mineral phases such as ferrihydrite points toward short-
1097 lived, low temperature water-rock interactions and/or limited diagenesis (Dehouck et al.,
1098 2017). This is in agreement with Wiens et al. (2022) analysis of LIBS data suggesting
1099 limited leaching of water-soluble cations in the rocks of the crater floor. In the follow-
1100 ing section, we discuss early- and late-stage (pre- and post-deposition of sulfates in pore-
1101 space, respectively) alteration products.

1102 *Early-stage alteration*

1103 The occurrence of clay-minerals in both Máaz and Séítah rocks is consistent with
1104 the weathering of an Fe/Mg-bearing protolith, likely unrelated to the sulfate deposition
1105 environment. Here, the Fe³⁺-clay mineral signature might be related to nontronite and/or

1106 hisingerite, which are spectrally similar. In this section, we discuss two hypotheses that
1107 could be compatible with the presence of these clay minerals and associated secondary
1108 minerals: supergene weathering or serpentinization.

1109 Ferric clay minerals such as nontronite usually form under neutral to alkaline and
1110 oxidizing conditions, directly from weathering of the initial protolith (Gainey et al., 2017),
1111 or by precipitation of ferrous clay minerals under anoxic/reducing conditions and their
1112 subsequent oxidation (Harder, 1976; Chemtob et al., 2017). Here, the coupled detection
1113 of oxyhydroxides, likely in the ferrihydrite form, and the absence of Fe^{2+} -clays point to-
1114 wards oxidizing conditions in the alteration history, but the associated timing is uncer-
1115 tain. Fe^{3+} -clays could have been produced during oxidizing and low-temperature weath-
1116 ering of the protolith near the surface (possibly related to the lake activity); another pos-
1117 sibility is that Fe^{2+} phyllosilicates first precipitated under anoxic conditions and were fully
1118 oxidized later in the history of the site.

1119 On the other hand, the presence of hisingerite can imply different alteration en-
1120 vironments. Though this mineral is relatively rare on Earth, it can be formed by super-
1121 gene weathering, but also during hydrothermal alteration of ferroan olivine-bearing rocks
1122 and has been proposed as a serpentinization product more common on Mars than on Earth
1123 owing to the higher Fe content of the Martian mantle (Evans et al., 2017; Tutolo et al.,
1124 2019). From orbit, Mg-serpentine has been detected in the regional olivine-bearing unit
1125 (Ehlmann et al., 2009). Brown et al. (2010) and VivianoBeck et al. (2013) proposed that
1126 the widespread carbonates observed in this unit could result from serpentinization and
1127 carbonation processes acting on ultramafic rocks, from which talc and magnesite would
1128 have formed with serpentinized olivine. In this contribution, we show the detection of
1129 Fe/Mg-carbonates and a Mg-OH phase in Séítah rocks. The nature of the Mg-OH min-
1130 eral is unclear, and could possibly be, among other candidates, talc or serpentine. In lab-
1131 oratory, Mg-serpentine-bearing mineral mixtures show a distinctive absorption band at
1132 $2.32 \mu\text{m}$, but even in mixtures with low serpentine concentrations the band depth of this
1133 feature is greater than what has been observed by the SuperCam instrument thus far
1134 in the mission (Mandon et al., 2022). This suggests no evidence for elevated Mg-serpentine
1135 content in the rocks measured during the first year of the mission. Hence, in the serpen-
1136 tinization scenario, either most of the Mg-serpentine produced from olivine alteration
1137 has been converted to hisingerite (Tutolo et al., 2019) or talc and magnesite under CO_2 -
1138 rich fluids and decreased temperature, or the rocks of Séítah never experienced condi-
1139 tions favorable to the production of Mg-serpentine from olivine. Nevertheless, Séítah rocks
1140 appear relatively pristine (with a limited amount of weathering products), as evidenced
1141 by large amount of remaining olivine.

1142 *Late-stage alteration*

1143 Geochemical models performed by Chevrier and Morisson (2021) showed that the
1144 evaporation of fluids resulting from the weathering of an olivine and pyroxene protolith
1145 and subsequent precipitation of ferric clay minerals and oxyhydroxides does not produce
1146 significant concentrations of Ca-sulfates and is not associated with Mg-sulfates precip-
1147 itation. The Mg-sulfates inferred from the infrared spectra of Máaz and Séítah rocks may
1148 record an environment distinct from the weathering of the crater floor and production
1149 of all the other secondary mineral phases mentioned before. The deposition of high-solubility
1150 phases such as sulfates would likely correspond to the final aqueous activity at Jezero,
1151 during the late-stage evaporation of the lake, with sulfate deposition from concentrated
1152 brines into the pores of the rocks. Their possible presence on both the abraded rocks of
1153 Máaz and Séítah supports that most of the crater floor observed today was exposed to
1154 the surface waters (likely briefly, in order to support the low alteration of the olivine grains),
1155 or at least not deeply buried to allow percolation of fluids into the bedrock. The pres-
1156 ence of akaganeite in Jezero is also consistent with past evaporitic conditions, likely in
1157 a highly saline and chlorinated environment.

1158 In Jezero, near-infrared spectral similarities were observed between dusty targets
1159 and the purple-tinted material coating portions of some rocks of the crater floor. This

1160 suggests some shared compositional traits and potentially a genetic link between dust
1161 and the coatings. This could result from induration of dust particles on the surface of
1162 rocks by a fluid of unknown composition, later in the history of the crater floor. LIBS
1163 measurements on these coatings show enrichment in S and H, in agreement with an hy-
1164 drated sulfate component similar to the dust (Meslin et al., this issue/Meslin et al., 2022).
1165 These coatings were observed sporadically on rocks from both formations of the crater
1166 floor (Garczynski et al., this issue/Garczynski et al., 2022), suggesting that at least mi-
1167 nor liquid water was present after the formation of the Máaz rocks. This environment
1168 could have been repeated over extended periods of time to allow cementation of grains
1169 into coatings, and balanced against erosion upon surface exposure. The fact that they
1170 are observed today on the surface of rocks affected by erosion implies that the last pro-
1171 cesses of coatings formation happened late in the history of Jezero. This late-stage in-
1172 teraction of water with the rock surfaces might explain the fact that salts were predom-
1173 inantly detected on abraded patches by both the VISIR and LIBS technique compared
1174 to the non abraded rock surfaces, as salt dissolution is likely to occur with limited sur-
1175 face water (although other processes such as irradiation can slightly alter sulfates on the
1176 surface; e.g., Cloutis et al., 2007).

1177 5.3 Origin of regolith materials

1178 Cousin et al. (2015) showed that the soils analyzed at Gale crater along the MSL
1179 rover traverse are composed of various material families, with the coarsest fraction be-
1180 ing likely sourced from physical weathering of the surrounding rocks, and the finest frac-
1181 tion being composed of different materials. These fine soils have a basaltic composition,
1182 thought to be global on the surface of Mars (Yen et al., 2005). Notably, the same trend
1183 seems to be present on the soils of Jezero crater:

- 1184 • the VISIR signature of the fine soils is consistent with the presence of pyroxene,
1185 with a weaker olivine component and consistent with a composition similar to the
1186 Martian global soils. The spectra measured on the fine soils at Jezero exhibit some
1187 weak absorptions near $2.3 \mu\text{m}$ and alternatively similar to those observed in rocks
1188 of the crater floor, suggesting some level of contamination of particles sourced from
1189 these rocks into the regolith;
- 1190 • the coarsest soils are associated with a strong olivine signature, similarly to the
1191 Séítah rocks and implying that, as for the coarse soils of Gale crater, physical weath-
1192 ering of the surrounding rocks source the local regolith.

1193 5.4 Comparison and implications for NIR orbital studies

1194 The evaluation of the reflectance between ~ 1 and $2.5 \mu\text{m}$ is predominantly used
1195 from orbit to detect and map minerals on the surface of Mars and hence significantly sup-
1196 ports the interpretation of past environments conditions (e.g., Bishop et al., 2008; Carter
1197 et al., 2013). The IRS onboard SuperCam was the first near-infrared reflectance spec-
1198 trometer to operate directly on the surface of Mars, joined three months later by the MarSCoDe
1199 instrument on the Zhurong rover as part of the Tianwen-1 mission (Liu et al., 2022). There-
1200 fore, it provides a prime opportunity to bring context to orbital studies using near-infrared
1201 data. Indeed, the spectra measured from orbit result from the combination of complex
1202 spectral mixing effect and variable surface state at large scales, as the best spatial res-
1203 olution of orbital hyperspectral cameras is on the order of $\sim 12 \text{ m/pixel}$ (Kreisch et al.,
1204 2017). It should be noted that the comparison between in situ and orbital measurements
1205 (the latter being usually shown as ratios in the literature) is not straightforward and
1206 future work with SuperCam data will expand on this aspect. Here, we provide an ini-
1207 tial report on the insights provided by the ground-based spectral signatures at Jezero
1208 crater, in order to understand the orbital ones.

1209

5.4.1 *Orbital datasets: bedrock exposures vs. soils signatures*

1210

1211

1212

1213

1214

1215

The in situ analysis of the crater floor by the rover payload and in particular by the VISIR spectrometer of SuperCam has confirmed the presence of all the minerals detected from orbit in the region (i.e., olivine, carbonates and Fe/Mg-phyllsilicates). These minerals are present in the bedrock (as opposed to the regolith), validating the strength and ability of the NIR orbital data to provide useful information to assess rock lithologies and hence deduce geological history.

1216

1217

1218

1219

1220

1221

1222

1223

1224

1225

1226

Perseverance's instruments analyses have revealed the presence of additional minerals that are theoretically detectable in the NIR. In particular, the rover payload has discovered the presence of sulfates (from LIBS, PIXL and SHERLOC instruments data, and in VISIR as shown here) and perchlorate on the crater floor (Razzell Hollis et al., 2022; Meslin et al., this issue/Meslin et al., 2022). These minerals were not detected from orbit in Jezero or on its watershed, despite their signature being observed elsewhere on Mars (e.g., Gendrin et al., 2005; Mass et al., 2010). As polyhydrated sulfates lack unique absorption bands in the NIR range, difficulty may arise in their identification and distinction from other hydrated minerals. Also, the signature of sulfates is relatively minor in our dataset, hence possibly having a weak contribution to the spectra acquired from orbit as well.

1227

1228

1229

1230

1231

1232

1233

1234

1235

1236

1237

1238

1239

1240

1241

1242

1243

1244

1245

1246

1247

1248

1249

1250

1251

A first-order comparison between the in situ reflectance signal of the crater floor units and spectra measured from orbit is provided in Fig. 13. From orbital data, it was first hypothesized that the Mááz formation (or the Cf-fr) was igneous in nature, based on its crater-retaining morphology and its near-infrared spectral signature consistent with a mixture of pyroxene and olivine (Goudge et al., 2015). Later, it was noted that a sedimentary origin could not be discarded based on the morphology solely (Stack et al., 2020); however, it was not understood whether the spectral signature of mafic minerals originates from the bedrock or from surficial deposits, despite the unit having a smooth texture on high-resolution orbital images that one could interpret as extensive soil coverage (Horgan et al., 2020). Investigation by the Mars 2020 payload has now confirmed the basaltic composition of the Mááz formation. However, no olivine has been observed, and we have shown here that the spectral signature of the bedrock in the near-infrared is dominated by hydrated minerals, with so far no single-point spectrum consistent with a mixture of olivine and pyroxene. On the other hand, NIR single-point spectra of soils exhibit the same features as the spectra measured by Goudge et al. (2015), with both olivine and pyroxene identified. This suggests that the mafic nature of the Mááz formation that was inferred from orbit could in fact be due to the major contribution of soils within CRISM pixels, that dominate the spectral signal in this extensively mantled area. In other words, the Mars 2020 mission confirmed the igneous composition of the Mááz formation that was inferred from orbit, but also revealed that the signature of mafic minerals detected with CRISM was more likely the signature of the regolith that extensively covers the Mááz bedrock. This highlights some implications for the interpretation of similar spectral signatures elsewhere on Mars, as fine soils tends to have an overall composition common to different locations on the planet (Cousin et al., this issue/Cousin et al., 2022).

1252

1253

1254

1255

1256

1257

1258

Wright et al. (2022) demonstrated that the surficial covers of Mááz and Séítah are significantly different, with the Mááz surface being mostly composed of scarce bedrock exposures and soils, and the Séítah surface of scarce bedrock exposures and large sand ripples. We showed that the sand dunes that are widely covering the Séítah formation seem to be composed of material sourced from the local bedrock. This might explain why the bedrock signature is dominating the orbital spectra measured over Séítah, as opposed to Mááz.

1259

1260

Using CRISM data, Horgan et al. (2020) noted an apparent enrichment of olivine along the rover traverse, compared to the rest of the Cf-fr. We showed that no rock of

1261 the Mááz formation exhibit an olivine signature in the VISIR, while parts of its regolith
 1262 consists of fine grains with mm-sized granules associated with a signature of olivine and
 1263 secondary minerals, similarly to Séítah rocks. Hence, a scenario where the erosion of the
 1264 nearby Séítah bedrock would provide material input onto the Cf-fr as eolian bedforms
 1265 is highly plausible, compared to an actual olivine enrichment of the Mááz bedrock near
 1266 the contact with Séítah (Vaughan et al., this issue/Vaughan et al., 2021, Cousin et al.,
 1267 this issue/Cousin et al., 2022).

1268 Finally, the rocks of the crater floor exhibit a stronger hydration band at $\sim 1.9 \mu$
 1269 m, compared to orbital measurements. This is consistent with the signature of rocks be-
 1270 ing diluted in the pixels of the orbital imaging spectrometers, which at best resolution
 1271 integrate tens of square meters of surface, where bedrock exposures are relatively scarce.
 1272 A similar effect was noted in the analysis of the NIR spectra measured by the Zhurong
 1273 rover (Liu et al., 2022), in an area which does not exhibit hydrated features from orbit.

1274 **5.4.2 Impact of the Martian dust**

1275 On Mars, one of the main limiting factors to identify minerals from hyperspectral
 1276 orbital data is the presence of aerial and surface dust, which impedes the spectral sig-
 1277 natures of the rocks on the surface. While the signature of dust in VISIR reflectance has
 1278 been estimated on dusty terrains (e.g., Le Moulic et al., 2006), data from the SuperCam
 1279 instrument offer the first opportunity to measure its near-infrared spectral signature in
 1280 situ. Surprisingly, even the dustiest targets exhibit a 1.9μ m absorption related to wa-
 1281 ter (caused by some hydrated mineral or water adsorbed on the surface of the small dust
 1282 particles), that does not seem to be related to the rocks underneath. This contrasts with
 1283 previous assumptions, based on orbital studies, that the dust is spectrally neutral in the
 1284 NIR below 2.5μ m, although the 3μ m fundamental absorption of water observed glob-
 1285 ally on the surface did suggest some form of hydration (Audouard et al., 2014). Simi-
 1286 lar to orbital measurements, a subtle downturn past 2.3μ m was observed, possibly re-
 1287 lated to the presence of some water-bearing materials. The effects of the atmosphere and
 1288 aerosols (decreasing spectral contrast) could explain these discrepancies between the or-
 1289 bital and in situ data. Also, we note that the in situ observations might be impacted by
 1290 multiple scattering leading to a 1.9μ m signature for dust.

1291 Notably, the magnetic dust deposited on the edges of the calibration targets does
 1292 exhibit a strong red slope in the visible, but a flat and featureless spectrum in the near-
 1293 infrared and no H_2O and OH related absorptions (section 4.1). One possibility is that
 1294 the magnetic dust (i.e., the fraction of dust attracted by the magnets, enclosing the SCCT),
 1295 does not include hydrated phases (but mainly maghemite/magnetite). Another expla-
 1296 nation is that the dust coatings present on the surrounding rocks are sufficiently older
 1297 to allow for hydration, perhaps as part of induration processes.

1298 **5.5 First near-infrared spectrometer on the surface: lessons learned af- 1299 ter one year of measurement**

1300 During the first year of the mission, the reflectance point spectrometer of Super-
 1301 Cam demonstrated considerable utility in inferring in a non destructive way the pres-
 1302 ence of a variety of primary and secondary minerals. Compensation for instrumental ef-
 1303 fects, variable illumination and observation conditions, and atmospheric corrections en-
 1304 abled constraints on surface mineralogy (albeit not always unique), even when mixtures
 1305 within the instrument fields of view complicated mineral identification.

1306 Mineralogical detections with VISIR are consistent with LIBS data (e.g., olivine,
 1307 pyroxene, Fe-oxides, carbonates, Mg-sulfates; Wiens et al., 2022; Clavé et al., this issue/Clav
 1308 et al., 2022; Meslin et al., this issue/Meslin et al., 2022), albeit with some differences.
 1309 In particular, minerals detections with one technique or the other are not necessarily as-

sociated with the same point in a raster, but often occur for the same target or rock type, likely owing to a significant difference of analytical footprint between VISIR and LIBS. Independent Component Analysis was proven quite relevant to separate individual spectral signatures from mineralogical endmembers when applied to IRS data. It allowed the identification of additional minerals, while the reflectance signal was dominated by the signature of hydrated phases: in particular, pyroxenes, which appear to be abundant based on data of the SuperCam's LIBS and the PIXL instrument (Wiens et al., 2022; Razzell Hollis et al., 2022), were not readily identified in the VISIR point spectra. Using the reflectance spectra, we were able to detect minerals not identified with LIBS data, such as the ferric phyllosilicates present in most of the rocks of the crater floor and which have implications for understanding the past aqueous environment at Jezero crater.

Ratios of SuperCam spectra were shown to be effective at emphasizing particular mineral phases present in the rocks, as was comparison of point spectra with mineral spectral libraries and band matching. However, ratioing was successful for mineralogical interpretation for only a limited set of observations, compared to orbital studies where it is conventionally performed (e.g., Horgan et al., 2020). To assist the retrieval of the different signatures of the minerals mixed in a rock spectrum, additional efforts are needed to document natural rock and mineral mixtures spectra (e.g., Bishop et al., 2013; Lantz et al., 2020; Mandon et al., 2022), as well as to understand the physics behind natural rock spectroscopy (e.g., Harloff & Arnold, 2001; Carli & Sgavetti, 2011; Carli et al., 2015). These will likely provide valuable insights to understand future data acquired by SuperCam or by other point spectrometers onboard planetary exploration missions (e.g., Korabiev et al., 2017; Xu et al., 2021; Liu et al., 2022). Ultimately, spectral unmixing (linear and unlinear) shall provide better constraints on the modal mineralogy and on the formation processes of the rocks and soils (Poulet et al., 2022).

6 Conclusion

In this work, we reported the first-year results of the first reflectance spectrometer on the Martian surface covering the visible and near-infrared range from 1.3 and 2.6 μ m, onboard the Perseverance rover of the Mars 2020 mission. In particular, we measured the reflectance spectra of rocks of the crater floor of Jezero crater, including the rocks that were cached for a possible return to Earth, as well as soils and dust coatings. From these results, we identified that:

- the basaltic upper part of Jezero's floor stratigraphy, informally referred to as the Máaz formation, exhibits a spectral signature in the VISIR dominated by hydrous mineral phases: Fe-oxyhydroxides (e.g., ferrihydrite, akaganeite), Fe³⁺-phyllosilicates (nontronite and/or hisingerite), monohydrated Mg-sulfates (e.g., kieserite), potential polyhydrated sulfates, and some minor Mg-OH phase(s) (e.g., Mg-smectite, serpentine, talc and/or brucite). Primary minerals were also detected by the spectrometer and consist of high-calcium pyroxenes (felspars being mostly featureless in the VISIR). No olivine was observed, in agreement with LIBS observations (Wiens et al., 2022, Udry et al., this issue/Udry et al., 2022);
- this mineralogical assemblage transitions into more mafic minerals towards the lowest stratigraphic levels observed, in the cumulate olivine-bearing formation called Séítah. Strong olivine signatures were observed in the reflectance data, along with high-Ca pyroxene and a complex mixture of alteration/hydrated mineral phases consisting of Fe-oxyhydroxides, Fe³⁺-phyllosilicates (nontronite and/or hisingerite), some Mg-OH phase(s) (e.g., Mg-smectite, serpentine, brucite and/or talc), scarce Fe/Mg-carbonates, an Al or Si-OH-phase, as well as monohydrated Mg-sulfates;
- alteration/hydrated minerals are present at relatively low proportion in the rocks (a few wt.% maximum) but their presence was evident in most of the rocks analyzed, pointing towards a widespread aqueous alteration on the crater floor but

1361 limited in intensity and/or time, as also evidenced by the dominance of poorly crys-
1362 talline mineral phases such as ferrihydrite and the lack of Al-phyllsilicates. The
1363 proposed alteration sequence of the Mááz formation includes weathering of the
1364 basaltic protolith from surface/near-surface leaching of the rocks possibly related
1365 to the lake activity or under deeper hydrothermal serpentinizing conditions, and
1366 under neutral to alkaline conditions. The presence of clay minerals usually favors
1367 the concentration and preservation of organic matter, though oxidizing conditions
1368 (as evidenced by the presence of and Fe³⁺-phyllsilicates and oxides) might have
1369 acted as a degradation process of organic materials. The strong olivine spectral
1370 features and weak secondary minerals signatures suggest that, as for the Mááz for-
1371 mation, water-rock interactions were likely minor in Séítah. Finally, evaporation
1372 of the lake likely induced minor sulfate deposition from concentrated brines onto
1373 pores of the rocks of the crater floor;

- 1374 • most of the minerals detected from orbit (olivine, pyroxene, Fe/Mg-phyllsilicates,
1375 Fe/Mg-carbonates, akaganeite; Goudge et al., 2015; Horgan et al., 2020; Carter
1376 et al., 2022) are present in the bedrock (as opposed to the regolith), validating the
1377 strength and ability of the NIR orbital data to provide useful information to as-
1378 sess rock lithologies and hence deduce geological history;
- 1379 • fine soils of the crater floor exhibit spectra suggesting a major mineralogical com-
1380 position consistent with what was inferred elsewhere on Mars, with pyroxene and
1381 possibly olivine, as well as a hydrous component, possibly inherited from the sur-
1382 rounding rocks. The regolith signature is likely what dominates orbital observa-
1383 tions of the Mááz formation, whose origin was thought to be igneous on the ba-
1384 sis of morphological and spectral criteria (Goudge et al., 2015). Similarities be-
1385 tween spectra measured on rocks and on coarse-grained soils suggest significant
1386 local input from the Séítah formation into the Mááz formation as eolian bedforms,
1387 and resolves the origin of the orbital signature of olivine-bearing materials on the
1388 western Mááz formation (Horgan et al., 2020);
- 1389 • the first in situ near-infrared spectra of Martian dust revealed similar features com-
1390 pared to dusty terrains measured from orbit, with a red slope in the visible range
1391 and an overall flat signature in the near-infrared range. However, a subtle hydra-
1392 tion band at 1.9 μ m is always present in the in situ spectra, which differs from
1393 orbital spectra and reveals a more significant contribution of hydration to the Mar-
1394 tian surface dust signature than previously thought. The spectral similarity be-
1395 tween dust and the purple-tinted coatings observed on the rocks of the crater floor
1396 suggests a similar composition between the two materials, and potential widespread
1397 past processes of dust induration under surface liquid water activity late in the
1398 history of Jezero;
- 1399 • of interest for the Mars Sample Return mission, all four pairs of rock sampled on
1400 the crater floor of Jezero during the first year of the Mars 2020 mission exhibit
1401 spectral features representative of the diversity of spectra measured on the two
1402 geological units investigated by the rover.

1403 Orbital data suggest that Perseverance landed in a relatively low hydration region,
1404 and that the rover will be driving through areas of progressively increasing hydration
1405 throughout the mission, as it moves onto the delta, the marginal carbonate unit and the
1406 region outside of Jezero crater. Sample return and future in situ measurements on these
1407 potentially more hydrated and/or diverse rocks are expected to bring new insights into
1408 the past environment at Jezero crater.

1409 Open research

1410 All data are available in the NASA Planetary Data System (Bell et al., 2020; Maki
1411 et al., 2021; Beegle et al., 2021; Maurice & Wiens, 2021).

1412 **Acknowledgments**

1413 The authors are truly grateful for the SuperCam and Mars 2020 hardware operations
 1414 teams for their investment in the mission. This work was supported by CNES. Additional
 1415 funding was provided by the following sources: NASA's Mars exploration program, CNRS,
 1416 IRIS OCAV, DIM ACAV, CSA, NSERC and ASI (ASI/INAF grant agreement n. 2017-
 1417 48-H-0).

1418 **Competing interests**

1419 The authors declare that they have no competing interests.

1420 **The SuperCam team**

1421 R. C. Wiens^{1,2}, S. Maurice³, T. Acosta-Maeda⁴, C. Alvarez-Llamas⁵, R. B. Ander-
 1422 son⁶, S. M. Angel⁷, D. M. Applin⁸, G. Arana⁹, M. Bassas-Portus¹⁰, R. Beal¹, P. Beck¹¹,
 1423 K. Benzerara¹², S. Bernard¹², P. Bernardi¹³, T. Bertrand¹³, O. Beyssac¹², T. Bosak¹⁴,
 1424 B. Bousquet¹⁵, A. Brown¹⁶, A. Cadu¹⁰, P. Caïs¹⁷, K. Castro⁹, B. Chide¹, E. Clavé¹⁵,
 1425 S. M. Clegg¹, E. Cloutis⁸, S. Connell⁸, A. Cousin³, A. Debus¹⁸, E. Dehouck¹⁹, D. Delapp¹,
 1426 C. Donny¹⁸, A. Dorresoundiram¹³, G. Dromart¹⁹, B. Dubois²⁰, C. Fabre²¹, A. Fau³, W.
 1427 Fischer²², O. Forni³, T. Fouchet¹³, R. Francis²³, J. Frydenvang²⁴, T. Gabriel⁶, O. Gasnault³,
 1428 E. Gibbons²⁵, I. Gontijo²³, X. Jacob²⁶, J. R. Johnson²⁷, H. Kalucha²², E. Kelly⁴, E. W.
 1429 Knutsen²⁸, G. Lacombe⁸, N. L. Lanza¹, J. Laserna⁵, J. Lasue³, S. Le Mouélic²⁹, C. Leg-
 1430 ett IV¹, R. Leveille²⁵, E. Lewin¹¹, G. Lopez-Reyes³⁰, R. D. Lorenz²⁷, E. Lorigny¹⁸, J.
 1431 M. Madariaga⁹, M. Madsen²⁴, S. Madsen²³, L. Mandon¹³, N. Mangold²⁹, M. Mann¹⁸,
 1432 J.-A. Manrique^{3,30}, J. Martinez-Frias³¹, L. E. Mayhew³², T. McConnochie³³, S. M. McLen-
 1433 nan³⁴, N. Melikechi³⁵, P.-Y. Meslin³, F. Meunier¹⁸, D. Mimoun¹⁰, G. Montagnac¹⁹, F.
 1434 Montmessin⁸, J. Moros⁵, V. Mousset¹⁸, N. Murdoch¹⁰, T. Nelson¹, R. T. Newell¹, A. Ollila¹,
 1435 Y. Parot³, P. Pilleri³, C. Pilorget^{36,37}, P. Pinet³, G. Pont¹⁸, F. Poulet³⁶, C. Quantin-
 1436 Nataf¹⁹, B. Quertier¹⁷, W. Rapin³, A. Reyes-Newell¹, S. Robinson¹, L. Rochas¹⁸, C. Royer¹³,
 1437 F. Rull³⁰, V. Sautter¹², S. Schröder³⁸, S. Sharma⁴, V. Shridar²³, A. Sournac¹⁰, A. Stott¹⁰,
 1438 M. Toplis³, I. Torre-Fdez⁹, N. Turenne⁸, T. Tzanetos²³, A. Udry³⁹, M. Veneranda³⁰, D.
 1439 Venhaus¹, D. Vogt³⁸ and P. Willis²³

1440 ¹Space and Planetary Exploration Team, Los Alamos National Laboratory, Los Alamos,
 1441 New Mexico, USA. ²Earth, Atmospheric, and Planetary Sciences, Purdue University, West
 1442 Lafayette, Indiana, USA. ³Institut de Recherche en Astrophysique et Planétologie, Uni-
 1443 versité de Toulouse 3 Paul Sabatier, CNRS, CNES, Toulouse, France. ⁴University of Hawaii,
 1444 Manoa, Hawaii, USA. ⁵Universidad de Malaga, Malaga, Spain. ⁶U.S. Geological Survey,
 1445 Flagstaff, Arizona, USA. ⁷Department of Chemistry and Biochemistry, University of South
 1446 Carolina, Columbia, South Carolina, USA. ⁸University of Winnipeg, Winnipeg, Canada.
 1447 ⁹University of Basque Country, UPV/EHU, Leioa, Bilbao, Spain. ¹⁰Institut Supérieur
 1448 de l'Aéronautique et de l'Espace (ISAE-SUPAERO), Université de Toulouse, Toulouse,
 1449 France. ¹¹Institut de Planétologie et Astrophysique de Grenoble, CNRS, Univ. Greno-
 1450 ble Alpes, Grenoble, France. ¹²Institut de Minéralogie, de Physique des Matériaux et
 1451 de Cosmochimie, CNRS, Sorbonne Université, MNHN, Paris, France. ¹³Laboratoire d'Etudes
 1452 Spatiales et d'Instrumentation en Astrophysique, Obs. Paris, CNRS, Sorbonne Univ.,
 1453 Univ. Paris-Diderot, Meudon, France. ¹⁴Earth, Atmospheric and Planetary Sciences, Mas-
 1454 sachusetts Institute of Technology, Cambridge, Massachusetts, USA. ¹⁵Centre Lasers In-
 1455 tenses et Applications, CNRS, CEA, Univ. Bordeaux, Bordeaux, France. ¹⁶Plancius Re-
 1456 search, Severna Park, Maryland, USA. ¹⁷Laboratoire d'Astrophysique de Bordeaux, CNRS,
 1457 Univ. Bordeaux, Bordeaux, France. ¹⁸Centre National d'Etudes Spatiales, Toulouse, France.
 1458 ¹⁹Univ. Lyon, UCBL, ENSL, UJM, CNRS, LGL-TPE, Villeurbanne, France. ²⁰Groupe
 1459 d'Instrumentation Scientifique, Observatoire Midi-Pyrénées, Toulouse, France. ²¹GéoRessources,
 1460 CNRS, Univ. Lorraine, Nancy, France. ²²California Institute of Technology, Pasadena,
 1461 California, USA. ²³Jet Propulsion Laboratory, California Institute of Technology, Pasadena,

1462 California, USA. ²⁴University of Copenhagen, Copenhagen, Denmark. ²⁵McGill Univer-
 1463 sity, Montreal, Canada. ²⁶Institut de Mécanique des Fluides, Univ. Toulouse 3 Paul Sabatier,
 1464 INP, CNRS, Toulouse, France. ²⁷Space Exploration Sector, Johns Hopkins Applied Physics
 1465 Laboratory, Laurel, Maryland, USA. ⁸Laboratoire Atmosphères, Milieux, Observations
 1466 Spatiales, CNRS, Univ. Saint-Quentin-en-Yvelines, Sorbonne Univ., Guyancourt, France.
 1467 ²⁹Laboratoire Planétologie et Géosciences, CNRS, Université Nantes, Université Angers,
 1468 Nantes, France. ³⁰University of Valladolid, Valladolid, Spain. ³¹Agencia Estatal Con-
 1469 sejo Superior de Investigaciones Científicas, Madrid, Spain. ³²Department of Geologi-
 1470 cal Sciences, University of Colorado Boulder, Boulder, Colorado, USA. ³³University of
 1471 Maryland, College Park, Maryland, USA. ³⁴State University of New York, Stony Brook,
 1472 New York, USA. ³⁵Department of Physics and Applied Physics, Kennedy College of Sci-
 1473 ences, University of Massachusetts, Massachusetts, USA. ³⁶Institut d’Astrophysique Spa-
 1474 tiale, CNRS, Univ. Paris-Saclay, Orsay, France. ³⁷Institut Universitaire de France, Paris,
 1475 France. ³⁸Deutsches Zentrum für Luft- und Raumfahrt (DLR), Institute of Optical Sen-
 1476 sor Systems, Berlin, Germany. ³⁹University of Nevada Las Vegas, Las Vegas, Nevada,
 1477 USA.

1478 References

- 1479 Audouard, J., Poulet, F., Vincendon, M., Milliken, R. E., Jouglet, D., Bib-
 1480 ring, J.-P., ... Langevin, Y. (2014). Water in the Martian re-
 1481 golith from OMEGA/Mars Express. *Journal of Geophysical Research:*
 1482 *Planets*, 119(8), 1969–1989. Retrieved 2022-05-09, from [https://](https://onlinelibrary.wiley.com/doi/abs/10.1002/2014JE004649)
 1483 onlinelibrary.wiley.com/doi/abs/10.1002/2014JE004649 (eprint:
 1484 <https://onlinelibrary.wiley.com/doi/pdf/10.1002/2014JE004649>) doi:
 1485 10.1002/2014JE004649
- 1486 Beegle, L. (2021). *Mars 2020 SHERLOC Bundle*. (Publisher: NASA Planetary Data
 1487 System. doi:10.17189/1522643)
- 1488 Bell, J., Maki, J. N., Mehall, G. L., Ravine, M. A., Caplinger, M. A., Bailey, Z. J.,
 1489 ... Wolff, M. J. (2021, February). The Mars 2020 Perseverance Rover Mast
 1490 Camera Zoom (Mastcam-Z) Multispectral, Stereoscopic Imaging Investigation.
 1491 *Space Science Reviews*, 217(1), 24. Retrieved 2022-04-17, from [https://](https://doi.org/10.1007/s11214-020-00755-x)
 1492 doi.org/10.1007/s11214-020-00755-x doi: 10.1007/s11214-020-00755-x
- 1493 Bell, J. F., & Maki, J. N. (2020). *Mars 2020 Mast Camera Zoom Bundle, from*
 1494 *Arizona State University Mastcam-Z Instrument Team, calibrated prod-*
 1495 *ucts*. Retrieved 2022-08-17, from [https://pds.nasa.gov/ds-view/pds/](https://pds.nasa.gov/ds-view/pds/viewBundle.jsp?identifier=urn%3Anasa%3Aaps%3Amars2020_mastcamz_sci_calibrated&version=1.0)
 1496 [viewBundle.jsp?identifier=urn%3Anasa%3Aaps%3Amars2020_mastcamz_sci](https://pds.nasa.gov/ds-view/pds/viewBundle.jsp?identifier=urn%3Anasa%3Aaps%3Amars2020_mastcamz_sci_calibrated&version=1.0)
 1497 [_calibrated&version=1.0](https://pds.nasa.gov/ds-view/pds/viewBundle.jsp?identifier=urn%3Anasa%3Aaps%3Amars2020_mastcamz_sci_calibrated&version=1.0) (Publisher: NASA Planetary Data System. doi:
 1498 10.17189/Q3TS-C749)
- 1499 Bell, J. F. I., Glotch, T. D., Hamilton, V. E., McConnochie, T., McCord, T.,
 1500 McEwen, A., ... Arvidson, R. E. (2008). Visible to near-IR multispectral
 1501 orbital observations of Mars. *The Martian Surface-Composition, Mineralogy,*
 1502 *and Physical Properties*, 169.
- 1503 Beyssac, O., Gasnault, O., Chide, B., Clave, E., Cousin, A., Forni, O., ... Wiens,
 1504 R. (2021, December). Mafic Chemistry and Mineralogy (including
 1505 olivine) of the Coarse-Grained Regolith Analyzed by SuperCam at Jezero
 1506 Crater, Mars. In (Vol. 2021, pp. P25A–08). Retrieved 2022-08-18, from
 1507 <https://ui.adsabs.harvard.edu/abs/2021AGUFM.P25A..08B> (Conference
 1508 Name: AGU Fall Meeting Abstracts ADS Bibcode: 2021AGUFM.P25A..08B)
- 1509 Bhartia, R., Beegle, L. W., DeFlores, L., Abbey, W., Razzell Hollis, J., Uck-
 1510 ert, K., ... Zan, J. (2021, May). Perseverance Scanning Habitable En-
 1511 vironments with Raman and Luminescence for Organics and Chemicals
 1512 (SHERLOC) Investigation. *Space Science Reviews*, 217(4), 58. Retrieved
 1513 2022-04-17, from <https://doi.org/10.1007/s11214-021-00812-z> doi:
 1514 10.1007/s11214-021-00812-z

- 1515 Bishop, J. L. (2020). *Visible and Near-Infrared Reflectance Spectroscopy Laboratory*
 1516 *Spectra of Geologic Materials. in REMOTE COMPOSITIONAL ANALYSIS-*
 1517 *Techniques for Understanding Spectroscopy, Mineralogy, and Geochemistry of*
 1518 *Planetary Surfaces*(Edited by Janice L. Bishop, James F. Bell, III, Jeffrey E.
 1519 *Moersch*). Cambridge University Press.
- 1520 Bishop, J. L., Dobrea, E. Z. N., McKeown, N. K., Parente, M., Ehlmann, B. L.,
 1521 Michalski, J. R., ... Mustard, J. F. (2008). Phyllosilicate diversity and past
 1522 aqueous activity revealed at Mawrth Vallis, Mars. *Science*, *321*(5890), 830–
 1523 833. doi: 10.1126/science.1159699
- 1524 Bishop, J. L., Perry, K. A., Dyar, M. D., Bristow, T. F., Blake, D. F., Brown, A. J.,
 1525 & Peel, S. E. (2013). Coordinated spectral and XRD analyses of magnesite-
 1526 nontronite-forsterite mixtures and implications for carbonates on Mars. *Jour-*
 1527 *nal of Geophysical Research: Planets*, *118*(4), 635–650. Retrieved 2019-12-
 1528 19, from [http://agupubs.onlinelibrary.wiley.com/doi/abs/10.1002/](http://agupubs.onlinelibrary.wiley.com/doi/abs/10.1002/jgre.20066)
 1529 [jgre.20066](http://agupubs.onlinelibrary.wiley.com/doi/abs/10.1002/jgre.20066) doi: 10.1002/jgre.20066
- 1530 Bishop, J. L., Quinn, R., & Dyar, M. D. (2014, August). Spectral and thermal prop-
 1531 erties of perchlorate salts and implications for Mars. *The American mineralo-*
 1532 *gist*, *99*(8-9), 1580–1592. Retrieved 2022-04-11, from [https://www.ncbi.nlm](https://www.ncbi.nlm.nih.gov/pmc/articles/PMC7008933/)
 1533 [.nih.gov/pmc/articles/PMC7008933/](https://www.ncbi.nlm.nih.gov/pmc/articles/PMC7008933/) doi: 10.2138/am.2014.4707
- 1534 Bramble, M. S., Mustard, J. F., & Salvatore, M. R. (2017, September). The geolog-
 1535 ical history of Northeast Syrtis Major, Mars. *Icarus*, *293*, 66–93. Retrieved
 1536 2018-03-14, from [http://www.sciencedirect.com/science/article/pii/](http://www.sciencedirect.com/science/article/pii/S0019103516303499)
 1537 [S0019103516303499](http://www.sciencedirect.com/science/article/pii/S0019103516303499) doi: 10.1016/j.icarus.2017.03.030
- 1538 Brown, A. J., Hook, S. J., Baldridge, A. M., Crowley, J. K., Bridges, N. T., Thom-
 1539 son, B. J., ... Bishop, J. L. (2010, August). Hydrothermal formation of
 1540 Clay-Carbonate alteration assemblages in the Nili Fossae region of Mars. *Earth*
 1541 *and Planetary Science Letters*, *297*(1), 174–182. Retrieved 2019-01-05, from
 1542 <http://www.sciencedirect.com/science/article/pii/S0012821X10003924>
 1543 doi: 10.1016/j.epsl.2010.06.018
- 1544 Brown, A. J., Kah, L., Mandon, L., Wiens, R., Pinet, P., Clav, E., ... Rava-
 1545 nis, E. (2022, June). *Properties of the Nili Fossae Olivine-clay-carbonate*
 1546 *lithology: orbital and in situ at Seitah*. arXiv. Retrieved 2022-08-18,
 1547 from <http://arxiv.org/abs/2206.13380> (arXiv:2206.13380 [astro-ph,
 1548 physics:physics]) doi: 10.48550/arXiv.2206.13380
- 1549 Brown, A. J., Viviano, C. E., & Goudge, T. A. (2020). Olivine-Carbonate Min-
 1550 eralogy of the Jezero Crater Region. *Journal of Geophysical Research:*
 1551 *Planets*, *125*(3), e2019JE006011. Retrieved 2020-03-19, from [http://](http://agupubs.onlinelibrary.wiley.com/doi/abs/10.1029/2019JE006011)
 1552 agupubs.onlinelibrary.wiley.com/doi/abs/10.1029/2019JE006011 doi:
 1553 10.1029/2019JE006011
- 1554 Burns, R. G. (1993). *Mineralogical Applications of Crystal Field Theory*. Cambridge
 1555 University Press.
- 1556 Calvin, W. M., King, T. V. V., & Clark, R. N. (1994). Hydrous carbon-
 1557 ates on Mars?: Evidence from Mariner 6/7 infrared spectrometer and
 1558 ground-based telescopic spectra. *Journal of Geophysical Research:*
 1559 *Planets*, *99*(E7), 14659–14675. Retrieved 2022-08-19, from [https://](https://onlinelibrary.wiley.com/doi/abs/10.1029/94JE01090)
 1560 onlinelibrary.wiley.com/doi/abs/10.1029/94JE01090 (_eprint:
 1561 <https://onlinelibrary.wiley.com/doi/pdf/10.1029/94JE01090>) doi: 10.1029/
 1562 94JE01090
- 1563 Cardoso, J. F., & Souloumiac, A. (1993, December). Blind beamforming for non-
 1564 gaussian signals. *IEE Proceedings F (Radar and Signal Processing)*, *140*(6),
 1565 362–370. Retrieved 2021-10-20, from [https://digital-library.theiet.org/](https://digital-library.theiet.org/content/journals/10.1049/ip-f-2.1993.0054)
 1566 [content/journals/10.1049/ip-f-2.1993.0054](https://digital-library.theiet.org/content/journals/10.1049/ip-f-2.1993.0054) (Publisher: IET Digital
 1567 Library) doi: 10.1049/ip-f-2.1993.0054
- 1568 Carli, C., Serventi, G., & Sgavetti, M. (2015, January). VNIR spectral character-
 1569 istics of terrestrial igneous effusive rocks: mineralogical composition and the

- 1570 influence of texture. *Geological Society, London, Special Publications*, 401(1),
 1571 139–158. Retrieved 2020-08-22, from [https://sp.lyellcollection.org/
 1572 content/401/1/139](https://sp.lyellcollection.org/content/401/1/139) doi: 10.1144/SP401.19
- 1573 Carli, C., & Sgavetti, M. (2011, February). Spectral characteristics of rocks: Effects
 1574 of composition and texture and implications for the interpretation of planet
 1575 surface compositions. *Icarus*, 211(2), 1034–1048. Retrieved 2020-08-24, from
 1576 <http://www.sciencedirect.com/science/article/pii/S0019103510004276>
 1577 doi: 10.1016/j.icarus.2010.11.008
- 1578 Carter, J., Loizeau, D., Mangold, N., Poulet, F., & Bibring, J.-P. (2015, March).
 1579 Widespread surface weathering on early Mars: A case for a warmer and wet-
 1580 ter climate. *Icarus*, 248, 373–382. Retrieved 2022-08-27, from [https://
 1581 www.sciencedirect.com/science/article/pii/S0019103514006393](https://www.sciencedirect.com/science/article/pii/S0019103514006393) doi:
 1582 10.1016/j.icarus.2014.11.011
- 1583 Carter, J., & Poulet, F. (2013, December). Ancient plutonic processes on Mars in-
 1584 ferred from the detection of possible anorthositic terrains. *Nature Geoscience*,
 1585 6(12), 1008–1012. Retrieved 2020-07-03, from [http://www.nature.com/
 1586 articles/ngeo1995](http://www.nature.com/articles/ngeo1995) doi: 10.1038/ngeo1995
- 1587 Carter, J., Poulet, F., Bibring, J.-P., Mangold, N., & Murchie, S. (2013). Hydrous
 1588 minerals on Mars as seen by the CRISM and OMEGA imaging spectrome-
 1589 ters: Updated global view. *Journal of Geophysical Research: Planets*, 118(4),
 1590 831–858. doi: 10.1029/2012JE004145
- 1591 Carter, J., Riu, L., Poulet, F., Bibring, J.-P., Langevin, Y., & Gondet, B. (2022,
 1592 August). A Mars Orbital Catalog of Aqueous Alteration Signatures
 1593 (MOCAAS). *Icarus*, 115164. Retrieved 2022-08-23, from [https://
 1594 www.sciencedirect.com/science/article/pii/S0019103522002664](https://www.sciencedirect.com/science/article/pii/S0019103522002664) doi:
 1595 10.1016/j.icarus.2022.115164
- 1596 Carter, J., Viviano-Beck, C., Loizeau, D., Bishop, J., & Le Deit, L. (2015, June).
 1597 Orbital detection and implications of akaganite on Mars. *Icarus*, 253, 296–
 1598 310. Retrieved 2022-08-19, from [https://www.sciencedirect.com/science/
 1599 article/pii/S0019103515000366](https://www.sciencedirect.com/science/article/pii/S0019103515000366) doi: 10.1016/j.icarus.2015.01.020
- 1600 Chemtob, S. M., Nickerson, R. D., Morris, R. V., Agresti, D. G., & Catalano,
 1601 J. G. (2017). Oxidative Alteration of Ferrous Smectites and Impli-
 1602 cations for the Redox Evolution of Early Mars. *Journal of Geophysi-
 1603 cal Research: Planets*, 122(12), 2469–2488. Retrieved 2022-03-04, from
 1604 <https://onlinelibrary.wiley.com/doi/abs/10.1002/2017JE005331>
 1605 (_eprint: <https://onlinelibrary.wiley.com/doi/pdf/10.1002/2017JE005331>)
 1606 doi: 10.1002/2017JE005331
- 1607 Chevrier, V. F., & Morisson, M. (2021). Carbonate-Phyllosilicate Parageneses and
 1608 Environments of Aqueous Alteration in Nili Fossae and Mars. *Journal of Geo-
 1609 physical Research: Planets*, 126(4), e2020JE006698. Retrieved 2022-02-18,
 1610 from <https://onlinelibrary.wiley.com/doi/abs/10.1029/2020JE006698>
 1611 (_eprint: <https://onlinelibrary.wiley.com/doi/pdf/10.1029/2020JE006698>) doi:
 1612 10.1029/2020JE006698
- 1613 Clark, R. N., & Roush, T. L. (1984, July). Reflectance spectroscopy: Quantitative
 1614 analysis techniques for remote sensing applications. *Journal of Geophysical Re-
 1615 search: Solid Earth*, 89(B7), 6329–6340. Retrieved 2018-03-14, from [http://
 1616 onlinelibrary.wiley.com/doi/10.1029/JB089iB07p06329/abstract](http://onlinelibrary.wiley.com/doi/10.1029/JB089iB07p06329/abstract) doi:
 1617 10.1029/JB089iB07p06329
- 1618 Clav, E., Benzerara, K., Beck, P., Meslin, P. Y., Beyssac, O., Forni, O., ... Su-
 1619 perCam Team (2022, March). Carbonate Detection with SuperCam in the
 1620 Jezero Crater, Mars. In (Vol. 2678, p. 2001). Retrieved 2022-08-18, from
 1621 <https://ui.adsabs.harvard.edu/abs/2022LPICo2678.2001C> (Conference
 1622 Name: LPI Contributions ADS Bibcode: 2022LPICo2678.2001C)
- 1623 Cloutis, E. A., Craig, M. A., Mustard, J. F., Kruzelecky, R. V., Jamroz, W. R.,
 1624 Scott, A., ... King, P. L. (2007). Stability of hydrated minerals on

- 1625 Mars. *Geophysical Research Letters*, 34(20). Retrieved 2022-06-26, from
 1626 <https://onlinelibrary.wiley.com/doi/abs/10.1029/2007GL031267>
 1627 (_eprint: <https://onlinelibrary.wiley.com/doi/pdf/10.1029/2007GL031267>)
 1628 doi: 10.1029/2007GL031267
- 1629 Cloutis, E. A., & Gaffey, M. J. (1991, April). Spectral-compositional variations in
 1630 the constituent minerals of mafic and ultramafic assemblages and remote sens-
 1631 ing implications. *Earth, Moon, and Planets*, 53(1), 11–53. Retrieved 2022-03-
 1632 23, from <https://doi.org/10.1007/BF00116217> doi: 10.1007/BF00116217
- 1633 Clnet, H., Pinet, P., Daydou, Y., Heuripeau, F., Rosemberg, C., Baratoux, D., &
 1634 Chevrel, S. (2011, May). A new systematic approach using the Modified
 1635 Gaussian Model: Insight for the characterization of chemical composition of
 1636 olivines, pyroxenes and olivinepyroxene mixtures. *Icarus*, 213(1), 404–422. Re-
 1637 trieved 2018-03-14, from [http://www.sciencedirect.com/science/article/
 1638 pii/S0019103511000868](http://www.sciencedirect.com/science/article/pii/S0019103511000868) doi: 10.1016/j.icarus.2011.03.002
- 1639 Cousin, A., Meslin, P. Y., Hausrath, E. M., Cardarelli, E., Lasue, J., Forni, O., ...
 1640 Maurice, S. (2022, March). Soil Diversity at Mars: Comparison of Dataset
 1641 from Gale and Jezero Craters. In (Vol. 2678, p. 1374). Retrieved 2022-05-17,
 1642 from <https://ui.adsabs.harvard.edu/abs/2022LPICo2678.1374C> (ADS
 1643 Bibcode: 2022LPICo2678.1374C)
- 1644 Cousin, A., Meslin, P. Y., Wiens, R. C., Rapin, W., Mangold, N., Fabre, C., ...
 1645 Delapp, D. (2015, March). Compositions of coarse and fine particles in mar-
 1646 tian soils at gale: A window into the production of soils. *Icarus*, 249, 22–42.
 1647 Retrieved 2022-05-06, from [https://www.sciencedirect.com/science/
 1648 article/pii/S0019103514002449](https://www.sciencedirect.com/science/article/pii/S0019103514002449) doi: 10.1016/j.icarus.2014.04.052
- 1649 Cousin, A., Sautter, V., Fabre, C., Dromart, G., Montagnac, G., Drouet, C., ...
 1650 Wiens, R. C. (2022, February). SuperCam calibration targets on board
 1651 the perseverance rover: Fabrication and quantitative characterization. *Spec-
 1652 trochimica Acta Part B: Atomic Spectroscopy*, 188, 106341. Retrieved 2022-
 1653 04-11, from [https://www.sciencedirect.com/science/article/pii/
 1654 S0584854721002986](https://www.sciencedirect.com/science/article/pii/S0584854721002986) doi: 10.1016/j.sab.2021.106341
- 1655 Crowley, J. K. (1986). Visible and near-infrared spectra of carbonate
 1656 rocks: Reflectance variations related to petrographic texture and im-
 1657 purities. *Journal of Geophysical Research: Solid Earth*, 91(B5),
 1658 5001–5012. Retrieved 2022-08-27, from [https://onlinelibrary
 1659 .wiley.com/doi/abs/10.1029/JB091iB05p05001](https://onlinelibrary.wiley.com/doi/abs/10.1029/JB091iB05p05001) (_eprint:
 1660 <https://onlinelibrary.wiley.com/doi/pdf/10.1029/JB091iB05p05001>) doi:
 1661 10.1029/JB091iB05p05001
- 1662 Dehouck, E., McLennan, S. M., Sklute, E. C., & Dyar, M. D. (2017). Sta-
 1663 bility and fate of ferrihydrite during episodes of water/rock interactions
 1664 on early Mars: An experimental approach. *Journal of Geophysical Re-
 1665 search: Planets*, 122(2), 358–382. Retrieved 2022-03-04, from [https://
 1666 onlinelibrary.wiley.com/doi/abs/10.1002/2016JE005222](https://onlinelibrary.wiley.com/doi/abs/10.1002/2016JE005222) (_eprint:
 1667 <https://onlinelibrary.wiley.com/doi/pdf/10.1002/2016JE005222>) doi:
 1668 10.1002/2016JE005222
- 1669 Edgett, K. S. (2018, November). A two-decade journey, learning to recognize
 1670 that Mars has a vast and accessible sedimentary rock record. GSA. Re-
 1671 trieved 2021-10-12, from [https://gsa.confex.com/gsa/2018AM/webprogram/
 1672 Paper316799.html](https://gsa.confex.com/gsa/2018AM/webprogram/Paper316799.html)
- 1673 Ehlmann, B. L., Mustard, J. F., Murchie, S. L., Poulet, F., Bishop, J. L., Brown,
 1674 A. J., ... Wray, J. J. (2008, December). Orbital Identification of Carbonate-
 1675 Bearing Rocks on Mars. *Science*, 322(5909), 1828–1832. Retrieved 2018-03-14,
 1676 from <http://science.sciencemag.org/content/322/5909/1828> doi:
 1677 10.1126/science.1164759
- 1678 Ehlmann, B. L., Mustard, J. F., Swayze, G. A., Clark, R. N., Bishop, J. L.,
 1679 Poulet, F., ... Murchie, S. L. (2009, February). Identification of hy-

- 1680 drated silicate minerals on Mars using MRO-CRISM: Geologic context
 1681 near Nili Fossae and implications for aqueous alteration. *Journal of Geo-*
 1682 *physical Research: Planets*, 114(E2), E00D08. Retrieved 2018-03-14, from
 1683 <http://onlinelibrary.wiley.com/doi/10.1029/2009JE003339/abstract>
 1684 doi: 10.1029/2009JE003339
- 1685 Evans, B. W., Kuehner, S. M., Joswiak, D. J., & Cressey, G. (2017, March). Ser-
 1686 pentine, Iron-rich Phyllosilicates and Fayalite Produced by Hydration and Mg
 1687 Depletion of Peridotite, Duluth Complex, Minnesota, USA. *Journal of Petrol-*
 1688 *ogy*, 58(3), 495–512. Retrieved 2022-05-06, from <https://doi.org/10.1093/petrology/egx024> doi: 10.1093/petrology/egx024
- 1689 Farley, K. A., Stack, K. M., Shuster, D. L., Horgan, B. H. N., Hurowitz, J. A., Tar-
 1690 nas, J. D., ... Zorzano, M.-P. (2022, August). Aqueously altered igneous rocks
 1691 sampled on the floor of Jezero crater, Mars. *Science*, eabo2196. Retrieved
 1692 2022-08-27, from <https://www.science.org/doi/10.1126/science.abo2196>
 1693 (Publisher: American Association for the Advancement of Science) doi:
 1694 10.1126/science.abo2196
- 1695 Farley, K. A., Williford, K. H., Stack, K. M., Bhartia, R., Chen, A., dela Torre, M.,
 1696 ... Wiens, R. C. (2020, December). Mars 2020 Mission Overview. *Space*
 1697 *Science Reviews*, 216(8), 142. Retrieved 2021-02-05, from [https://doi.org/](https://doi.org/10.1007/s11214-020-00762-y)
 1698 [10.1007/s11214-020-00762-y](https://doi.org/10.1007/s11214-020-00762-y) doi: 10.1007/s11214-020-00762-y
- 1699 Fassett, C. I., & Head, J. W. (2005). Fluvial sedimentary deposits on Mars: Ancient
 1700 deltas in a crater lake in the Nili Fossae region. *Geophysical Research Letters*,
 1701 32(14). Retrieved 2020-05-29, from [http://agupubs.onlinelibrary.wiley](http://agupubs.onlinelibrary.wiley.com/doi/abs/10.1029/2005GL023456)
 1702 [.com/doi/abs/10.1029/2005GL023456](http://agupubs.onlinelibrary.wiley.com/doi/abs/10.1029/2005GL023456) doi: 10.1029/2005GL023456
- 1703 Fau, A., Beyssac, O., Gauthier, M., Meslin, P. Y., Cousin, A., Benzerara, K., ...
 1704 Maurice, S. (2019, October). Pulsed laser-induced heating of mineral phases:
 1705 Implications for laser-induced breakdown spectroscopy combined with Raman
 1706 spectroscopy. *Spectrochimica Acta Part B: Atomic Spectroscopy*, 160, 105687.
 1707 Retrieved 2022-05-23, from [https://www.sciencedirect.com/science/](https://www.sciencedirect.com/science/article/pii/S0584854719301600)
 1708 [article/pii/S0584854719301600](https://www.sciencedirect.com/science/article/pii/S0584854719301600) doi: 10.1016/j.sab.2019.105687
- 1709 Ferguson, R. L., Hare, T. M., Mayer, D. P., Galuszka, D. M., Redding, B. L., Smith,
 1710 E. D., ... Otero, R. E. (2020, March). Mars 2020 Terrain Relative Navigation
 1711 Flight Product Generation: Digital Terrain Model and Orthorectified Image
 1712 Mosaic. , 2020. Retrieved 2022-04-13, from [https://ui.adsabs.harvard.edu/](https://ui.adsabs.harvard.edu/abs/2020LPI...51.2020F)
 1713 [abs/2020LPI...51.2020F](https://ui.adsabs.harvard.edu/abs/2020LPI...51.2020F) (Conference Name: 51st Annual Lunar and Plan-
 1714 etary Science Conference ADS Bibcode: 2020LPI...51.2020F)
- 1715 Fouchet, T., Reess, J.-M., Montmessin, F., Hassen-Khodja, R., Nguyen-Tuong, N.,
 1716 Humeau, O., ... Wiens, R. C. (2022). The SuperCam infrared spectrome-
 1717 ter for the perseverance rover of the Mars2020 mission. *Icarus*, 373, 114773.
 1718 Retrieved 2021-11-13, from [https://www.sciencedirect.com/science/](https://www.sciencedirect.com/science/article/pii/S0019103521004231)
 1719 [article/pii/S0019103521004231](https://www.sciencedirect.com/science/article/pii/S0019103521004231) doi: 10.1016/j.icarus.2021.114773
- 1720 Gainey, S. R., Hausrath, E. M., Adcock, C. T., Tschauner, O., Hurowitz, J. A.,
 1721 Ehlmann, B. L., ... Bartlett, C. L. (2017, November). Clay mineral formation
 1722 under oxidized conditions and implications for paleoenvironments and organic
 1723 preservation on Mars. *Nature Communications*, 8(1), 1230. Retrieved 2022-02-
 1724 18, from <https://www.nature.com/articles/s41467-017-01235-7> (Num-
 1725 ber: 1 Publisher: Nature Publishing Group) doi: 10.1038/s41467-017-01235-7
- 1726 Garczynski, B. J., III, J. B., Horgan, B. H. N., Johnson, J. R., Rice, M. S., Vaughan,
 1727 A., ... Herd, C. D. K. (2022). Perseverance and the purple coating: a
 1728 Mastcam-Z multispectral story. In *LPI Contributions* (Vol. 2678, p. 2346).
- 1729 Gasnault, O., Virmontois, C., Maurice, S., Wiens, R., Le Moulic, S., Bernardi, P.,
 1730 ... Rapin, W. (2021). What SuperCam will see: The Remote Micro-Imager
 1731 aboard Perseverance. In *52nd Lunar and Planetary Science Conference*.
- 1732 Gendrin, A., Mangold, N., Bibring, J.-P., Langevin, Y., Gondet, B., Poulet, F.,
 1733 ... LeMoulic, S. (2005, March). Sulfates in Martian Layered Terrains: The
 1734

- 1735 OMEGA/Mars Express View. *Science*, 307(5715), 1587–1591. Retrieved 2020-
1736 03-27, from <http://science.sciencemag.org/content/307/5715/1587> doi:
1737 10.1126/science.1109087
- 1738 Goudge, T. A., Mustard, J. F., Head, J. W., Fassett, C. I., & Wiseman, S. M.
1739 (2015, April). Assessing the mineralogy of the watershed and fan de-
1740 posits of the Jezero crater paleolake system, Mars. *Journal of Geophysi-
1741 cal Research: Planets*, 120(4), 2014JE004782. Retrieved 2018-03-14, from
1742 <http://onlinelibrary.wiley.com/doi/10.1002/2014JE004782/abstract>
1743 doi: 10.1002/2014JE004782
- 1744 Hanley, J., Chevrier, V. F., Davis, B. L., Altheide, T. S., & Francis, A. (2009,
1745 July). Reflectance Spectra of Low-Temperature Chloride and Perchlo-
1746 rate Hydrates and Their Relevance to the Martian Surface. In (Vol. 1502,
1747 p. 16). Retrieved 2022-03-07, from [https://ui.adsabs.harvard.edu/abs/
1748 2009LPICo1502...16H](https://ui.adsabs.harvard.edu/abs/2009LPICo1502...16H) (ADS Bibcode: 2009LPICo1502...16H)
- 1749 Hapke, B. (1993). *Theory of Reflectance and Emittance Spectroscopy*.
1750 Cambridge University Press. Retrieved 2020-08-24, from [/core/
1751 books/theory-of-reflectance-and-emittance-spectroscopy/
1752 4DE2B656DD8CCD9F75F12C66128D83D2](http://core/books/theory-of-reflectance-and-emittance-spectroscopy/4DE2B656DD8CCD9F75F12C66128D83D2)
- 1753 Harder, H. (1976, October). Nontronite synthesis at low temperatures. *Chem-
1754 ical Geology*, 18(3), 169–180. Retrieved 2022-02-18, from [https://
1755 www.sciencedirect.com/science/article/pii/0009254176900012](https://www.sciencedirect.com/science/article/pii/0009254176900012) doi:
1756 10.1016/0009-2541(76)90001-2
- 1757 Harloff, J., & Arnold, G. (2001, February). Near-infrared reflectance spec-
1758 troscopy of bulk analog materials for planetary crust. *Planetary and
1759 Space Science*, 49(2), 191–211. Retrieved 2020-08-22, from [http://
1760 www.sciencedirect.com/science/article/pii/S003206330000132X](http://www.sciencedirect.com/science/article/pii/S003206330000132X) doi:
1761 10.1016/S0032-0633(00)00132-X
- 1762 Harner, P. L., & Gilmore, M. S. (2015, April). Visible-near infrared spectra of
1763 hydrous carbonates, with implications for the detection of carbonates in hy-
1764 perspectral data of Mars. *Icarus*, 250, 204–214. Retrieved 2020-05-07, from
1765 <http://www.sciencedirect.com/science/article/pii/S0019103514006782>
1766 doi: 10.1016/j.icarus.2014.11.037
- 1767 Hartmann, W. K., & Neukum, G. (2001). Cratering Chronology and the Evolution
1768 of Mars. In *Chronology and Evolution of Mars* (pp. 165–194). Springer, Dor-
1769 drecht. Retrieved 2018-03-14, from [https://link.springer.com/chapter/10
1770 .1007/978-94-017-1035-0_6](https://link.springer.com/chapter/10.1007/978-94-017-1035-0_6)
- 1771 Hausrath, E. M., Adcock, C. T., Bechtold, A., Beck, P., Brown, A., Cardarelli,
1772 E. L., . . . Regolith Working Group (2022, March). Examining Soil Crusts
1773 at Jezero Crater, Mars. In (Vol. 2678, p. 1604). Retrieved 2022-08-18, from
1774 <https://ui.adsabs.harvard.edu/abs/2022LPICo2678.1604H> (Conference
1775 Name: LPI Contributions ADS Bibcode: 2022LPICo2678.1604H)
- 1776 Hoefen, T. M., Clark, R. N., Bandfield, J. L., Smith, M. D., Pearl, J. C., & Chris-
1777 tensen, P. R. (2003, October). Discovery of Olivine in the Nili Fossae
1778 Region of Mars. *Science*, 302(5645), 627–630. Retrieved 2018-03-14,
1779 from <http://science.sciencemag.org/content/302/5645/627> doi:
1780 10.1126/science.1089647
- 1781 Holm-Alwmark, S., Kinch, K. M., Hansen, M. D., Shahrzad, S., Svennevig,
1782 K., Abbey, W. J., . . . Quantin-Nataf, C. (2021). Stratigraphic Rela-
1783 tionships in Jezero Crater, Mars: Constraints on the Timing of Fluvial-
1784 Lacustrine Activity From Orbital Observations. *Journal of Geophysical
1785 Research: Planets*, 126(7), e2021JE006840. Retrieved 2021-11-18, from
1786 <https://onlinelibrary.wiley.com/doi/abs/10.1029/2021JE006840>
1787 (_eprint: <https://onlinelibrary.wiley.com/doi/pdf/10.1029/2021JE006840>)
1788 doi: 10.1029/2021JE006840
- 1789 Horgan, B. H. N., Anderson, R. B., Dromart, G., Amador, E. S., & Rice, M. S.

- 1790 (2020, March). The mineral diversity of Jezero crater: Evidence for possi-
 1791 ble lacustrine carbonates on Mars. *Icarus*, 339, 113526. Retrieved 2022-
 1792 04-18, from [https://www.sciencedirect.com/science/article/pii/](https://www.sciencedirect.com/science/article/pii/S0019103518306067)
 1793 S0019103518306067 doi: 10.1016/j.icarus.2019.113526
- 1794 Horgan, B. H. N., Cloutis, E. A., Mann, P., & Bell, J. F. (2014, May). Near-infrared
 1795 spectra of ferrous mineral mixtures and methods for their identification in
 1796 planetary surface spectra. *Icarus*, 234, 132–154. Retrieved 2020-08-03, from
 1797 <http://www.sciencedirect.com/science/article/pii/S0019103514001171>
 1798 doi: 10.1016/j.icarus.2014.02.031
- 1799 Hyvrinen, A., & Oja, E. (2000, June). Independent component analysis: al-
 1800 gorithms and applications. *Neural Networks*, 13(4), 411–430. Retrieved
 1801 2022-05-09, from [https://www.sciencedirect.com/science/article/pii/](https://www.sciencedirect.com/science/article/pii/S0893608000000265)
 1802 S0893608000000265 doi: 10.1016/S0893-6080(00)00026-5
- 1803 Irwin, R. P., Howard, A. D., Craddock, R. A., & Moore, J. M. (2005). An in-
 1804 tense terminal epoch of widespread fluvial activity on early Mars: 2. In-
 1805 creased runoff and paleolake development. *Journal of Geophysical Re-*
 1806 *search: Planets*, 110(E12). Retrieved 2020-09-21, from [https://agupubs](https://agupubs.onlinelibrary.wiley.com/doi/abs/10.1029/2005JE002460%4010.1002/%28ISSN%292169-9100.EARLYMARS1)
 1807 [.onlinelibrary.wiley.com/doi/abs/10.1029/2005JE002460%4010.1002/](https://agupubs.onlinelibrary.wiley.com/doi/abs/10.1029/2005JE002460%4010.1002/%28ISSN%292169-9100.EARLYMARS1)
 1808 [%28ISSN%292169-9100.EARLYMARS1](https://agupubs.onlinelibrary.wiley.com/doi/abs/10.1029/2005JE002460%4010.1002/%28ISSN%292169-9100.EARLYMARS1) doi: 10.1029/2005JE002460
- 1809 Johnson, J. R., Bell, J. F., Bender, S., Blaney, D., Cloutis, E., DeFlores, L., ...
 1810 Wiens, R. C. (2015, March). ChemCam passive reflectance spectroscopy
 1811 of surface materials at the Curiosity landing site, Mars. *Icarus*, 249, 74–92.
 1812 Retrieved 2022-04-11, from [https://www.sciencedirect.com/science/](https://www.sciencedirect.com/science/article/pii/S0019103514001146)
 1813 [article/pii/S0019103514001146](https://www.sciencedirect.com/science/article/pii/S0019103514001146) doi: 10.1016/j.icarus.2014.02.028
- 1814 Johnson, J. R., Leget, C., Wiens, R. C., Newell, R. T., Cloutis, E., Forni, O.,
 1815 ... Hayes, A. (2022, March). Visible Wavelength Spectroscopy (400-
 1816 1020 Nm) of Surface Materials at Jezero Crater, Mars, from Supercam
 1817 and Mastcam-Z. In (Vol. 2678, p. 1254). Retrieved 2022-08-18, from
 1818 <https://ui.adsabs.harvard.edu/abs/2022LPICo2678.1254J> (Conference
 1819 Name: LPI Contributions ADS Bibcode: 2022LPICo2678.1254J)
- 1820 Klima, R. L., Pieters, C. M., & Dyar, M. D. (2007). Spectroscopy of synthetic
 1821 Mg-Fe pyroxenes I: Spin-allowed and spin-forbidden crystal field bands in
 1822 the visible and near-infrared. *Meteoritics & Planetary Science*, 42(2), 235–
 1823 253. Retrieved 2020-06-30, from [http://onlinelibrary.wiley.com/doi/](http://onlinelibrary.wiley.com/doi/abs/10.1111/j.1945-5100.2007.tb00230.x)
 1824 [abs/10.1111/j.1945-5100.2007.tb00230.x](http://onlinelibrary.wiley.com/doi/abs/10.1111/j.1945-5100.2007.tb00230.x) doi: 10.1111/j.1945-5100.2007
 1825 .tb00230.x
- 1826 Korablev, O. I., Dobrolensky, Y., Evdokimova, N., Fedorova, A. A., Kuzmin, R. O.,
 1827 Mantsevich, S. N., ... Ivanov, A. Y. (2017, July). Infrared Spectrometer for
 1828 ExoMars: A Mast-Mounted Instrument for the Rover. *Astrobiology*, 17(6-7),
 1829 542–564. Retrieved 2020-09-21, from [http://www.liebertpub.com/doi/](http://www.liebertpub.com/doi/10.1089/ast.2016.1543)
 1830 [10.1089/ast.2016.1543](http://www.liebertpub.com/doi/10.1089/ast.2016.1543) doi: 10.1089/ast.2016.1543
- 1831 Kreisch, C. D., O’Sullivan, J. A., Arvidson, R. E., Politte, D. V., He, L., Stein,
 1832 N. T., ... Laptre, M. G. A. (2017, January). Regularization of Mars Recon-
 1833 naissance Orbiter CRISM alongtrack oversampled hyperspectral imaging obser-
 1834 vations of Mars. *Icarus*, 282, 136–151. Retrieved 2022-05-17, from [https://](https://www.sciencedirect.com/science/article/pii/S0019103516301579)
 1835 www.sciencedirect.com/science/article/pii/S0019103516301579 doi:
 1836 10.1016/j.icarus.2016.09.033
- 1837 Kremer, C. H., Mustard, J. F., & Bramble, M. S. (2019, April). A widespread
 1838 olivine-rich ash deposit on Mars. *Geology*, 47(7), 677–681. Retrieved 2019-
 1839 05-30, from [https://pubs.geoscienceworld.org/gsa/geology/article](https://pubs.geoscienceworld.org/gsa/geology/article-abstract/570813/a-widespread-olivine-rich-ash-deposit-on-mars)
 1840 [-abstract/570813/a-widespread-olivine-rich-ash-deposit-on-mars](https://pubs.geoscienceworld.org/gsa/geology/article-abstract/570813/a-widespread-olivine-rich-ash-deposit-on-mars)
 1841 doi: 10.1130/G45563.1
- 1842 Lantz, C., Poulet, F., Loizeau, D., Riu, L., Pilorget, C., Carter, J., ... Werner,
 1843 S. C. (2020, September). Planetary Terrestrial Analogues Library
 1844 project: 1. characterization of samples by near-infrared point spectrome-

- 1845 ter. *Planetary and Space Science*, 189, 104989. Retrieved 2020-10-16, from
 1846 <http://www.sciencedirect.com/science/article/pii/S0032063320300246>
 1847 doi: 10.1016/j.pss.2020.104989
- 1848 Legett, C., Newell, R. T., Reyes-Newell, A. L., Nelson, A. E., Bernardi, P., Ben-
 1849 der, S. C., ... Wiens, R. C. (2022, April). Optical calibration of the Su-
 1850 perCam instrument body unit spectrometers. *Applied Optics*, 61(11),
 1851 2967–2974. Retrieved 2022-04-11, from [https://opg.optica.org/ao/](https://opg.optica.org/ao/abstract.cfm?uri=ao-61-11-2967)
 1852 [abstract.cfm?uri=ao-61-11-2967](https://opg.optica.org/ao/abstract.cfm?uri=ao-61-11-2967) (Publisher: Optica Publishing Group)
 1853 doi: 10.1364/AO.447680
- 1854 Le Moulic, S., Sotin, C., Combe, J. P., Ledoit, L., Gendrin, A., Mustard, J., ...
 1855 Pinet, P. (2006, March). Composition of the Dust on Mars Derived from
 1856 OMEGA Hyperspectral Images. In (p. 1409). Retrieved 2022-02-01, from
 1857 <https://ui.adsabs.harvard.edu/abs/2006LPI....37.1409L> (ADS Bib-
 1858 code: 2006LPI....37.1409L)
- 1859 Liu, Y., Tice, M. M., Schmidt, M. E., Treiman, A. H., Kizovski, T. V., Hurowitz,
 1860 J. A., ... Zorzano, M.-P. (2022, August). An olivine cumulate outcrop
 1861 on the floor of Jezero crater, Mars. *Science*, eabo2756. Retrieved 2022-
 1862 08-27, from <https://www.science.org/doi/10.1126/science.abo2756>
 1863 (Publisher: American Association for the Advancement of Science) doi:
 1864 10.1126/science.abo2756
- 1865 Liu, Y., Wu, X., Zhao, Y.-Y. S., Pan, L., Wang, C., Liu, J., ... Zou, Y. (2022,
 1866 May). Zhurong reveals recent aqueous activities in Utopia Planitia, Mars. *Sci-*
 1867 *ence Advances*. Retrieved 2022-05-27, from [https://www.science.org/doi/](https://www.science.org/doi/full/10.1126/sciadv.abn8555)
 1868 [full/10.1126/sciadv.abn8555](https://www.science.org/doi/full/10.1126/sciadv.abn8555) (Publisher: American Association for the
 1869 Advancement of Science) doi: 10.1126/sciadv.abn8555
- 1870 Maki, J. M. (2021). *Mars 2020 Hazard Cameras Bundle, raw products*. (Publisher:
 1871 NASA Planetary Data System. doi: 10.17189/282B-1524)
- 1872 Maki, J. N., Gruel, D., McKinney, C., Ravine, M. A., Morales, M., Lee, D., ... Al-
 1873 germissen, S. (2020, November). The Mars 2020 Engineering Cameras and
 1874 Microphone on the Perseverance Rover: A Next-Generation Imaging Sys-
 1875 tem for Mars Exploration. *Space Science Reviews*, 216(8), 137. Retrieved
 1876 2022-05-05, from <https://doi.org/10.1007/s11214-020-00765-9> doi:
 1877 10.1007/s11214-020-00765-9
- 1878 Mandon, L. (2020). *Prparation des futures missions in situ martiennes via la tld-*
 1879 *tection et l'expérimentation en spectroscopie de réflectance* (These de doctorat,
 1880 Lyon). Retrieved 2021-09-02, from <https://www.theses.fr/2020LYSE1261>
- 1881 Mandon, L., Beck, P., Quantin-Nataf, C., Dehouck, E., Pommerol, A., Yoldi, Z., ...
 1882 Sautter, V. (2021, May). Martian meteorites reflectance and implications for
 1883 rover missions. *Icarus*, 366, 114517. Retrieved 2021-05-09, from [https://](https://www.sciencedirect.com/science/article/pii/S0019103521001925)
 1884 www.sciencedirect.com/science/article/pii/S0019103521001925 doi:
 1885 10.1016/j.icarus.2021.114517
- 1886 Mandon, L., Beck, P., Quantin-Nataf, C., Dehouck, E., Thollot, P., Loizeau,
 1887 D., & Volat, M. (2022). ROMA: A Database of Rock Reflectance
 1888 Spectra for Martian In Situ Exploration. *Earth and Space Sci-*
 1889 *ence*, 9(1), e2021EA001871. Retrieved 2022-01-22, from [https://](https://onlinelibrary.wiley.com/doi/abs/10.1029/2021EA001871)
 1890 onlinelibrary.wiley.com/doi/abs/10.1029/2021EA001871 (eprint:
 1891 <https://onlinelibrary.wiley.com/doi/pdf/10.1029/2021EA001871>) doi:
 1892 10.1029/2021EA001871
- 1893 Mandon, L., Parkes Bowen, A., Quantin-Nataf, C., Bridges, J. C., Carter, J., Pan,
 1894 L., ... Thollot, P. (2021, March). Morphological and Spectral Diversity of the
 1895 Clay-Bearing Unit at the ExoMars Landing Site Oxia Planum. *Astrobiology*,
 1896 21(4). Retrieved 2021-03-08, from [https://www.liebertpub.com/doi/full/](https://www.liebertpub.com/doi/full/10.1089/ast.2020.2292)
 1897 [10.1089/ast.2020.2292](https://www.liebertpub.com/doi/full/10.1089/ast.2020.2292) doi: 10.1089/ast.2020.2292
- 1898 Mandon, L., Quantin-Nataf, C., Thollot, P., Mangold, N., Lozac'h, L., Dro-
 1899 mart, G., ... Volat, M. (2020, January). Refining the age, emplace-

- 1900 ment and alteration scenarios of the olivine-rich unit in the Nili Fossae re-
 1901 gion, Mars. *Icarus*, 336, 113436. Retrieved 2019-10-25, from [http://](http://www.sciencedirect.com/science/article/pii/S0019103518306031)
 1902 www.sciencedirect.com/science/article/pii/S0019103518306031 doi:
 1903 10.1016/j.icarus.2019.113436
- 1904 Mangold, N., Dromart, G., Ansan, V., Salese, F., Kleinhans, M. G., Mass, M., ...
 1905 Stack, K. M. (2020, May). Fluvial Regimes, Morphometry, and Age of Jezero
 1906 Crater Paleolake Inlet Valleys and Their Exobiological Significance for the
 1907 2020 Rover Mission Landing Site. *Astrobiology*, 20(8). Retrieved 2020-06-08,
 1908 from <http://www.liebertpub.com/doi/abs/10.1089/ast.2019.2132> doi:
 1909 10.1089/ast.2019.2132
- 1910 Mangold, N., Gupta, S., Gasnault, O., Dromart, G., Tarnas, J. D., Sholes, S. F.,
 1911 ... Williford, K. H. (2021). Perseverance rover reveals an ancient delta-lake
 1912 system and flood deposits at Jezero crater, Mars. *Science*, 0(0), eabl4051.
 1913 Retrieved 2021-10-12, from [https://www.science.org/doi/10.1126/](https://www.science.org/doi/10.1126/science.abl4051)
 1914 [science.abl4051](https://www.science.org/doi/10.1126/science.abl4051) (Publisher: American Association for the Advancement
 1915 of Science) doi: 10.1126/science.abl4051
- 1916 Mangold, N., Poulet, F., Mustard, J. F., Bibring, J.-P., Gondet, B., Langevin, Y.,
 1917 ... Neukum, G. (2007, August). Mineralogy of the Nili Fossae region with
 1918 OMEGA/Mars Express data: 2. Aqueous alteration of the crust. *Journal of*
 1919 *Geophysical Research: Planets*, 112(E8), E08S04. Retrieved 2018-03-14, from
 1920 <http://onlinelibrary.wiley.com/doi/10.1029/2006JE002835/abstract>
 1921 doi: 10.1029/2006JE002835
- 1922 Manrique, J. A., Lopez-Reyes, G., Cousin, A., Rull, F., Maurice, S., Wiens, R. C.,
 1923 ... Veneranda, M. (2020, November). SuperCam Calibration Targets: De-
 1924 sign and Development. *Space Science Reviews*, 216(8), 138. Retrieved
 1925 2022-04-05, from <https://doi.org/10.1007/s11214-020-00764-w> doi:
 1926 10.1007/s11214-020-00764-w
- 1927 Mass, M., Bourgeois, O., Le Moulic, S., Verpoorter, C., Le Deit, L., & Bibring, J. P.
 1928 (2010, October). Martian polar and circum-polar sulfate-bearing deposits:
 1929 Sublimation tills derived from the North Polar Cap. *Icarus*, 209(2), 434–
 1930 451. Retrieved 2022-03-14, from [https://www.sciencedirect.com/science/](https://www.sciencedirect.com/science/article/pii/S0019103510001740)
 1931 [article/pii/S0019103510001740](https://www.sciencedirect.com/science/article/pii/S0019103510001740) doi: 10.1016/j.icarus.2010.04.017
- 1932 Masursky, H. (1973). An overview of geological results from Mariner 9. *Jour-*
 1933 *nal of Geophysical Research (1896-1977)*, 78(20), 4009–4030. Retrieved
 1934 2020-10-10, from [http://agupubs.onlinelibrary.wiley.com/doi/abs/](http://agupubs.onlinelibrary.wiley.com/doi/abs/10.1029/JB078i020p04009%4010.1002/%28ISSN%292169-9356.MARINER9)
 1935 [10.1029/JB078i020p04009%4010.1002/%28ISSN%292169-9356.MARINER9](http://agupubs.onlinelibrary.wiley.com/doi/abs/10.1029/JB078i020p04009%4010.1002/%28ISSN%292169-9356.MARINER9)
 1936 doi: 10.1029/JB078i020p04009
- 1937 Maurice, & Wiens, R. C. (2021). *Mars 2020 SuperCam Bundle*. (Publisher: NASA
 1938 Planetary Data System. doi: 10.17189/1522646)
- 1939 Maurice, S., Clegg, S. M., Wiens, R. C., Gasnault, O., Rapin, W., Forni, O., ...
 1940 Vasavada, A. R. (2016, March). ChemCam activities and discoveries during
 1941 the nominal mission of the Mars Science Laboratory in Gale crater, Mars.
 1942 *Journal of Analytical Atomic Spectrometry*, 31(4), 863–889. Retrieved
 1943 2022-06-26, from [https://pubs.rsc.org/en/content/articlelanding/](https://pubs.rsc.org/en/content/articlelanding/2016/ja/c5ja00417a)
 1944 [2016/ja/c5ja00417a](https://pubs.rsc.org/en/content/articlelanding/2016/ja/c5ja00417a) (Publisher: The Royal Society of Chemistry) doi:
 1945 10.1039/C5JA00417A
- 1946 Maurice, S., Wiens, R. C., Bernardi, P., Cas, P., Robinson, S., Nelson, T., ... Wong,
 1947 K. W. (2021, April). The SuperCam Instrument Suite on the Mars 2020
 1948 Rover: Science Objectives and Mast-Unit Description. *Space Science Re-*
 1949 *views*, 217(3), 47. Retrieved 2021-05-10, from [https://doi.org/10.1007/](https://doi.org/10.1007/s11214-021-00807-w)
 1950 [s11214-021-00807-w](https://doi.org/10.1007/s11214-021-00807-w) doi: 10.1007/s11214-021-00807-w
- 1951 McEwen, A. S., Eliason, E. M., Bergstrom, J. W., Bridges, N. T., Hansen, C. J.,
 1952 Delamere, W. A., ... Weitz, C. M. (2007, May). Mars Reconnaissance Or-
 1953 biter's High Resolution Imaging Science Experiment (HiRISE). *Journal of*
 1954 *Geophysical Research: Planets*, 112(E5), E05S02. Retrieved 2018-03-14, from

- 1955 <http://onlinelibrary.wiley.com/doi/10.1029/2005JE002605/abstract>
 1956 doi: 10.1029/2005JE002605
- 1957 Meslin, P. Y., Forni, O., Beck, P., Cousin, A., Beyssac, O., Lopez-Reyes, G.,
 1958 ... Zorzano, M. P. (2022, March). Evidence for Perchlorate and Sulfate
 1959 Salts in Jezero Crater, Mars, from Supercam Observations. In (Vol. 2678,
 1960 p. 2694). Retrieved 2022-08-18, from [https://ui.adsabs.harvard.edu/abs/](https://ui.adsabs.harvard.edu/abs/2022LPICo2678.2694M)
 1961 [2022LPICo2678.2694M](https://ui.adsabs.harvard.edu/abs/2022LPICo2678.2694M) (Conference Name: LPI Contributions ADS Bibcode:
 1962 [2022LPICo2678.2694M](https://ui.adsabs.harvard.edu/abs/2022LPICo2678.2694M))
- 1963 Milliken, R. E., & Bish, D. L. (2014, March). Distinguishing Hisingerite from
 1964 Other Clays and its Importance for Mars. In (p. 2251). Retrieved 2022-01-12,
 1965 from <https://ui.adsabs.harvard.edu/abs/2014LPI...45.2251M> (ADS
 1966 Bibcode: 2014LPI...45.2251M)
- 1967 Muirhead, B. K., Nicholas, A. K., Umland, J., Sutherland, O., & Vijendran,
 1968 S. (2020, November). Mars Sample Return Campaign Concept Sta-
 1969 tus. *Acta Astronautica*, 176, 131–138. Retrieved 2020-08-12, from
 1970 <http://www.sciencedirect.com/science/article/pii/S0094576520303933>
 1971 doi: 10.1016/j.actaastro.2020.06.026
- 1972 Murchie, S., Arvidson, R., Bedini, P., Beisser, K., Bibring, J.-P., Bishop, J., ...
 1973 Wolff, M. (2007, May). Compact Reconnaissance Imaging Spectrometer
 1974 for Mars (CRISM) on Mars Reconnaissance Orbiter (MRO). *Journal of*
 1975 *Geophysical Research: Planets*, 112(E5), 1–57. Retrieved 2018-03-14, from
 1976 <http://onlinelibrary.wiley.com/doi/10.1029/2006JE002682/abstract>
 1977 doi: 10.1029/2006JE002682
- 1978 Mustard, J. F., Ehlmann, B. L., Murchie, S. L., Poulet, F., Mangold, N., Head,
 1979 J. W., ... Roach, L. H. (2009, February). Composition, Morphology, and
 1980 Stratigraphy of Noachian Crust around the Isidis basin. *Journal of Geo-*
 1981 *physical Research: Planets*, 114(E2), E00D12. Retrieved 2018-03-14, from
 1982 <http://onlinelibrary.wiley.com/doi/10.1029/2009JE003349/abstract>
 1983 doi: 10.1029/2009JE003349
- 1984 Mustard, J. F., Poulet, F., Gendrin, A., Bibring, J.-P., Langevin, Y., Gondet,
 1985 B., ... Altieri, F. (2005, March). Olivine and Pyroxene Diversity in the
 1986 Crust of Mars. *Science*, 307(5715), 1594–1597. Retrieved 2018-03-14,
 1987 from <http://science.sciencemag.org/content/307/5715/1594> doi:
 1988 10.1126/science.1109098
- 1989 Mustard, J. F., Poulet, F., Head, J. W., Mangold, N., Bibring, J.-P., Pelkey, S. M.,
 1990 ... Neukum, G. (2007, August). Mineralogy of the Nili Fossae region with
 1991 OMEGA/Mars Express data: 1. Ancient impact melt in the Isidis Basin and
 1992 implications for the transition from the Noachian to Hesperian. *Journal of*
 1993 *Geophysical Research: Planets*, 112(E8), E08S03. Retrieved 2018-03-14, from
 1994 <http://onlinelibrary.wiley.com/doi/10.1029/2006JE002834/abstract>
 1995 doi: 10.1029/2006JE002834
- 1996 Ody, A., Poulet, F., Bibring, J.-P., Loizeau, D., Carter, J., Gondet, B., & Langevin,
 1997 Y. (2013, February). Global investigation of olivine on Mars: Insights into
 1998 crust and mantle compositions. *Journal of Geophysical Research: Planets*,
 1999 118(2), 234–262. Retrieved 2018-03-14, from [http://onlinelibrary.wiley](http://onlinelibrary.wiley.com/doi/10.1029/2012JE004149/abstract)
 2000 [.com/doi/10.1029/2012JE004149/abstract](http://onlinelibrary.wiley.com/doi/10.1029/2012JE004149/abstract) doi: 10.1029/2012JE004149
- 2001 Palumbo, A. M., & Head, J. W. (2018). Impact cratering as a cause of climate
 2002 change, surface alteration, and resurfacing during the early history of Mars.
 2003 *Meteoritics & Planetary Science*, 53(4), 687–725. Retrieved 2019-02-11, from
 2004 <https://onlinelibrary.wiley.com/doi/abs/10.1111/maps.13001> doi:
 2005 10.1111/maps.13001
- 2006 Poulet, F., Bibring, J.-P., Mustard, J. F., Gendrin, A., Mangold, N., Langevin,
 2007 Y., ... Forget, F. (2005, December). Phyllosilicates on Mars and impli-
 2008 cations for early martian climate. *Nature*, 438(7068), 623–627. Retrieved
 2009 2018-03-14, from <https://www.nature.com/articles/nature04274> doi:

- 2010 10.1038/nature04274
- 2011 Poulet, F., Royer, C., Beck, P., Mandon, L., Quantin-Nataf, C., Johnson, J. R.,
2012 ... Wiens, R. C. (2022, March). Modal Mineralogy of Seitah Unit in
2013 Jezero Crater (Mars) Retrieved from Nonlinear Unmixing Analyses of
2014 IRS/SUPERCAM. In (Vol. 2678, p. 2032). Retrieved 2022-05-16, from
2015 <https://ui.adsabs.harvard.edu/abs/2022LPICo2678.2032P> (ADS Bib-
2016 code: 2022LPICo2678.2032P)
- 2017 Quantin-Nataf, C., Holm-Alwmark, S., Lasue, J., Calef, F. J., Shuster, D., Kinch,
2018 K. M., ... Brown, A. (2021, March). The Complex Exhumation History
2019 of Jezero Crater Floor Unit. In (p. 2034). Retrieved 2022-08-18, from
2020 <https://ui.adsabs.harvard.edu/abs/2021LPI...52.2034Q> (Confer-
2021 ence Name: 52nd Lunar and Planetary Science Conference ADS Bibcode:
2022 2021LPI...52.2034Q)
- 2023 Razzell Hollis, J., Moore, K. R., Sharma, S., Beegle, L., Grotzinger, J. P., All-
2024 wood, A., ... Yanchilina, A. (2022, November). The power of paired
2025 proximity science observations: Co-located data from SHERLOC and PIXL
2026 on Mars. *Icarus*, 387, 115179. Retrieved 2022-08-27, from [https://](https://www.sciencedirect.com/science/article/pii/S0019103522002809)
2027 www.sciencedirect.com/science/article/pii/S0019103522002809 doi:
2028 10.1016/j.icarus.2022.115179
- 2029 Roach, L. H., Mustard, J. F., Lane, M. D., Bishop, J. L., & Murchie, S. L.
2030 (2010, June). Diagenetic haematite and sulfate assemblages in Valles
2031 Marineris. *Icarus*, 207(2), 659–674. Retrieved 2021-10-18, from [https://](https://www.sciencedirect.com/science/article/pii/S0019103509004758)
2032 www.sciencedirect.com/science/article/pii/S0019103509004758 doi:
2033 10.1016/j.icarus.2009.11.029
- 2034 Rogers, A. D., Warner, N. H., Golombek, M. P., Head III, J. W., & Cowart, J. C.
2035 (2018, February). Areally Extensive Surface Bedrock Exposures on Mars:
2036 Many Are Clastic Rocks, Not Lavas. *Geophysical Research Letters*, 45(4),
2037 1767–1777. Retrieved 2018-12-21, from [http://agupubs.onlinelibrary](http://agupubs.onlinelibrary.wiley.com/doi/10.1002/2018GL077030)
2038 [.wiley.com/doi/10.1002/2018GL077030](http://agupubs.onlinelibrary.wiley.com/doi/10.1002/2018GL077030) doi: 10.1002/2018GL077030
- 2039 Royer, C., Fouchet, T., Montmessin, F., Poulet, F., Forni, O., Johnson, J. R., ...
2040 Wiens, R. C. (2022, March). The Detection of Spectral Signatures with
2041 IRS/SuperCam, Perseverance Rover: Instrument Performance. In (Vol. 2678,
2042 p. 1840). Retrieved 2022-08-18, from [https://ui.adsabs.harvard.edu/abs/](https://ui.adsabs.harvard.edu/abs/2022LPICo2678.1840R)
2043 [2022LPICo2678.1840R](https://ui.adsabs.harvard.edu/abs/2022LPICo2678.1840R) (Conference Name: LPI Contributions ADS Bibcode:
2044 2022LPICo2678.1840R)
- 2045 Scheller, E. L., & Ehlmann, B. L. (2020). Composition, Stratigraphy, and Geolog-
2046 ical History of the Noachian Basement Surrounding the Isidis Impact Basin.
2047 *Journal of Geophysical Research: Planets*, e2019JE006190. Retrieved 2020-
2048 05-30, from [http://agupubs.onlinelibrary.wiley.com/doi/abs/10.1029/](http://agupubs.onlinelibrary.wiley.com/doi/abs/10.1029/2019JE006190)
2049 [2019JE006190](http://agupubs.onlinelibrary.wiley.com/doi/abs/10.1029/2019JE006190) doi: 10.1029/2019JE006190
- 2050 Schon, S. C., Head, J. W., & Fassett, C. I. (2012, July). An overfilled lacustrine
2051 system and progradational delta in Jezero crater, Mars: Implications for
2052 Noachian climate. *Planetary and Space Science*, 67(1), 28–45. Retrieved
2053 2018-03-14, from [http://www.sciencedirect.com/science/article/pii/](http://www.sciencedirect.com/science/article/pii/S003206331200044X)
2054 [S003206331200044X](http://www.sciencedirect.com/science/article/pii/S003206331200044X) doi: 10.1016/j.pss.2012.02.003
- 2055 Schrder, S., Meslin, P. Y., Gasnault, O., Maurice, S., Cousin, A., Wiens, R. C.,
2056 ... Vaniman, D. (2015, March). Hydrogen detection with ChemCam at
2057 Gale crater. *Icarus*, 249, 43–61. Retrieved 2022-03-28, from [https://](https://www.sciencedirect.com/science/article/pii/S001910351400445X)
2058 www.sciencedirect.com/science/article/pii/S001910351400445X doi:
2059 10.1016/j.icarus.2014.08.029
- 2060 Shahrzad, S., Kinch, K. M., Goudge, T. A., Fassett, C. I., Needham, D. H.,
2061 QuantinNataf, C., & Knudsen, C. P. (2019). Crater Statistics on the
2062 Dark-Toned, Mafic Floor Unit in Jezero Crater, Mars. *Geophysical Re-*
2063 *search Letters*, 46(5), 2408–2416. Retrieved 2020-07-17, from [http://](http://agupubs.onlinelibrary.wiley.com/doi/abs/10.1029/2018GL081402)
2064 agupubs.onlinelibrary.wiley.com/doi/abs/10.1029/2018GL081402 doi:

- 2065 10.1029/2018GL081402
- 2066 Simon, J. I., Amundsen, H. E. F., Beegle, L. W., Bell, J., Benison, K. C., Berger,
2067 E. L., ... Zorzano, M.-P. (2022, March). Sampling of Jezero Crater Maz For-
2068 mation By Mars 2020 Perseverance Rover. Houston, TX. Retrieved 2022-08-
2069 18, from <https://ntrs.nasa.gov/citations/20210026260> (NTRS Author
2070 Affiliations: Johnson Space Center, University of Oslo, Jet Propulsion Lab,
2071 Arizona State University, West Virginia University, Jacobs (United States),
2072 Massachusetts Institute of Technology, University of Cincinnati, Goddard
2073 Space Flight Center, Universit Libre de Bruxelles, Centro de Astrobiologia,
2074 California Institute of Technology, Universities Space Research Association,
2075 University of Nevada, Las Vegas, University of Alberta, Purdue University
2076 West Lafayette, Lunar and Planetary Institute, Paris Observatory, University
2077 of Toulouse, University of the Basque Country, University of Colorado Boulder,
2078 Stony Brook University, RISE Research Institutes of Sweden, University of
2079 California, Berkeley, Washington University in St. Louis, Los Alamos National
2080 Laboratory, University of Aberdeen NTRS Document ID: 20210026260 NTRS
2081 Research Center: Johnson Space Center (JSC))
- 2082 Stack, K. M., Williams, N. R., Calef, F., Sun, V. Z., Williford, K. H., Farley,
2083 K. A., ... Aileen Yingst, R. (2020, November). Photogeologic Map of
2084 the Perseverance Rover Field Site in Jezero Crater Constructed by the
2085 Mars 2020 Science Team. *Space Science Reviews*, 216(8), 127. Retrieved
2086 2021-05-26, from <https://doi.org/10.1007/s11214-020-00739-x> doi:
2087 10.1007/s11214-020-00739-x
- 2088 Stopar, J. D., Jeffrey Taylor, G., Hamilton, V. E., & Browning, L. (2006, Decem-
2089 ber). Kinetic model of olivine dissolution and extent of aqueous alteration
2090 on mars. *Geochimica et Cosmochimica Acta*, 70(24), 6136–6152. Retrieved
2091 2019-07-15, from [http://www.sciencedirect.com/science/article/pii/](http://www.sciencedirect.com/science/article/pii/S0016703706020102)
2092 [S0016703706020102](http://www.sciencedirect.com/science/article/pii/S0016703706020102) doi: 10.1016/j.gca.2006.07.039
- 2093 Thollot, P. (2013). *Etude de l'altration de la surface de Mars par imagerie*
2094 *hyperspectrale : minralogie des rgions de Noctis Labyrinthus et Valles*
2095 *Marineris* (Doctoral dissertation, Nantes). Retrieved 2018-06-12, from
2096 <http://www.theses.fr/2013NANT2076>
- 2097 Tornabene, L. L., Moersch, J. E., McSween, H. Y., Hamilton, V. E., Piatek, J. L.,
2098 & Christensen, P. R. (2008, October). Surface and crater-exposed lithologic
2099 units of the Isidis Basin as mapped by coanalysis of THEMIS and TES derived
2100 data products. *Journal of Geophysical Research: Planets*, 113(E10), E10001.
2101 Retrieved 2018-03-14, from [http://onlinelibrary.wiley.com/doi/10.1029/](http://onlinelibrary.wiley.com/doi/10.1029/2007JE002988/abstract)
2102 [2007JE002988/abstract](http://onlinelibrary.wiley.com/doi/10.1029/2007JE002988/abstract) doi: 10.1029/2007JE002988
- 2103 Tutolo, B. M., Evans, B. W., & Kuehner, S. M. (2019, January). SerpentineHisin-
2104 gerite Solid Solution in Altered Ferroan Peridotite and Olivine Gabbro. *Miner-*
2105 *als*, 9(1), 47. Retrieved 2022-05-06, from [https://www.mdpi.com/2075-163X/](https://www.mdpi.com/2075-163X/9/1/47)
2106 [9/1/47](https://www.mdpi.com/2075-163X/9/1/47) (Number: 1 Publisher: Multidisciplinary Digital Publishing Institute)
2107 doi: 10.3390/min9010047
- 2108 Udry, A., Sautter, V., Cousin, A., Wiens, R. C., Forni, O., Benzerara, K., ... Ma-
2109 diaraga, J. M. (2022). A Mars 2020 Perseverance SuperCam Perspective on
2110 the Igneous Nature of the Maz Formation at Jezero Crater, Mars. The Wood-
2111 lands, TX. Retrieved 2022-08-18, from [https://ntrs.nasa.gov/citations/](https://ntrs.nasa.gov/citations/20220000502)
2112 [20220000502](https://ntrs.nasa.gov/citations/20220000502) (NTRS Author Affiliations: University of Nevada, Las Vegas,
2113 Institute de Recherche en Astrophysique et Planetologie, Los Alamos National
2114 Laboratory, Centre national de la recherche scientifique, Institute of Miner-
2115 alogy, Materials Physics and Cosmochemistry, Texas A&M University, ENS
2116 Lyon, Massachusetts Institute of Technology, Laboratoire de Plantologie et Go-
2117 dynamique de Nantes, Johns Hopkins University Applied Physics Laboratory,
2118 Brock University, Purdue University West Lafayette, United States Geological
2119 Survey, Stony Brook University, Johnson Space Center, University of Alberta,

- 2120 University of the Basque Country NTRS Document ID: 20220000502 NTRS
 2121 Research Center: Johnson Space Center (JSC))
- 2122 Vaughan, A., Rice, M., Horgan, B., Johnson, J., Bell, J., Nunez, J., ... Brown,
 2123 A. (2021, December). A Mastcam-Z View of Regolith at Jezero Crater:
 2124 Textural and Spectral Properties. In (Vol. 2021, pp. P25I–2245). Re-
 2125 trieved 2022-08-18, from <https://ui.adsabs.harvard.edu/abs/2021AGUFM>
 2126 .P25I2245V (Conference Name: AGU Fall Meeting Abstracts ADS Bibcode:
 2127 2021AGUFM.P25I2245V)
- 2128 VivianoBeck, C. E., Moersch, J. E., & McSween, H. Y. (2013). Implications for
 2129 early hydrothermal environments on Mars through the spectral evidence for
 2130 carbonation and chloritization reactions in the Nili Fossae region. *Journal of*
 2131 *Geophysical Research: Planets*, 118(9), 1858–1872. Retrieved 2019-01-05, from
 2132 <http://agupubs.onlinelibrary.wiley.com/doi/abs/10.1002/jgre.20141>
 2133 doi: 10.1002/jgre.20141
- 2134 VivianoBeck, C. E., Seelos, F. P., Murchie, S. L., Kahn, E. G., Seelos, K. D., Taylor,
 2135 H. W., ... Morgan, M. F. (2014). Revised CRISM spectral parameters and
 2136 summary products based on the currently detected mineral diversity on Mars.
 2137 *Journal of Geophysical Research: Planets*, 119(6), 1403–1431. Retrieved 2020-
 2138 04-22, from <http://agupubs.onlinelibrary.wiley.com/doi/abs/10.1002/>
 2139 2014JE004627 doi: 10.1002/2014JE004627
- 2140 Werner, S. C. (2008, May). The early martian evolution Constraints from basin
 2141 formation ages. *Icarus*, 195(1), 45–60. Retrieved 2018-05-28, from [http://](http://www.sciencedirect.com/science/article/pii/S0019103507006136)
 2142 www.sciencedirect.com/science/article/pii/S0019103507006136 doi: 10
 2143 .1016/j.icarus.2007.12.008
- 2144 Wiens, R. C., Maurice, S., Robinson, S. H., Nelson, A. E., Cais, P., Bernardi, P.,
 2145 ... Willis, P. (2021). The SuperCam Instrument Suite on the NASA Mars
 2146 2020 Rover: Body Unit and Combined System Tests. *Space Science Re-*
 2147 *views*, 217(1), 4. Retrieved 2021-12-18, from [https://doi.org/10.1007/](https://doi.org/10.1007/s11214-020-00777-5)
 2148 [s11214-020-00777-5](https://doi.org/10.1007/s11214-020-00777-5) doi: 10.1007/s11214-020-00777-5
- 2149 Wiens, R. C., Udry, A., Beyssac, O., Quantin-Nataf, C., Mangold, N., Cousin, A.,
 2150 ... THE SUPERCAM TEAM (2022, August). Compositionally and density
 2151 stratified igneous terrain in Jezero crater, Mars. *Science Advances*, 8(34),
 2152 eabo3399. Retrieved 2022-08-25, from [https://www.science.org/doi/](https://www.science.org/doi/10.1126/sciadv.abo3399)
 2153 [10.1126/sciadv.abo3399](https://www.science.org/doi/10.1126/sciadv.abo3399) (Publisher: American Association for the Advance-
 2154 ment of Science) doi: 10.1126/sciadv.abo3399
- 2155 Wright, J., Barrett, A. M., Fawdon, P., Favaro, E. A., Balme, M. R., Woods,
 2156 M. J., & Karachalios, S. (2022, August). Jezero crater, Mars: applica-
 2157 tion of the deep learning NOAH-H terrain classification system. *Jour-*
 2158 *nal of Maps*, 0(0), 1–13. Retrieved 2022-08-19, from [https://doi.org/](https://doi.org/10.1080/17445647.2022.2095935)
 2159 [10.1080/17445647.2022.2095935](https://doi.org/10.1080/17445647.2022.2095935) (Publisher: Taylor & Francis eprint:
 2160 <https://doi.org/10.1080/17445647.2022.2095935>) doi: 10.1080/17445647.2022
 2161 .2095935
- 2162 Xu, W., Liu, X., Yan, Z., Li, L., Zhang, Z., Kuang, Y., ... Shu, R. (2021, July).
 2163 The MarSCoDe Instrument Suite on the Mars Rover of Chinas Tianwen-1 Mis-
 2164 sion. *Space Science Reviews*, 217(5), 64. Retrieved 2022-02-17, from [https://](https://doi.org/10.1007/s11214-021-00836-5)
 2165 doi.org/10.1007/s11214-021-00836-5 doi: 10.1007/s11214-021-00836-5
- 2166 Yen, A. S., Gellert, R., Schrder, C., Morris, R. V., Bell, J. F., Knudson, A. T., ...
 2167 Zipfel, J. (2005, July). An integrated view of the chemistry and mineral-
 2168 ogy of martian soils. *Nature*, 436(7047), 49–54. Retrieved 2022-05-06, from
 2169 <https://www.nature.com/articles/nature03637> (Number: 7047 Publisher:
 2170 Nature Publishing Group) doi: 10.1038/nature03637
- 2171 Zaini, N., Van der Meer, F., & Van der Werff, H. (2012, April). Effect of Grain Size
 2172 and Mineral Mixing on Carbonate Absorption Features in the SWIR and TIR
 2173 Wavelength Regions. *Remote Sensing*, 4(4), 987–1003. Retrieved 2022-08-27,
 2174 from <https://www.mdpi.com/2072-4292/4/4/987> (Number: 4 Publisher:

Accepted Article

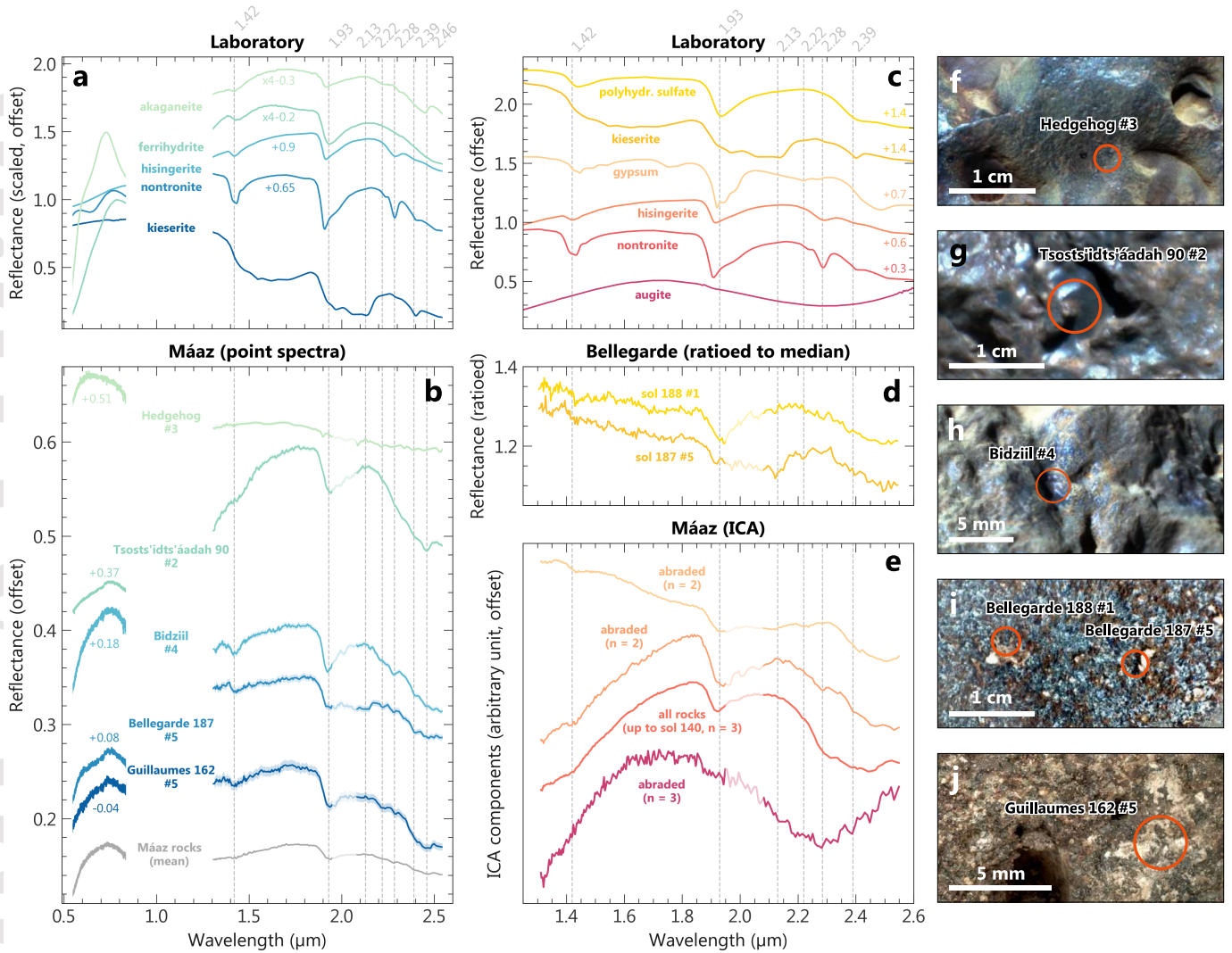


Figure 6: Spectral endmembers of the Mááz formation rocks. (a) Laboratory spectra from the RELAB spectral library (kieserite F1CC15, nontronite CBJB26, hisingerite C1RM137, ferrihydrite C1JB45 and akaganeite C1JB48). (b) Mean spectra of endmember rock targets within the Mááz formation as well as single-point spectra showing similar spectral features as the library spectra displayed in (a). Segments of the spectra shown with lower opacity line near 2 μm correspond to the main atmospheric CO_2 absorption domain, where residuals might affect the spectra. (c) Laboratory spectra from the RELAB spectral library (augite C1SC35, nontronite CBJB26, hisingerite C1RM137, gypsum BKR1JB556, kieserite F1CC15 and polyhydrated sulfate 799F366). (d) Point spectra on the abraded patch *Bellegarde* ratioed to the raster's median and showing similar spectral features as the Mg-sulfates spectra showed in (c), including a large absorption near 2.13 μm . The sol 188 ratioed spectrum has absorptions and spectral shape similar to polyhydrated sulfates; other hydrated minerals such as zeolites can also exhibit the same spectra but are less favored by LIBS analysis (Meslin et al., this issue/Meslin et al., 2022). (e) ICA components showing NIR spectral features similar to the spectra displayed in (c), with n the number of components in input. (f, g, h, i) Contrast-enhanced RMI close-ups on the holey rock *Hedgehog* (f), on a dark filled void of target *Tsosts'id ts'áadah* (g), on target *Bidziil* (h), and on the abraded patch *Bellegarde* (i). (j) WATSON close-up on the abraded patch *Guillaumes*. Red circles indicate the location of the field of view of the IRS accounting for 68% of signal. See supplementary text S1 for image IDs.

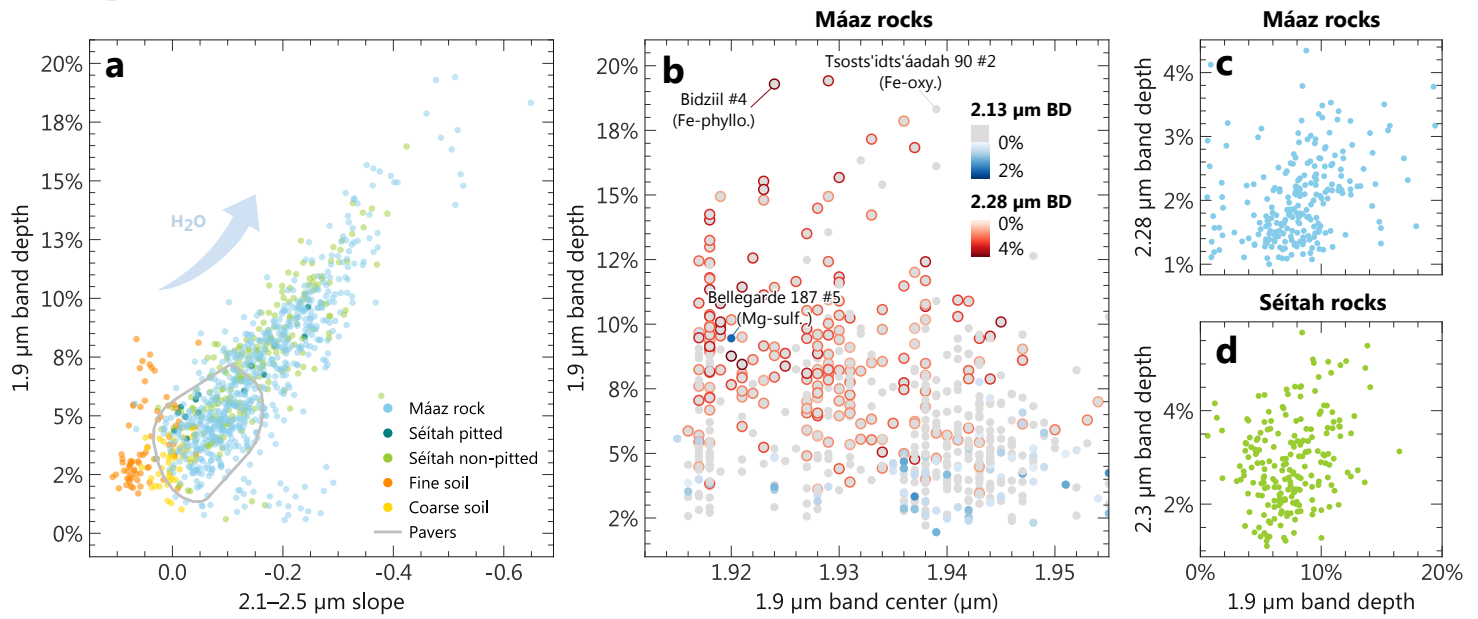


Figure 7: (a) Spectral parameters tracking the hydration signature in the NIR spectra. The pavers' distribution is delimited by the kernel density estimate of the points with an isoproportion level set at 75%. (b) Intensity of the 1.9 μm water absorption as a function of its position, color-coded with the intensity of the 2.28 μm (Fe^{3+} -OH) and 2.13 μm (Mg-sulfate) absorptions (BD: Band Depth). Spectral endmembers identified in Fig. 6b are reported in the plot. (c) Intensity of the 2.28 μm (Fe^{3+} -OH) absorption as a function of the 1.9 μm (water) band depth, showing poor correlation for the Máaz rocks spectra. (d) Intensity of the 2.3 μm absorption (Fe -OH, Mg-OH and CO_3) as a function of the 1.9 μm (water) band depth, showing poor correlation for the Séítah rocks spectra. See table 1 for the parameter definitions.

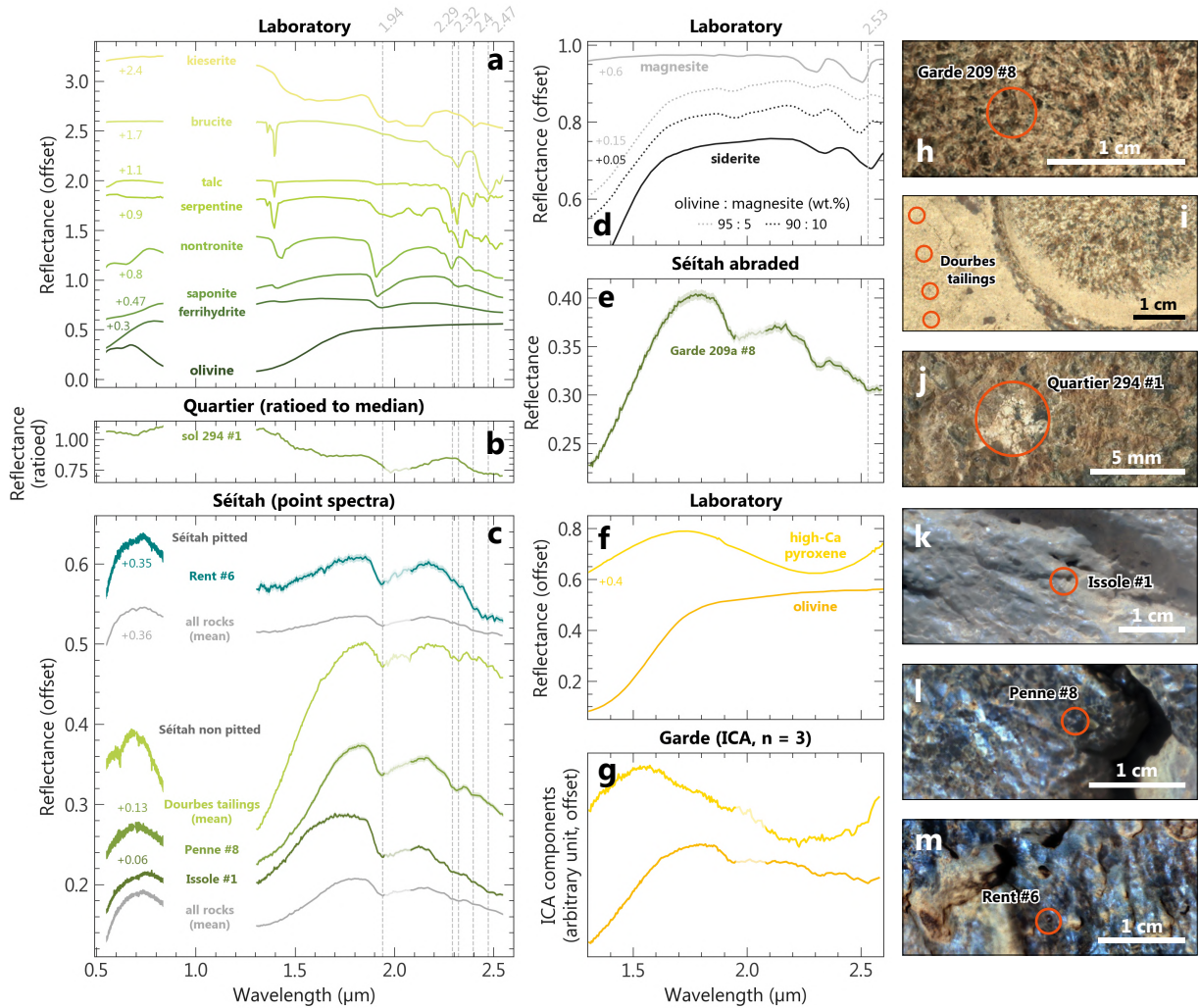


Figure 8: Spectral endmembers of the Séítah formation rocks. (a) Laboratory spectra from the RELAB library (olivine C1PO47, ferrihydrite C1JB45, saponite LASA59, nontronite CBJB26, serpentine LASR10, talc LAEA15, brucite C1JB944 and kieserite F1CC15). (b) Point spectrum on the abraded patch *Quartier* ratioed to the raster median and showing similar spectral features as the mono-hydrated Mg-sulfates spectrum of kieserite showed in (a). (c) Mean spectra of rock targets in the Séítah formation as well as individual point spectra showing similar spectral features as the library spectra displayed in (a). Segments of the spectra shown with lower opacity line near $2 \mu\text{m}$ correspond to the main atmospheric CO_2 absorption domain, where residuals might affect the spectra. (d) Laboratory spectra of olivine (grain size: $0.1\text{--}1 \text{ mm}$) and magnesite ($<0.1 \text{ mm}$) compact mixtures (from Mandon et al., 2022) along with spectra from the RELAB library (magnesite KACB06A and siderite LACB08A). (e) Point spectrum on the abraded patch *Garde*, in which carbonates were detected by LIBS and Raman (Clavé et al., this issue/Clavé et al., 2022). Note the presence of a band near $2.5 \mu\text{m}$, possibly explained by a small contribution from carbonates. (f) Laboratory spectra from the RELAB library (olivine C1PO47 $\text{Fo}_{50\text{--}70}$, undefined grainsize; pyroxene C1SC35, augite, $45\text{--}90 \mu\text{m}$ particulate). (g) ICA components showing NIR spectral features similar to the spectra displayed in (d) and (f), with three components in input. (h, i, j) WATSON close-up on the abraded patches *Garde*, *Dourbes* and *Quartier*. (k, l, m) Contrast-enhanced RMI close-ups on the rock targets *Issole*, *Penne* (non-pitted) and *Rent* (pitted). Red circles indicate the location of the field of view of the IRS accounting for 68% of signal. See supplementary text S1 for image IDs.

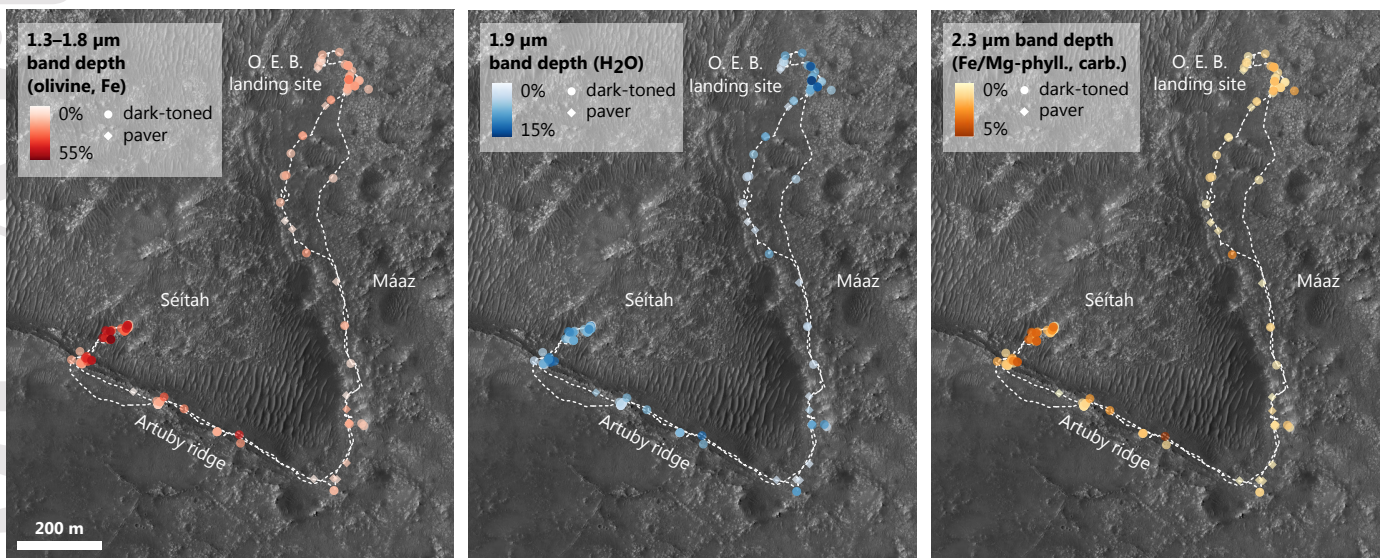


Figure 9: Spectral parameter maps along the rover traverse, up to sol 379 overlain on a HiRISE mosaic (McEwen et al., 2007; Ferguson et al., 2020). The Séítah formation is generally outcropping at higher elevation than the Máaz formation, but is stratigraphically on a lowest level (Farley et al., 2022; Wiens et al., 2022).

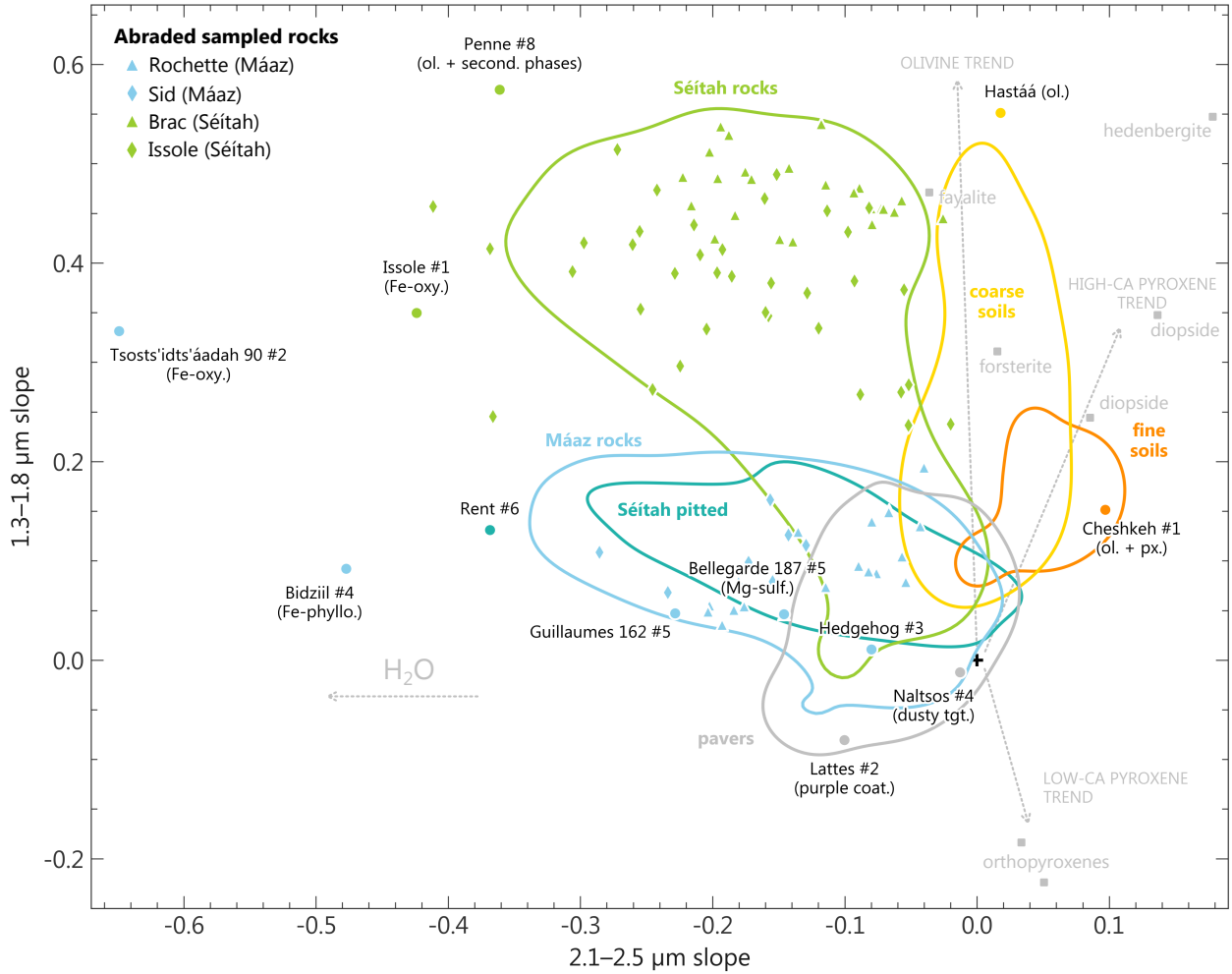


Figure 10: Diversity of the spectral shapes in the NIR for all the point spectra measured on the crater floor (solid lines), point spectra endmembers shown in previous figures (circle points) and sampled rocks (triangles and diamonds points). Solid lines delimit the kernel density estimate of the distributions for each type of observations, with an iso-proportion level set at 75%. Dotted lines indicate the trend of various mineral families inferred from laboratory spectra from the RELAB library (olivines and pyroxenes in grey squares). Pavers (dustiest rocks) include both targets from the Máaz and Séítah formations. The reader is referred to section 3.4.3 and to table 1 for the definition and sensitivity of the 1.3–1.8 and 2.1–2.5 μ m slopes parameters.

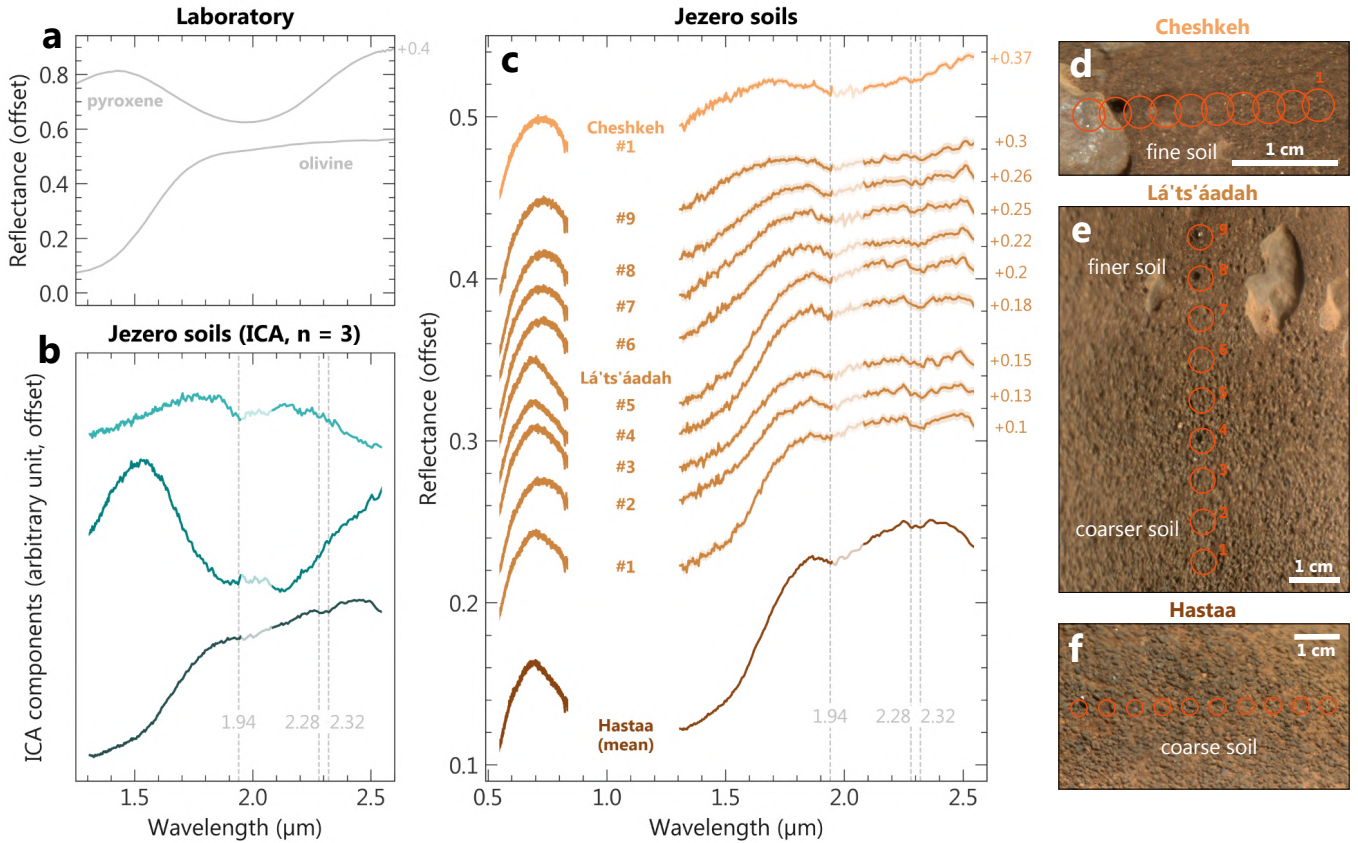


Figure 11: Spectral signature of the Mááz formation regolith. (a) Laboratory spectra from the RELAB spectral library (olivine C1PO47 Fo_{50-70} , undefined grainsize; pyroxene C1SC35, augite, 45–90 μm particulate). (b) Results of ICA considering three individual components. (c) Point spectra of selected regolith observations in the Mááz formation along with the corresponding RMI images in (d), (e) and (f). Segments of the spectra shown with lower opacity line near 2 μm correspond to the main atmospheric CO_2 absorption domain, where residuals might affect the spectra. Red circles indicate the location of the field of view of the IRS accounting for 68% of signal. The *Cheshkeh* target, observed on sol 116, is a fine soil with millimeter sized particles, while the *Hastaa* target, observed on sol 106 is coarse-grained, with millimeter-sized granules. *Lá'ts'áadah* was observed on sol 110 and exhibits a transition of granulometry within the raster, from millimeter-sized granules to micrometer-sized particles, correlated with an increase of the olivine absorption. See supplementary text S1 for image IDs.

Table 2: Summary of the minerals non-ambiguously identified with the VISIR spectrometer of SuperCam on the crater floor of Jezero and corresponding spectral features (values are absorption centers). Other suspected minerals are discussed in the text. Items labeled with a number in the Máaz and Séítah sections indicate minerals that have been detected in the corresponding unit from orbital NIR spectroscopy (1: Goudge et al., 2015, 2: Horgan et al., 2020, 3: Carter et al., 2022).

Máaz		Clinopyroxene ^{1, 2}	~2.3 μ m (broad and wide; ICA)
		Fe-oxyhydroxide(s) (e.g., ferrihydrite, akaganeite ³)	1.93–1.94 μ m (wide), occasional 2.46 μ m (point spectra and ICA)
		Fe ³⁺ -phyllosilicate (nontr. or hising. likely)	1.42, 1.92, 2.28–2.29 and 2.39 μ m (point spectra and ICA)
		Monohydrated Mg-sulfate	2.13 μ m and 2.4 μ m downturn (occasional; point spectra, ratios)
		Al or Si–OH-mineral (Al-phyllosilicate and/or hydrated silica)	2.20–2.22 μ m (point spectra)
		Mg–OH mineral (smectite, serpentine, talc and/or brucite) and/or carbonate – minor	2.32–2.33 μ m (point spectra)
Séítah	Pitted	Fe-oxyhydroxide(s) (e.g., ferrihydrite)	1.93–1.94 μ m (wide; point spectra)
		Fe ³⁺ -phyllosilicate (nontr. or hising.)	1.42, 1.92, 2.28–2.29 and 2.39 μ m (point spectra)
		Olivine ^{1,2}	0.7–1.8 μ m range (broad; point spectra and ICA)
	Non-pitted	Clinopyroxene	~2.3 μ m (broad and wide; ICA)
		Fe ³⁺ -mineral (nontr. or hising.) ²	2.28–2.29 μ m (point spectra and ICA)
		Mg–OH mineral (Mg-smectite, serpentine, talc and/or brucite) ²	2.32–2.33 μ m (point spectra and ICA)
		Fe/Mg-carbonates ^{1,2}	2.53 μ m (point spectra)
		Fe-oxyhydroxide(s) (e.g., ferrihydrite)	1.93–1.94 μ m (wide; point spectra)
		Monohydrated Mg-sulfate	1.9–2.3 μ m (ratios)
		Al or Si–OH-mineral (Al-phyllosilicate and/or hydrated silica) ²	2.20–2.22 μ m (point spectra)
Soils	Fine (μ m-sized)	Pyroxene	~2 μ m (broad and wide; point spectra and ICA)
		Olivine	0.7–1.8 μ m range (broad; point spectra and ICA)
		Hydration	1.94 μ m (point spectra and ICA)
	Coarse (μ m–mm-sized)	Olivine	0.7–1.8 μ m range (broad; point spectra and ICA)
		Fe ³⁺ -mineral (nontr. or hising. likely)	2.28–2.29 μ m (point spectra and ICA)
		Mg–OH mineral (Mg-smectite, serpentine, talc and/or brucite)	2.32–2.33 μ m (point spectra and ICA)
Dust		Fe-oxides	Strong 0.545 μ m band depth and 0.60–0.84 μ m slope (point spectra)
		Hydration	1.94 μ m (point spectra)
Purple coat.		Fe-oxides	Strong 0.545 μ m band depth and 0.60–0.84 μ m slope (point spectra)
		Hydration	1.94 μ m (point spectra)

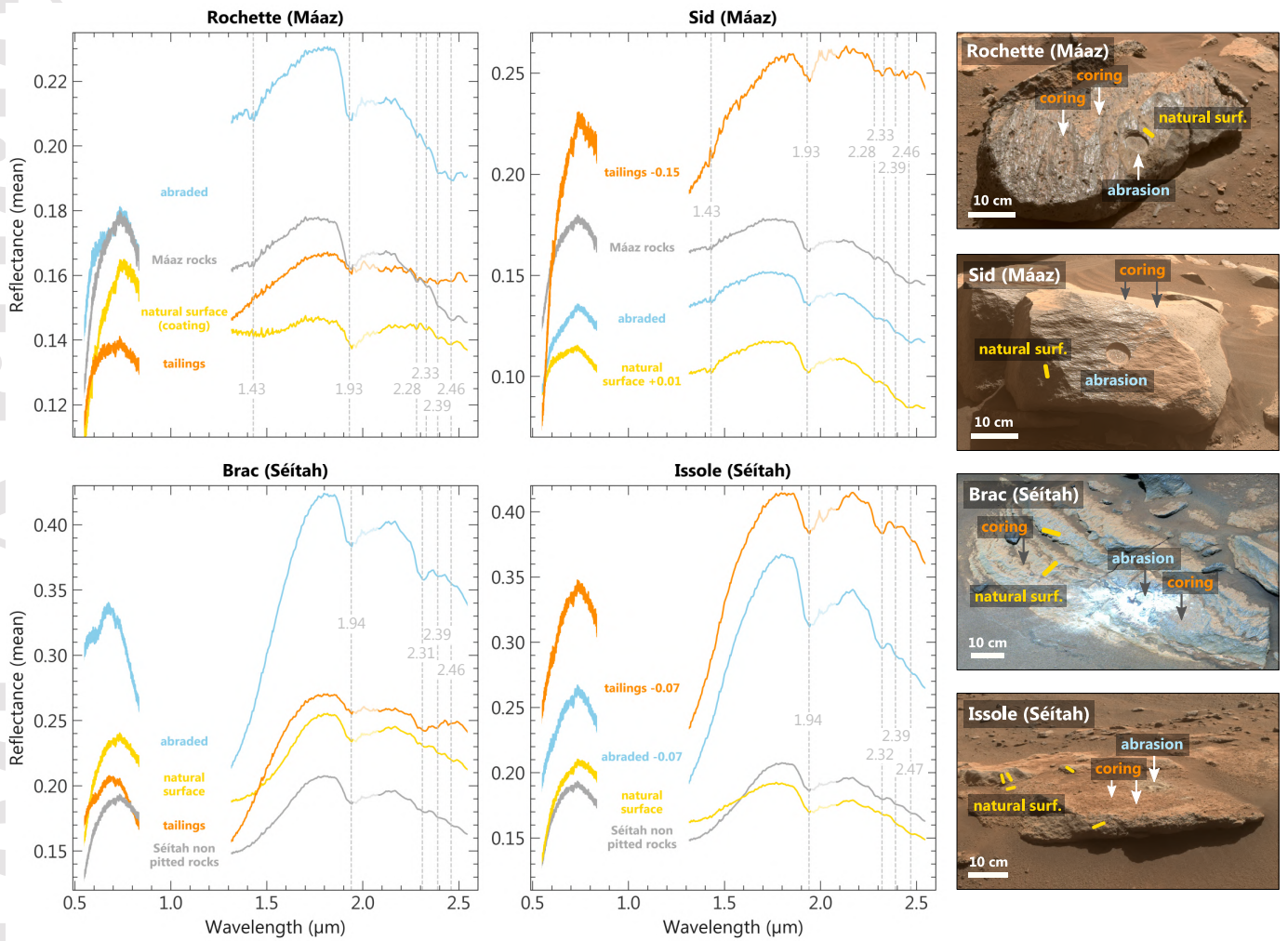


Figure 12: VISIR reflectance signature of the rocks sampled by Perseverance on the crater floor of Jezero along with Hazcams and Mastcam-Z context images. For each rock/outcrop (*Rochette*, *Sid*, *Brac*, *Issole*), two samples were collected, and SuperCam measurements were performed on the natural and abraded surfaces, as well as on the tailings resulting from coring or abrasion activities. See the supplementary text S2 for the list of targets considered in the averaged spectra. The positions of the main (possibly weak) absorptions identified to be recurring in the observations and meaningful for mineralogical interpretation are shown as vertical lines. Segments of the spectra shown with lower opacity line near $2 \mu\text{m}$ correspond to the main atmospheric CO_2 absorption domain, where residuals might affect the spectra. Note that these measurements were performed under variable phase angle, possibly affecting the absolute reflectance and spectral slopes. Yellow areas correspond to the locations of VISIR rasters performed on natural (i.e., non abraded) surfaces. See supplementary text S1 for image IDs.

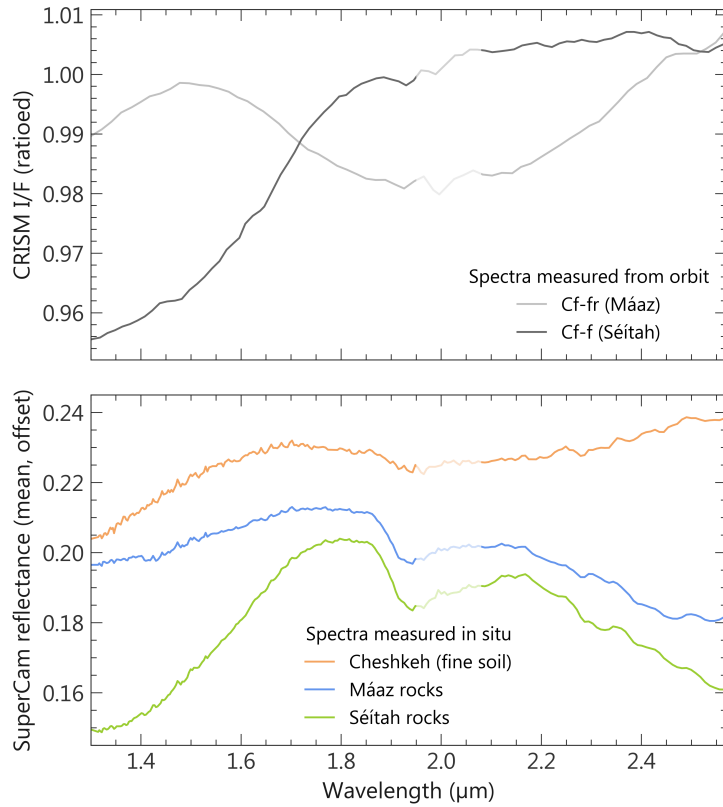


Figure 13: First-order comparison between in situ and orbital spectra of the crater floor. Orbital spectra were extracted from CRISM data by Goudge et al. (2015). Segments of the spectra shown with lower opacity line near 2 μm correspond to the main atmospheric CO_2 absorption domain, where residuals might affect the spectra.